Doctoral theses at NTNU, 2012:265

Amin S. Azar

Dry Hyperbaric Gas Metal Arc Welding of Subsea Pipelines

Experiments and Modeling

Doctoral Thesis

Amin S. Azar

ISBN 978-82-471-3840-3 (printed version)
ISBN 978-82-471-3841-0 (electronic version)
ISSN 1503-8181

NTNU – Trondheim
Norwegian University of Science and Technology

NTNU – Trondheim
Norwegian University of Science and Technology

NTNU
Norwegian University of Science and Technology
Thesis for the degree of Philosophiae Doctor
Faculty of Engineering Science and Technology
Department of Engineering Design and Materials

Doctoral theses at NTNU, 2012:265

NTNU

Amin S. Azar

Dry Hyperbaric Gas Metal Arc Welding of Subsea Pipelines

Experiments and Modeling

Thesis for the degree of Philosophiae Doctor

Trondheim, October 2012

Norwegian University of Science and Technology
Faculty of Engineering Science and Technology
Department of Engineering Design and Materials

NTNU – Trondheim
Norwegian University of
Science and Technology

NTNU
Norwegian University of Science and Technology

Thesis for the degree of Philosophiae Doctor

Faculty of Engineering Science and Technology
Department of Engineering Design and Materials

ISBN 978-82-471-3840-3 (printed version)
ISBN 978-82-471-3841-0 (electronic version)
ISSN 1503-8181

Doctoral theses at NTNU, 2012:265

Printed by Skipnes Kommunikasjon as

“

Here’s to the crazy ones. The rebels. The troublemakers. The ones who see things differently. While some may see them as the crazy ones, we see genius. Because the people who are crazy enough to think they can change the world, are the ones who do...

”

‘Think Different’ advertisement, Apple Inc. 1997.

Dedicated to Liberty...

List of Publications

Paper I
Statistical Analysis of the Arc Behavior in Dry Hyperbaric GMA Welding from 1 to 250 *bar*.
Journal of Materials Processing Technology 212 (2012) 211– 219.
Amin S. Azar, Neil Woodward, Hans Fostervoll, Odd M. Akselsen.

Paper II
Analytical Modeling of Weld Bead Shape in Dry Hyperbaric GMAW Using Ar-He Chamber Gas Mixtures.
Journal of Materials Engineering and Performance, Online First.
Amin S. Azar, Sigmund K. Ås, Odd M. Akselsen.

Paper III
Prediction of the Thermal Cycles in Dry Hyperbaric GMA Welding Using Partial Differential Heat Transfer Equations.
Trends in Welding Research, 4-8 June 2012, Chicago, USA.
Amin S. Azar, Hans Fostervoll, Odd M. Akselsen.

Paper IV
Determination of Welding Heat Source Parameters from Actual Bead Shape.
Computational Materials Science 54 (2012) 176–182.
Amin S. Azar, Sigmund K. Ås, Odd M. Akselsen.

Paper V
Effect of Hyperbaric Chamber Gas on Transformation Texture of the API-X70 Pipeline Weld Metal.
Metallurgical and Materials Transactions A 43 (9) (2012) 3162-3178.
Amin S. Azar, Erling Østby, and Odd M. Akselsen.

Paper VI
Effect of Hyperbaric Gas Composition on Mechanical Properties of the Weld Metal.
Materials Science and Engineering A, 556 (2012) 465-472.
Amin S. Azar, Hans I. Lange, Erling Østby, Odd M. Akselsen.

B

Contents

Preface

This PhD dissertation is apparently submitted to describe the authentically performed investigations during a period from September 2009 to September 2012 at Norwegian University of Science and Technology, Faculty of Engineering Science and Technology, Department of Engineering Design and Materials. The major financial support has been provided by the Norwegian Research Council and PETROMAKS program (Contract number 192967/S60). Statoil, Gassco, Technip, IFE and EFD Induction companies partly supported the project as project partners.

Trondheim, October 2012

Amin S. Azar

Acknowledgments

I would like to acknowledge the group of scientists whom I had the opportunity to have a share of their priceless knowledge during this work.

I wish to express my deepest gratitude to my supervisor, Professor (II) Odd Magne Akselsen, who granted me the opportunity, inspiration, courage and support. He provided me with the ultimate freedom that a researcher could possibly face for conducting a work along the track of interest and enthusiasm.

I owe a debt of gratitude to Professor Lars-Erik Svensson, who prepared the ground for achieving the greatest wish of my life.

Senior researcher, Dr. Erling Østby is gratefully acknowledged for patiently tolerating my endless quotes and queries.

Senior researcher, Dr. Neil Woodward deserves the best of my gratitude for dedicating his invaluable experiences where needed.

Dr. Sigmund K. Ås whom I learned the WeldSimS from is truly a devoted friend. Without his thorough insight, the genuine simulations of this work could hardly be fulfilled.

Mr. Hans Fostervoll who taught me the hyperbaric welding instruments- which is the axis of this study- is gratefully acknowledged.

This work has been scientifically supported by Dr. Hans I. Lange, Dr. Bård W. Tveiten, Mr. Bård Nyhus and Dr. Vigdis Olden whom working beside them was truly a great honor.

Sincere gratitude goes to those individuals at Statoil, Gassco, Technip, IFE and EFD Induction companies who were providing the grounds of this research.

I would like to wish the bests for the following group of people who were continuously backing me up in the technical practices:

Mr. Ansgar S. Hårsvær, Mr. Arne Gellein, Mr. Tore A. Kristensen, Mr. Andrew Marson, Mrs. Solveig Kirkenes, Mrs. Synnøve Åldstedt, Mrs. Lisbeth I. R. Støen, Mr. Wilhelm Dall, Mr. Yingda Yu, Mr. Levi Sandviken and Mrs. Aud Rodahl.

Exclusive thanks to all my friends and comrades in Norway and Sweden. Special thanks to Antonio Alvaro, Dr. Xiaobo Ren, Masoud Asgari and Peyman Mohseni who were almost following the same field of research. Mohsen Aminipour, Behbood Borghei, Mahdi Dehestani, Farham Farhangi, Farzad Irani and Sina K. Pakazad are all undoubtedly the best characters I have ever met, who supported me at all circumstances.

More importantly, I am deeply thankful for encourages from my family which have always been at the best of motivations for having such a thesis fulfilled.

Shirin, you know the best how much your supports benefited this work. I am dedicating this thesis on behalf of both of us, because, this work is truly yours…

Summary

Ambitions in exploration of oil and gas fields at deeper water depth require continuous investigation and maintenance. The transportation pipelines laid in deep waters are both subjected to corrosion and buckling due to environmental phenomena. They may also often undergo branching (namely hot tapping) to redirect (or add to) the transportation paths. Mechanical joints and welding are both considered as available alternatives when sectioning and replacement of the pipes at shallow waters is necessary, yet, welding is more promising for deep waters where remote operation is central.

Fusion welding on the other hand comprises several technological detractions for sound operations under high ambient pressures disregarding its low cost and flexibility. The foremost detracting phenomenon in the arc welding is called 'arc root constriction', which is defined as arc geometry shrinkage under the increased pressure. Consequently, the power delivery to the weld pool at different pressure levels is a major worry.

Effects of ionization and dissociation energies of different gases and mixtures, partial pressure of environmental gases including hydrogen and oxygen, gasification and degasification of the weld metal, inclusions that affect the phase transformation, absorption and desorption kinetics, oxidation and deoxidation reactions and many more are the phenomena that can possibly be altered by the gas type and ambient pressure level.

Spattering and fume generation is a problematic issue since the arc is rather unstable under high pressure. Thus, seeking the effect of different chamber gas mixtures on welding parameters, final microstructure and mechanical properties is the main objective of this work.

Statistical analysis of the collected voltage and current waveforms is carried out to identify the source of arc misbehavior and instability (discussed in Paper I). The stochastic parameters is related to the electrical stability and resolved into a number of varying welding parameters. The datasets are representing the effects of using pure argon under 14 incrementally increased pressure levels. Fast Fourier Transformation (FFT) is used to characterize the frequency domain of the waveforms. Auto-correlation Function (AF) and Power Spectral Density (PSD) were calculated assuming the Wiener-Khinchin theorem. Considering the AF, it is possible to visualize the deteriorating stability of the arc. The rate of stability degradation is quite gentle after 20 *bar*, though, huge differences were observed from 1 to 20 *bar*. The characteristic frequencies of 100-150 Hz and 350-400 Hz were observed. The first range can be associated with the mass transfer or molten

droplet launch frequency and the latter range is representative of the rectified mains. The spread of large low-frequency peaks at higher pressures is illustrating the mass transfer deterioration. The aforementioned peaks were found above 125 *bar* where the range of the characteristic frequency peaks in voltage and current waveforms started to deviate. The calculated arc power is higher at high-pressure range while the weld bead geometry was barely varied. It implies that the arc efficiency factor decreases at high pressures.

The heat source dimensions and heat efficiency factor are two major inputs for finite element (FE) simulations of the weld. However, a systematic classification of these factors was hardly available prior to this work. Additionally, to the best of author's knowledge, the direct high-speed observation of the arc inside the hyperbaric welding chamber has not been investigated in detail by far due to several technological issues. The varying bead-on-plate welds including the end crater appearance can possibly be good candidates to categorize the FE heat source dimensions. Double-ellipsoidal heat source (Goldak's Model) was implemented in WeldSimS® FE code that is used in this study. Since the model incorporates two superimposed reference heat sources, the amount of dissipated heat from each source should be differentiated. An intermediate heat source model was employed for this purpose. The latter model is after Myhr and Grong that is called distributed point heat sources. This model can be accurately fit to the weld cross section geometry if calibrated accurately. The calibrated parameters were found to be very close to the ones required by Double-ellipsoidal heat source model. By using this approach, not only the effect of welding parameters on weld bead geometry can be categorized, but also the spent time for double-ellipsoidal heat source adjustments will be cut by 90%.

A Gaussian heat source was also employed for welding thermal cycle simulations. Accompanying experiments suggested that the thermal gradients hardly change as pressure elevates. However, it was found that the increased pressure level might not necessarily result in higher or lower cooling rates despite the geometrical changes.

In a parallel investigation, the metallurgical effect of different shielding environments on phase transformation and mechanical properties of the bead-on-plate weld samples was studies. Electron backscattered diffraction (EBSD) and orientation imaging microscopy (OIM) techniques were used to identify the effect of five different shielding environments on the phase transformation. Argon and Helium chamber gases offer the conditions that facilitate the highest amount of acicular ferrite transformation, yet, they show some differences in a number of crystallographic details. CO_2 gas provided conditions for a lot of porosity in addition to the dominant polygonal ferrite/bainite transformation. He+½CO_2 mixture resulted in bainite transformation that was found to follow the maximum heat flow direction in terms of crystallographic orientations.

Very small sized tensile and single-edged notch bending (SENB) samples were machined from the weld metal material. The tests revealed that the best mechanical

properties are associated with the He chamber gas and the poorest properties were presented by the samples welded in He+½CO_2 shielding environment. It was also observed that there is a good correlation between the acquired acoustic signals and the fracture properties of the weld samples.

Chapter 1

Introduction and Objectives

Welding under high ambient pressure is often required in a variety of industries [1]. One example is subsea pipeline tie-ins and hot tapping in the oil and gas industry. However, this welding process should possess the best characteristics of a sound welded structure to be considered as a permanent repair. The wet welds are suffering from low toughness and ductility and the process productivity is very low [2]. Thus, welding under wet subsea condition fails due to a number of potential weaknesses when long lasting infrastructures with higher level of structural integrity is required.

The dry hyperbaric welding idea was developed to resolve the insufficient characteristics of wet welding. In the earliest type of dry welding, the workspace was surrounded by a chamber, which seals off the environment from the seawater*. In shallow water operations, the sealing structure can withstand the hydrostatic pressure outside and sinking such a chamber to shallow depth may not be a great challenge. However, for relatively larger depths, the chamber was sunk without being sealed that should be dewatered and sealed in depth afterwards. By increasing the depth of operation, it will be difficult to maintain the atmospheric environment inside the chamber. The water should be somehow pumped out of the chamber, and substituted by another media that is suitable for welding. If the gas shielded welding techniques are to be used, the chamber gas would consist of any conventionally utilized media like argon. However, the pressure inside the chamber should cope with that of the seawater: the deeper the operation, the higher the pressure will be.

The abovementioned high ambient pressure affects the process in a diversity of aspects. In general, ambient pressure pushes the welding parameters into the limits by influencing the overall arc stability, process characteristics and energy transport properties [3]. As a result, the pressure dependent parameters should be fine-tuned as long as their effects on overall stability jeopardize the viability of this method.

A number of welding methods can be used under the hyperbaric conditions† [3]. However, Gas Tungsten Arc Welding (GTAW) has been chosen due to the available knowledge in terms of its revealed characteristics. On the other hand, the

* Cofferdam welding

† Shielded Metal Arc Welding (SMAW), Flux-Cored Arc Welding (FCAW), Gas Tungsten Arc Welding (GTAW), Gas Metal Arc Welding (GMAW), Plasma Arc Welding (PAW)

initial pilot tests have shown that by simple manipulations in the GTAW method, relatively better stability can be obtained compared to the other processes. Moreover, the properties are more consistent with the offshore requirements [4]. Developments were first focused on GTAW followed by a number of investigations and reports mostly at Cranfield University, UK [3].

Since the divers' assistance at the larger depths is practically impossible, deep-water repair and hot tapping urges the development of remotely controlled equipment that can obviate the same performance as it was required in shallower depths. Conventionally, the GTAW can only be performed by intervention and the existing equipment may not offer the feasibility for fully remote operations. In this sense, the mechanized GMAW is considered a potential alternative, which can provide almost similar characteristics as can GTAW contribute.

The main objective of this thesis is to find alternative parameters that may ensure the quality and robustness of the hyperbaric welds. For this purpose, a thorough understanding of the arc physics is required for finding right solutions when modeling the welding related phenomena.

The general trend of welding arc behavior as a function of pressure and discussions about the possible reasons are eluded in a number of earlier studies. Moreover, the physical properties and the fundamentals of pressure effect on phase transformation and mechanical properties were barely investigated.

Lack of arc monitoring facilities for investigating the effect of environmental pressure on the metal transfer should be compensated by well-developed approaches to gain a better overview when defining the welding parameters for a wide range of pressure levels.

In this study, not only the source of arc instability is scrutinized, but also the effect of different shielding gases as a possible varying parameter on the final properties and microstructure of the weld metal is investigated and categorized.

New models are required to determine the effect of pressure on the heat source in finite element analyses (FEA) for 2D and 3D models as well as analytical approaches to take the effect of arc root constriction into account.

Fundamental understanding of the weld pool solidification as a result of weld pool (thermo)dynamics and reactions is a key for better design and qualification of the welding procedure.

Furthermore, the influence of shielding gas on transformation properties and texture of the weld metal should be analyzed in terms of microstructural constituents, chemical composition and grain boundary engineering (GBE).

Finally yet importantly, the mechanical properties of the weld metal under different shielding pressure should be analyzed to ease the following qualification procedures.

Chapter 2

The Technology of Dry Hyperbaric GMWA

1. General

During the past years, there have been many developments on types of chambers and repair procedures. The development of dry hyperbaric GTAW and GMAW has been reported chronologically elsewhere [2]. Here, the latest technology in developing the GMAW process will be addressed.

So far, replacing the damaged section of a pipeline has been performed using the sleeve concept [5]. Sleeve is an oversized segment of pipeline inside which the ends of two loose pipes are placed and fillet welded at both ends. Figs. 1**a** and 1**b** show the configuration of a sleeve-repaired pipeline.

This repair concept uses GMAW process in fillet welding and the operational procedure is as below:

The damaged site should be first discovered and dredged. Then the CRU (Coating Removal Unit) is launched for removing the concrete layer on the pipe using water jet. Then the CRU will be equipped with abrasive cutting jet and the damaged section will be cut and removed. A new pipeline including sleeves at both ends will then be deployed together with a SJU (Sleeve Jacking Unit) and H-frames. H-frames will have the responsibility of embracing and lifting the two ends of pipeline from the seabed and aligning the pipe ends for performing the welding operation. Fig. 2 depicts the H-frames.

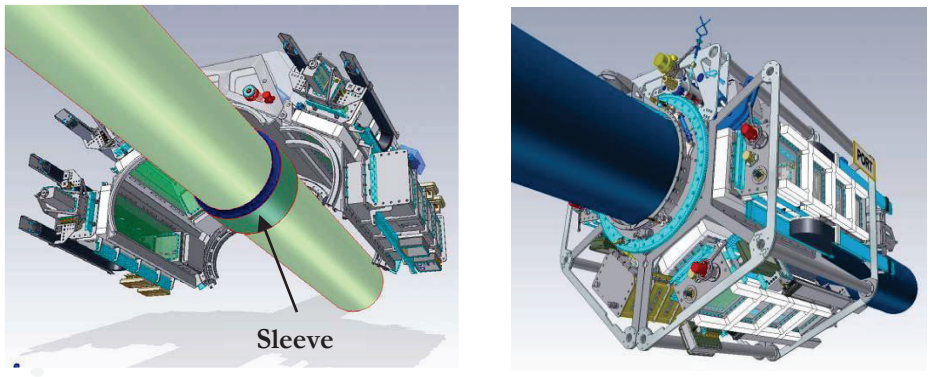

Fig. 1: Sleeve repair technology and installation. Threading the pipelines into a sleeve (**a**) and the operating chamber (**b**) [6].

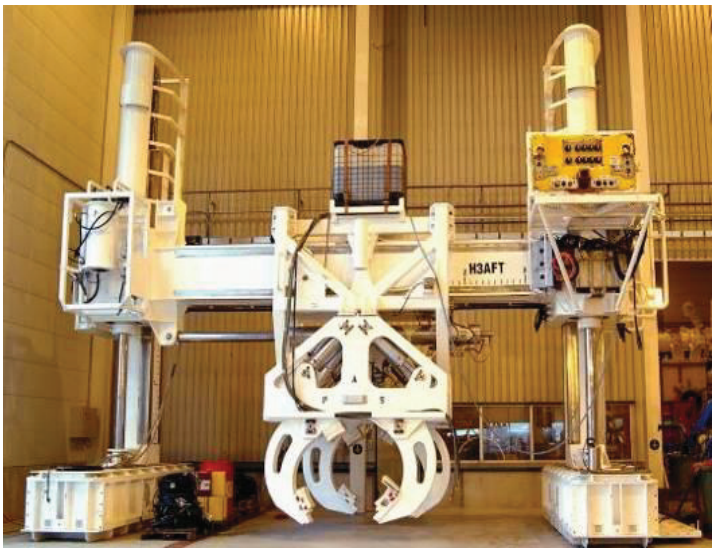

Fig. 2: H-frames for lifting the pipeline after removing the damaged section.

After the required alignments and sleeve positioning, the Remote Operated Welding Tool (ROWT) will be there to start the welding operation. As illustrated in Fig. 1**b**, ROWT includes a chamber that surrounds the operation site and seals it around. For evacuating the chamber from water, the chamber gas will be blown inside the chamber. In order to neutralize any hydrostatic pressure on the chamber, the inner pressure should comply with the water pressure at the operation depth. The latter sentence brings the challenges in welding about and such a challenge will be more intricate once the operation depth is large that requires high pressure chamber gas by definition [7].

After evacuation, the welding head is starting its duty. The deposition of weld bead starts and will be carried out until the fillet weld forms. Eventually, when the operation finishes, the entire equipment will be recovered and the pipeline will be sent back to its normal position. Apeland *et al.* [5] and Woodward *et al.* [7] have discussed the entire process more extensively.

In order to perform the qualification work, similar conditions should be simulated in the laboratory scale. There are currently two active chambers designed for GMAW dry hyperbaric welding purpose. One is lying in Cranfield University with the maximum pressure capacity of 250 *bar* and the other chamber located in SINTEF hyperbaric research laboratories with the maximum nominal capacity of 40 *bar*. These two chambers have been working during many years for analyzing process parameters and developing new procedures in subsea welding technology [5, 8].

For applying the same condition as in real process, the interesting water depth and materials are simulated inside the laboratory chambers. Depending on the

mechanical requirements of a certain type of welding, the process parameters will be optimized and qualifications will be developed. Figs. 3**a** and 3**b** are showing the aforementioned chambers at Cranfield and SINTEF.

The chamber at SINTEF consists of a conventional GMA welding torch without any shielding gas hose, a wire feeder with a spool at the back side of the chamber, optimized welding control unit and a gas mixture unit that can provide any mixture from Ar, He, CO_2 and O_2 as a chamber gas. The welding power source consists of three Fronius TransPocket TP 450 in series to deliver up to 450 A and 200 V. Another unit controls the power source parameters using a computer. The latter specifications apply to the power source used by the sister chamber at Cranfield [8].

Fig. 4 illustrates the upcoming chambers to be installed at PRS Pool, Killingøy. This chamber is under construction and will be operational shortly. Additionally, the volume of this chamber is about 2.3 m^3, with maximum capacity of 400 *bar* for providing the conditions of simulating the depth of 4 *km* of sea water.

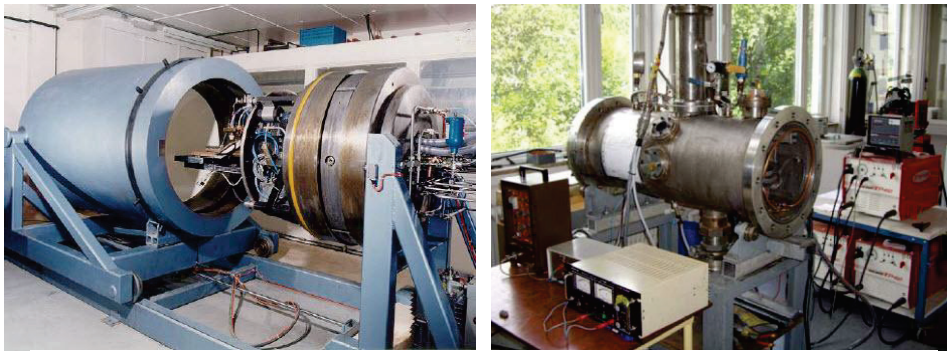

a **b**

Fig. 3: Hyperbaric chamber at Cranfield University (**a**) and SINTEF hyperbaric laboratories (**b**).

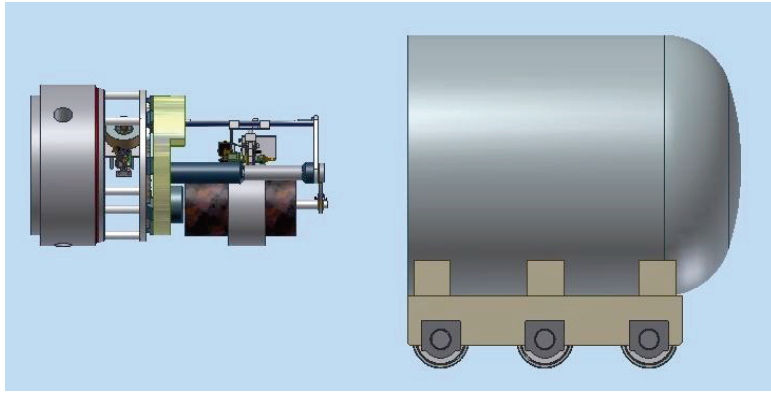

Fig. 4: New hyperbaric welding facilities at Statoil, Killingøy.

2. GTAW vs. GMAW

GTAW process has drawn special attentions by far. However, it is a confined operation in terms of human intervention limitations. Ambitious explorations of oil wells followed by laying transport pipelines in very deep-water depths require a process independence of divers' assistance. Moreover, controlling the welding head, electrode replacement and mechanical alignments are performed by divers' assistance. Since the working climate at 180 *msw*[*] is deemed to have incapacitating effect on the human body, the GTAW operation reaches to its limits [9]. On the other hand, although unmanned operation is considered cost effective, it requires skillful operators and near-perfect design.

Therefore, engineers have been looking for a replacement that offers almost the same characteristics of GTAW that is compatible with automation. So far, GMAW is the most adaptable method, which should be looked upon scientifically.

From the metallurgical point of view, GTAW is preferred due to its weld quality. The process is very flexible and can produce welds with higher toughness and finer grains [10]. However, GTAW provides the weld pool with rather lower rates of deposition that may result in decreased productivity.

Investigation of GTAW physics in the laboratory have also revealed that the arc characteristics undergo certain variations as the pressure increases [11]. Stability of the arc will be deteriorated and arc root will be contracted because of high pressure. Richardson *et al.* [12] have found that pressure corresponding to 500 *m* to 750 *m* impairs the entire process and makes the arc unworkable.

GMAW has also shown a strong pressure dependency. Increasing the pressure, results in a very unstable arc as well as lots of fume and spattering generation [13]. Nonetheless, the process can be under control by using tailor-made metal-cored welding wires. These types of consumables include some compounds and elements, which help stabilizing the arc under higher pressures. Moreover, power source parameters were adjustable to a number of conditions for GMAW in order to prevent frequent issues like lack of fusion [14].

Assuming the GMAW a suitable process, more studies should be carried out in order to define the effect of different parameters on the arc stability and weld characteristics. The following work will try to contribute in approaching to GMAW implementation, making the process parameters systematically clear.

[*] (Meters of Salt Water), corresponds to about 18 *bar*.

Chapter 3

Arc Physics in Dry Hyperbaric Welding

1. GMAW Arc Ignition

Gas Metal Arc Welding (GMAW) is a fusion welding process that requires an arc ignition between anode (+: welding wire) and cathode (−: workpiece)* [12]. In this type of welding, the anode electrode is of consumable type, which is fed continuously to the weld pool. Shielding gas flows with a certain rate for protecting the weld pool from being oxidized. It also prevents hazardous gas species in the air to find way into the weld pool [15]. However, in dry hyperbaric weld chamber, the surrounding gas is responsible for this task and therefore, there is no need for any extra flowing one [2]. In fact, the separation of chamber gas and shielding gas is feasible in the conditions that more expensive gas mixtures are required to protect the weld pool.

The shielding gas consists of an inert or active gas, which can be either pure or blended. This gas should be able to produce ionized or dissociated atoms in arc plasma temperature for cascading free electrons in the gaseous column. The gaseous jet is believed to be mainly made of such ionized atoms in addition to vaporized and molten metal during the process [16]. Due to economic reasons, shielding gases are not selected amongst the expensive ones, leading to a limited number of choices. Argon and helium are the most important inert gases employed in this type of welding. CO_2 and O_2 are active gases, which are normally added in portions to an inert gas, making it active. CO_2 is seldom used as pure shielding gas, and O_2, because of its oxidizing nature, cannot be used alone.

As mentioned in the previous paragraph, ionization of these gases in the potential difference between electrode and workpiece ignites the arc. When arc ignition takes place, in the very first moments, there is no molten metal and droplet transfer from electrode to workpiece. This range hardly exceeds several milliseconds depending on the power source settings. As a result, understanding the behavior of pure or blend gases during the ignition phase is crucially important.

* Reverse polarity can be applied in certain cases.

2. Shielding gas properties

As described in the previous section, the plasma jet consists of ionized gas, molten metal, slag and vapors. It has been proved that the formation of plasma arc is very much dependent on the overall properties of the shielding gas, which is used to protect the weld pool. Some of these properties have been tabulated in Table 1. The following descriptions about the basic properties of shielding gases have been fundamentally reviewed elsewhere [17-23].

Atomic/Molecular weight is a relative weight of a single atom compared to C-12. For sake of simplicity, the numbers are reported per *mol* of atoms. Thus, it has the physical dimension of $g.mol^{-1}$. It should be noted that the higher atomic weight implies higher number of electrons and protons in a single atom.

Ionization energy of an atom is the minimum required energy to remove an electron from the electron orbital cloud. As a result, an atom possesses *n* ionization energy, *n* equal to the number of electrons. Under equilibrium condition, the number of electrons and protons are the same and the bound energy is distributed amongst the electrons. However, when ionization takes place, the number of protons exceeds, the bound energy increases and it leads to higher required energy for the second electron to be repelled. The latter statement implies that the ionization energy decreases as atomic weight increases because of the farther position of outer electron shells with respect to the core, which leads to less binding energy. Theoretically, in a population of atoms, the second ionization will not take place unless the last atom of that population completes the first ionization process. Atoms with lower ionization potential will be easily ionized unlike those with lower atomic weight and higher ionization potential. In welding, gases with higher ionization potential may hinder the ignition phase.

The arc voltage will provide the required energy of ionization in the plasma jet. It infers that the required voltage for He is higher than that of Ar. Likewise, due to higher voltage, the heat input on the materials will be increased. Moreover, parameters influencing the arc voltage will also influence the ionization conditions of the shielding gas.

Triple point and critical point are specifying the thermodynamical conditions of a gas. These terms describe the boundaries at which the gas will undergo a phase transformation to liquid or solid. In hyperbaric welding, the knowledge of phase transformation of gases is essential since the gases are used in high-pressure ranges and low temperatures. These values are needed to specify the pressure and temperature ranges of using a gas in which it does not change its state to liquid or solid. For instance, the boiling temperature of CO_2 at 5.2 *bar* is about -57 *°C* while this temperature rises to about 10 *°C* at 50 *bar* [24].

Thermal conductivity of a gas is an indication of its heat conduction properties. The convection of gases around the plasma jet results in radial heat dissipation. Depending on the thermal conductivity value of a gas, the shape of weld bead varies. Gases with lower thermal conductivity will not dissipate the heat

to the surrounding easily, which leaves the arc core hotter than the peripheral area. In argon, it results in a specific geometry of weld bead known as 'argon finger'. The depth of penetration is larger in the middle where the hot arc core is located compared to the surrounding. Combination of different gases with designed proportions may lead to desired weld bead geometry.

Dissociation and recombination are the properties of molecular gases. O_2, CO_2 and H_2 better known as active gases are multi-atom gases. When these gases are heated to very high plasma temperature, the atomic bonds break and ions will be generated. The dissociated ions are in higher energy state and, once reaching the cold workpiece, they recombine and release heat. The recombination area is relatively large and the weld bead will be wider consequently. The dissociation and recombination energies of O_2 and CO_2 are tabulated in Table 1 and marked with asterisks.

Oxidation potential of active gases like CO_2 and O_2 not only change the arc physics but also result in constituent loss in the weld metal. Manganese and silicon are the most prone constituents, which show losses proportional to the percentage of active gasses in chamber gas. For defining how these gases affect the weld metal, the oxidation potential (*OP*) can be employed [15]:

$$OP = \%O_2 + C \cdot \sqrt{\%CO_2} \quad \textbf{(1)}$$

where *C* is a constant. In fact, this formula is optimized for atmospheric process while under hyperbaric condition, partial pressure of these gases is playing a paramount role. For instance, in a welding chamber pressurized with a mixture of (Ar, 5%CO_2, 2%O_2), *OP* will be higher at 10 *bar* compared to 1 *bar*.

Table 1: Characteristic parameters of different gases. (*) Dissociation and recombination energies of active gases [25].

Gas	Atomic/ Molecular weight	First Ionization Energy [$kJ.mol^{-1}$]	Second Ionization energy [$kJ.mol^{-1}$]	Triple point coordination		Critical point coordination		Thermal Conductivity [$W \cdot m^{-1} \cdot K^{-1}$]
				T [°C]	P [*bar*]	T [°C]	P [*bar*]	
Kr	83.79	1350.8	2353.5	-157.2	0.73	-63.6	59.60	9.4×10^{-3}
CO_2	44.01	1394.6*	2353.5*	-56.6	5.18	31.0	72.80	71.0×10^{-3}
Ar	39.95	1520.5	2665.8	-189.0	0.69	-122.1	13.49	17.7×10^{-3}
O_2	31.99	1317.2*	3399.4*	-218.8	0.01	-118.4	50.43	26.6×10^{-3}
Ne	20.18	2082.3	3961.2	-248.4	0.43	-228.6	27.60	49.1×10^{-3}
He	4.00	2372.3	5268.6	N/A	N/A	-268.2	2.27	151.3×10^{-3}

The addition of active gases into inert shielding gas may improve the arc stability [16], though, it is a trade-off between having a stable process and a sound weld metal composition.

Microstructural evolution can be discussed from thermodynamical point of view [26]. Since under the hyperbaric condition the solid phase free energy is assumed constant*, the discussion is mainly focused on the role of the present active elements in the shielding gas. As cited previously, O_2, CO_2, and H_2 are amongst those. The effect of CO_2 can be discussed in terms of the effects of C and O_2. The effect of H_2 is a comprehensive subject, which has been discussed by many researchers so far and will not be covered here.

It was found that the presence of oxide precipitates in weld metal entails formation of acicular ferrite in the solid-state phase transformation stage [27]. This microstructure was found beneficial in terms of weld metal toughness [28].

According to the classifications made by Babu [26], the microstructural evolution consists of two parts; thermodynamics and kinetics. From thermodynamical point of view, a change in microstructure occurs when the Gibbs free energy of that phase is higher than other stable phases (phases with lower free energy). However, the rate of such transformation is determined by the kinetics of a reaction or transformation. As a result, for understanding the presence of a special phase, its stability in terms of free energy should be sought. The stability of a phase can be a function of temperature, pressure and elemental concentration and activity coefficient [29].

In X70 parent metal case, Al, Ti, Si, V and Mn are the most prone elements to form oxide in the presence of oxygen. Apart from the epitaxial growth on the parent metal as a substrate, these oxides are considered as suitable sites of nucleation and growth at any stage of microstructural evolution. Their presence is apparently important when it comes to the desired phase constituents [30].

Depending on the morphology of an inclusion, its amount and its interface energy† with the product phase, different microstructure can be created [31]. Babu *et al.* [32] have described the overall transformation kinetics of inclusion formation during welding, using JMAK (Johnson-Mehl-Avrami-Kolmogorov) framework. This framework describes the overall transformation kinetics in one formula as below:

$$\zeta = 1 - exp\left[-\frac{1}{f} I_V \left(\frac{8\pi}{15}\right) (\alpha_3)^3 t^{5/2}\right] \quad \textbf{(2)}$$

* In fact, when welding, the chemical composition of the weld pool is subjected to change by the chemicals from welding wire as well as the reactions that are taking place prior to solidification [42]. Since the activity of an element is changing by its alloyed mole percent, deviation in free energy is definitely expected. This assumption makes the further studies simplified.

† Wetting Angle

where ζ is the transformation extent at a certain temperature, f is the fraction of precipitates under equilibrium condition, I_V is the volumetric nucleation rate, a_3 is parabolic function (appears in TTT/CCT diagrams) [33] and t is the retention time at a certain temperature. As it can be seen, higher I_V and smaller f brings about the larger transformation extent ζ.

Large phase region in CCT diagram means bigger area through which wide range of cooling rates can be accommodated. In other words, larger ζ value results in phase transformation consistency. If the relationship of oxygen partial pressure is constructed, the JMAK formula can be written as below:

$$\zeta = 1 - exp\left[-\frac{1}{F(P_{O_2/CO_2})}\eta\left(\frac{8\pi}{15}\right)(\alpha_3)^3 t^{5/2}\right] \quad \textbf{(3)}$$

where F is a relationship function between the partial pressure of oxygen/carbon dioxide and precipitates fraction and η is the resultant nucleation rate due to newborn embryos.

Back to hyperbaric condition, the partial pressure of oxygen will be increasing in higher pressure according to Dalton's law. It means that the F function will be changing accordingly. This is the moment where thermodynamics and kinetics will compete to find the right pressure of active gases. Unlimited amount of precipitates, thermodynamically need unlimited amount of driving force for nucleation that seems impossible theoretically. As a result, Eq. (3) is valid as long as the driving force for nucleation for every embryo is provided.

Jones *et al.* [34] have corrected the JMAK equation for precipitates that tend to form simultaneously. It will help more to predict the final microstructure when a number of precipitates with different morphology exist simultaneously. They have used their theory to calculate the nucleation potency in X70 steel [35]. They calculated that when the effective inclusion fraction doubles, the amount of idiomorphic ferrite increases about 7-8%.

The surface tension and surface-active elements have profound effect on weld bead appearance and geometry. Higher surface energy results in a humped, convex bead shape with increased susceptibility of undercutting. Consequently, flat weld bead is a product of low surface tension [36].

Surface-active elements like O_2 and CO_2 in the shielding gas and S in the weld metal and welding wire reduce the surface tension and lead to flatter bead profile. Subramaniam *et al.* [37] have described that this behavior has been observed when the effect of one surface-active element in the absence of the others is studied. They reported that S content decreases the surface tension but may increase or have no effect when 2%O_2 is added to the shielding gas. Pure argon is known to produce a humped bead cap but once combined with a sufficient amount of oxygen, the shape will be flattened. However, highly active gases like O_2 may be used with cautious due to their oxidizing effect.

The presence of surface-active elements, apart from variation in flow characteristics of the weld pool [38], enhances the slag formation by entering to a number of interactions. As a result, the existing approaches of steelmaking simulations can be fine-tuned for slag-liquid interaction to predict the inclusion formation during the welding process [39].

Under hyperbaric conditions, the pressure inside the chamber is above the atmospheric pressure depending on the depth of process. According to Young-Laplace equation [40], the pressure inside an ideally spherical liquid drop can be described as below:

$$\sum F = 0 \;\; \therefore \; -2\gamma(2\pi R) + P_i(\pi R^2) = 0 \overset{so}{\Rightarrow} P_i - P_0 = \frac{4\gamma}{R} \tag{4}$$

where P_i is the pressure inside in *Pa*, P_0 is the pressure outside in *Pa*, R is the radius of droplet in *m* (as illustrated in Fig. 5) and γ is the surface tension in $J.m^{-2}$. However, the droplet is not necessarily spherical and it may change its superficial shape differently at any instance. As a result, a general form of Eq. (4) can be defined to include the shape variations:

$$\Delta P = -\gamma \nabla \hat{n} = 2\gamma H \tag{5}$$

where $\hat{n}$ is the surface normal vector and H is the mean curvature in mm^{-1}.

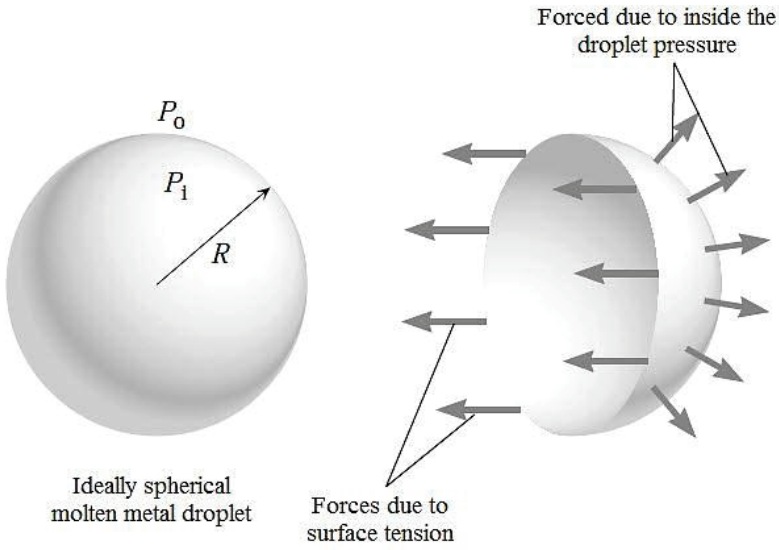

Fig. 5: The structure of ideal molten metal droplet between anode and cathode.

Referring to the Eqs. (4) and (5), it can be deduced that a larger droplet which is a product of larger surface tension, has lower internal pressure. Since the surface-active elements decrease the surface tension, spray of molten metal with droplets of high internal pressure should be expected. On the other hand, it is obvious when a droplet with higher internal pressure (small droplets) reach the weld pool, noticeable amount of spatter can be generated as a result of interface layer burst and high pressure molten metal launch. It can be summarized that the presence of surface active elements may increase the spattering due to the droplets internal pressure and may be used partially beside the chamber gases like He which tend to produce larger droplets with flat weld geometry.

Consequently, the gas atoms or ions configuration and density will be affected by the environmental pressure [41]. It is then expected to have eccentric behavior of gaseous jet compared to atmospheric condition. The following illustration is worth to be reviewed for better understanding of the involved mechanisms.

3. Gaseous Jet Formation

As pointed out previously, ionization of shielding gas is the cornerstone of arc ignition. Starting from the atmospheric condition, let us assume gaseous jet's shape is a conical frustum with its smaller base on the electrode and larger base on the workpiece. According to the observation and modeling, the nominal dimensions of such a frustum are illustrated in Fig. 6**a**.

This imaginary set-up is made based on a welding wire with 2 *mm* in diameter, a working distance of 10 *mm* and the weld pool of 8 *mm* in width. The volume of this imaginary cone is shown in Fig. 6**a**. Suppose that the surrounding chamber gas is 1 *atm* argon (no hyperbaric condition). Assuming the behavior of argon as ideal gas one can write [42]:

$$PV = nRT \tag{6}$$

or

$$P = \rho \frac{R}{M} T \tag{7}$$

where P is the ideal gas pressure in *Pa*, ρ is density in $g.m^{-3}$, R is gas constant in $J.K^{-1}.mol^{-1}$, n is *mol* number, M is the atomic weight (for Ar = 39.948 $g \cdot mol^{-1}$) and T is the temperature in *K*. The density of gases is dependent upon the ambient pressure and temperature. Thus, the density of the gases in the ignition phase of the process (low ambient temperature) can be calculated using the abovementioned formula:

Gaseous jet column density under atmospheric condition= 1.784×10^{-6} $g.mm^{-3}$
Gaseous jet column density at 1 *bar(g)* condition= 1.6×10^{-3} $g.mm^{-3}$
Gaseous jet column density at 10 *bar(g)* condition= 1.6×10^{-2} $g.mm^{-3}$
Gaseous jet column density at 250 *bar(g)* condition= 0.4 $g.mm^{-3}$

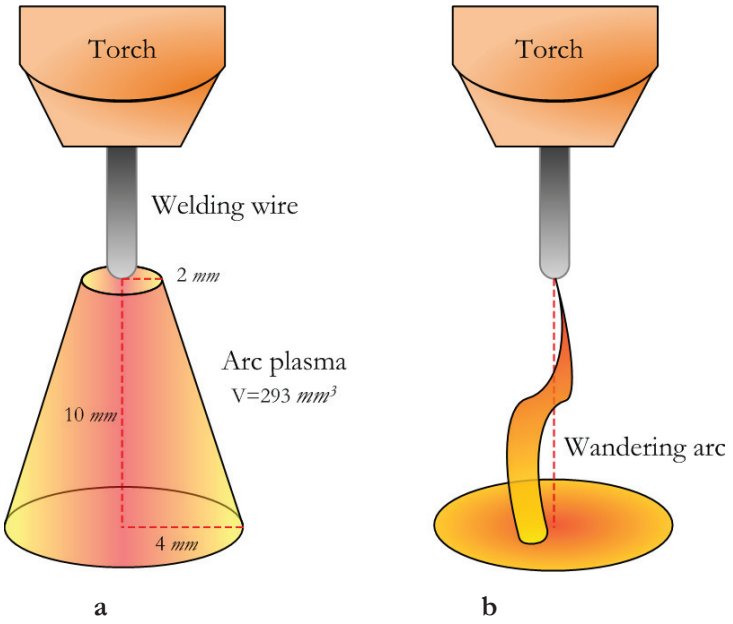

Fig. 6: GMAW gaseous arc plasma configuration (**a**) and wandering arc configuration (**b**).

The ambient temperature is assumed equal to room temperature despite down to 4°*C* is expected in the seabed operations (or lower in arctic operations). As it can be seen, increasing the gas pressure results in elevated concentration of argon in the imaginary gaseous jet volume.

For having a constant gaseous jet volume, it is necessary to ionize all the atoms in that volume. Assuming the 1st ionization energy of a gas like Ar is equal to 1520.6 $kJ \cdot mol^{-1}$ (Table 1) it can be written:

Required ionization energy under atmospheric condition: 0.02 *kJ*
Required ionization energy at 1 *bar(g)*: 17.85 *kJ*
Required ionization energy at 10 *bar(g)*: 178.9 *kJ*
Required ionization energy at 250 *bar(g)*: 4461.1 *kJ*

It is obvious that for keeping the arc shape constant, a huge amount of energy is required at higher pressures to ionize the atoms within the pressurized imaginary volume.

With respect to the previous studies of power source supplies, Fostervoll *et al.* [8] found that the suitable arc current is around 225 *A* giving 25 *V* of RMS (root-mean-square) voltage. This means that the arc energy is hardly exceeding 5.6 $kJ.s^{-1}$.*

* The energy losses due to convection and UV emission are not taken into account.

Moreover, higher voltage and amperage results in higher heat input in welding process, which may not be in favor of eventual weld microstructure.

Since arc strike will take place in the presence of potential difference, this amount of energy can only be sufficient for ionization of the aforementioned imaginary gaseous jet volume. Thereafter, such supplied energy can hardly ionize the same column of argon gas and therefore, the volume should shrink to ionize the corresponding number of atoms. This behavior is referred as 'arc root constriction' under hyperbaric welding condition. Richardson [3] has discussed these phenomena extensively.

At very high pressures, arc root constriction is noticeably high. This gives a column of gaseous jet, which is much smaller than the electrode cross section. Consequently, the arc will strike in any arbitrary spot of electrode cross section and moves across the area during a certain time range. This is another phenomenon which is regarded as 'arc wandering' at high pressures. The mentioned phenomenon is the source of process instability and has been emphasized by Richardson [43] and Matsunawa *et al.* [44]. Fig. 6**b** shows the arc wandering condition.

By combining the calculated elements into one analytical formula, the following calculations can be carried out:
The volume of plasma jet semi-cone can be calculated as below:

$$V = \frac{\pi h}{12}(W^2 + WD + D^2) \quad \textbf{(8)}$$

where V is the gaseous jet volume in *mm*, h is the anode to cathode distance in *mm*, W is the weld bead width in *mm* and D is the welding wire diameter in *mm*. The number of moles, which can occupy the semi-cone volume, can be calculated by combining the Eqs. (6) and (8):

$$n = \frac{\pi h P}{12RT}(W^2 + WD + D^2) \quad \textbf{(9)}$$

Assuming that every atom inside the arc column should be ionized, one can calculate the amount of energy needed for ionization. The required energy for ionizing one mole of a certain gas will be I_E. As a result, required energy for the entire gaseous column will be $n.I_E$ in *J*. On the other hand, the provided energy from the power source in a defined duration (t) will be $U.I.t$ where U is the arc voltage and I is the arc current. Since the arc power should provide the required ionization energy, these terms can be written in an equation as below:

$$n \cdot I_E = K_0 \cdot U \cdot I \cdot t \quad \textbf{(10)}$$

where K_0 is the energy correspondence coefficient.

According to [45] the arc energy can be resolved into a number of electrical parameters in short circuiting mode. The sum of those is considered as transient arc energy shown in the following:

$$E_A = \eta \cdot [\frac{LI^2}{2} + \frac{CU^2}{2}] \quad (11)$$

where η is the dimensionless arc efficiency, L is the inductance of electrodes in *Henry* ($J.A^{-2}$), C is the inter-electrode capacitance in *Farad* ($J.V^{-2}$) and I and U are current and voltage respectively in A and V.

By combining the Eqs. (9) to (11) it can be written:

$$K_0 = \frac{\pi \cdot h \cdot I_E \cdot P}{12 \cdot \eta \cdot [\frac{LI^2}{2} + \frac{CU^2}{2}] \cdot R \cdot T} \cdot (W^2 + W \cdot D + D^2) \quad (12)$$

where h is the anode to cathode distance, I_E is the first ionization energy per mol, P is the pressure, W is the weld bead width and D is the welding wire diameter. Energy correspondence coefficient, K_0, is a dimensionless factor that shows how many times of the supplied energy is needed to ionize the entire column, presuming that the volume does not change. As it can be seen, the K_0 coefficient has a power relationship with the weld-bead geometry parameter W and the wire diameter D. It implies that in higher pressure where K_0 is high, we may get higher W if we replace the welding wire with a thicker one. However, this replacement may not exceed certain limits, resulting in P-dependence of K_0. On the other hand, welding power source parameters are confined to certain values too. It seems that the only variable factor is the chamber gas. Replacing the conventional argon gas by other shielding gases* with different ionization energy may result in better stability at least in lower pressure range. Nevertheless, such gases are very expensive to be used as a chamber gas. The environmental temperature can affect the K_0 coefficient as well. Under subsea condition, it can be as low as 4°C. Heating the chamber gas can be an option in order to tackle with this problem.

4. Effects of shielding gas mixtures on weld bead geometry

It is known that the weld bead geometry varies by changing the shielding gas type [46]. The reason for this behavior is lies behind many factors [47]. Thermal conductivity of shielding gas is a determining factor ahead of some other factors that have been discussed earlier. Argon, for instance, offers a lower thermal conductivity level, which leaves the core of gaseous jet hotter than circumferential surroundings. This behavior leads to smaller gaseous jet cone compared to other gases. Thus, the weld bead will be wider close to the surface but deeper in the center†. It is difficult to identify the effect of different mixtures on weld bead geometry, but it is possible to anticipate using the given characteristics of each gas.

* e.g. xenon (Xe) or helium (He)
† Argon nose

In hyperbaric welding, ambient pressure will be influential in determining the thermal behavior of gases. Different mixtures behave uniquely in a defined range of pressure and temperature.
Pure argon at 25 $^{\circ}C$ and 1 *bar* initial condition shows thermal conductivity values, shown in Fig. 7.

As described earlier, argon possesses small thermal conductivity values. However, as a function of pressure and temperature, the values vary with ambient pressure and temperature. The physical nature of argon can be considered more pressure dependent when compared to He. It implies that in higher ambient pressure and temperature, the gas will show higher thermal conductivity and as a result, wider gaseous jet and shallower penetration should be expected. Nevertheless Woodward [48] have experimentally confirmed that the weld bead geometry does not vary beyond 100 *bar* up to 250 *bar*. Such phenomenon can possibly stem from the fact that the arc root constriction at high-pressure range concentrates the heat distribution in the central arc, counteracting the effect of increased thermal conductivity.

Helium possesses different behavior than argon. It is less pressure dependent compared to its overall dependency configuration. Moreover, its temperature dependency is much stronger than that of argon. Fig. 8 depicts the variation of thermal conductivity as a function of temperature and pressure. The variation of its thermal conductivity is about five times more than argon (Note the differences in thermal conductivity values). Since the thermal conductivity of He is not pressure dependent, it is expected to show deeper penetration in higher pressures since the arc root constriction competes with the conductivity values. The effect of ambient temperature was described in analytical analysis in section 3 of this chapter. Pure helium will be affected very much if ambient temperature increases. Wider weld bead due to very high thermal conductivity and instable arc behavior are also expected (e.g. difficult to ignite and/or short-circuiting).

High ionization energy of helium is considered as a drawback because it deteriorates the ignition characteristics when using pure helium. Addition of gases with lower ionization potential may obviate the problem to some extent. Thermodynamical calculation using gas mixture models can be employed to predict the behavior of a number of mixtures. However, a comprehensive model that can predict the high pressure and temperature ranges is not available so far. The calculation have been performed for a couple of mixtures and shown in Figs. 9 and 10. Detailed descriptions of the models and calculations are given in the accompanying paper II.

The 50%Ar, 50%He mixture shows thermal conductivity range almost as same as pure argon. It has just been increased very little because of the effect of helium. However, the calculated figures reveal that in 50% mixture, the argon behavior is prevailing. This mixture shows very small pressure dependency however, strong

temperature dependency can be observed. Larger gaseous jet is expected due to steep changes of thermal conductivity with temperature.

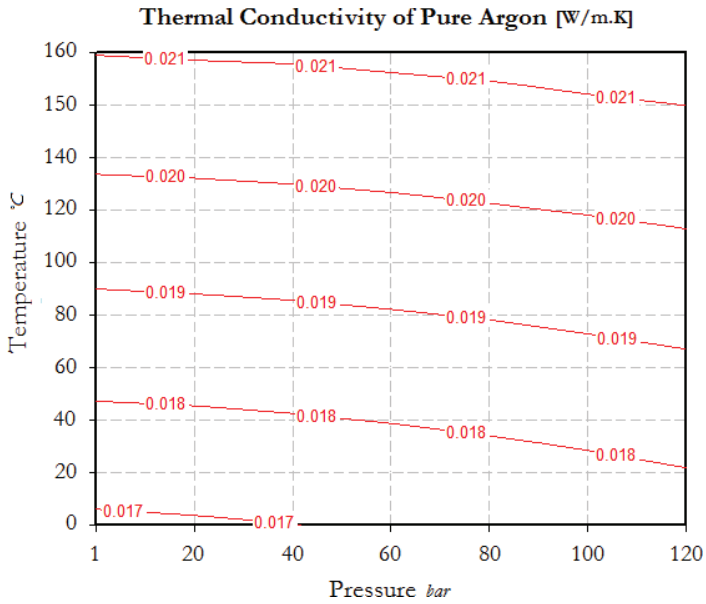

Fig. 7: Thermal conductivity of pure argon as a function of pressure and temperature.

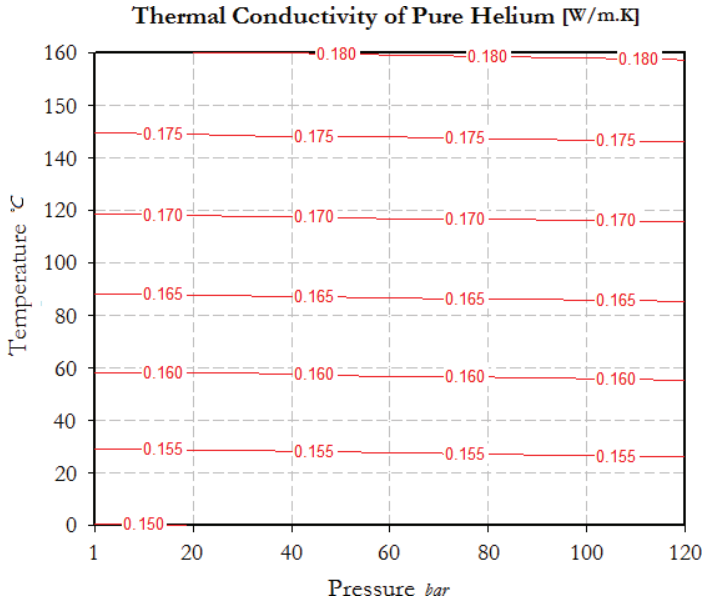

Fig. 8: Thermal conductivity of pure helium as a function of pressure and temperature.

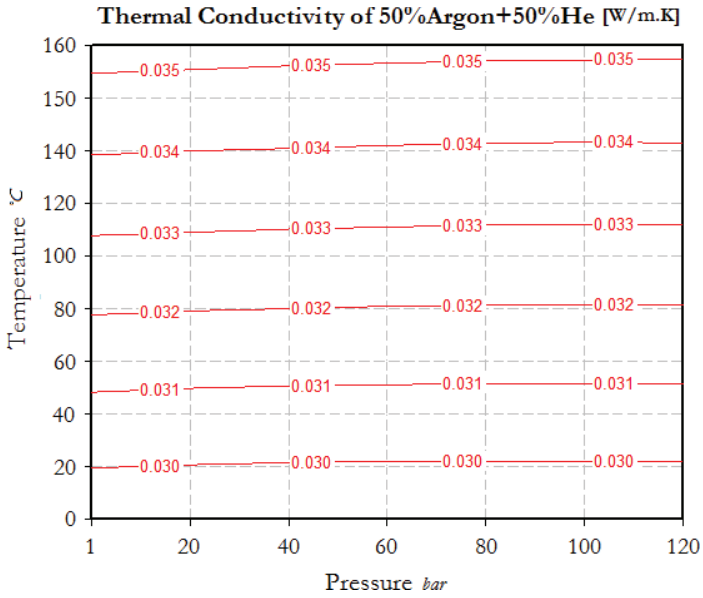

Fig. 9: Thermal conductivity of 50%Ar, 50%He as a function of pressure and temperature.

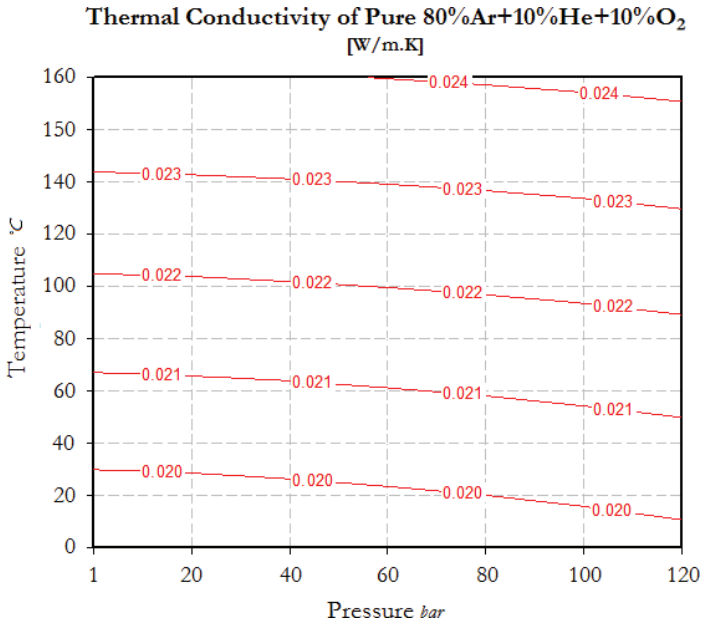

Fig. 10: Thermal conductivity of 80%Ar, 10%He, 10%O_2 as a function of pressure and temperature.

Second mixture is for investigating the effect of small additions to a pure gas. It can be seen that the thermal conductivity range and its behavior is matching that of argon. Oxygen reduces the surface tension of molten material and as a result works as a surfactant element. It is believed that the presence of oxygen improves the arc stability but it may decrease the weld pool viscosity, making such mixture unsuitable for positional welding. The presence of oxygen will also results in thicker slag formation, which can be a trouble in multi-pass deposition. Consequently, the Oxidation Potential (*OP*) should always be calculated and adjusted prior to welding.

Fig. 11 presents the behavior of CO_2 gas under varying pressure and temperature. It can be seen that the pure gas is affected by both parameters more than any previously discussed mixture. The thermal conductivity level can be compared with pure argon range; however, the pressure dependency is stronger. According to the triple point of pure CO_2 gas, it changes its state from gas to liquid at about 50 *bar* at room temperature, which means that the partial pressure of the CO_2 should never exceed this limit during the welding. It implies that CO_2 may not be a suitable candidate for shielding gas mixtures in deep water operations. Moreover, the slag formation and Mn and Si loss was detected when CO_2 was purely or partially included in the chamber gas. The results are presented in the accompanying paper IV.

Fig. 12 shows the end crater shape and size under a number of chamber gas mixtures conditions. It can be seen that the addition of He to Ar gently affects the heat source dimensions until the He percentage exceeds 90%.

On the other hand, the addition of CO_2 to He continuously increases the tail and decreases the width of the heat source. Fig. 13 illustrates the variation of the end crater dimensions with reference to the double-ellipsoid heat source parameters.

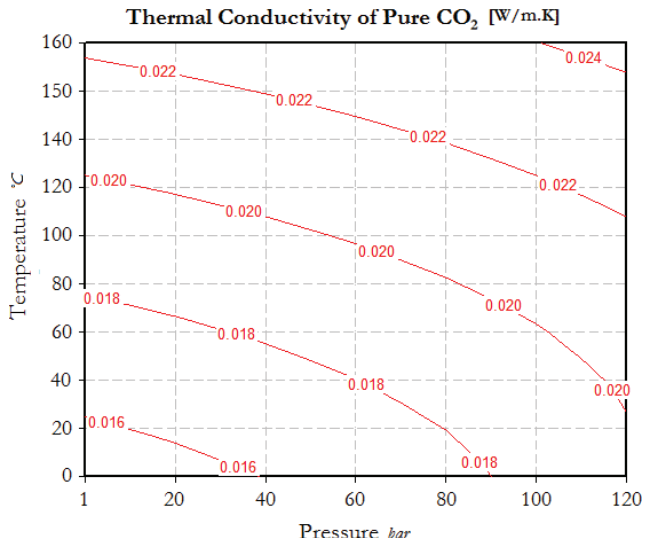

Fig. 11: Thermal conductivity of pure CO_2 as a function of pressure and temperature.

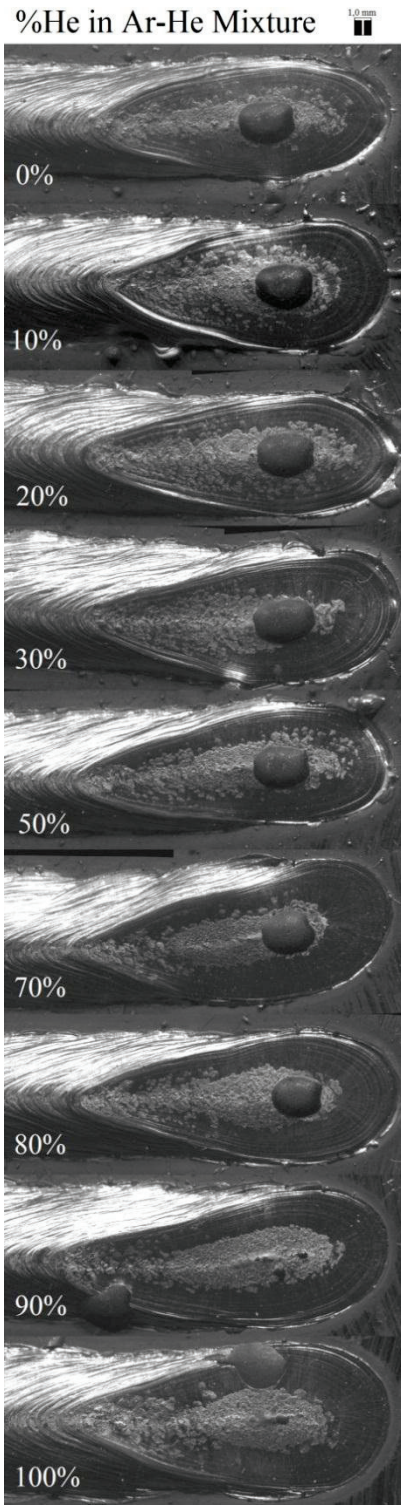

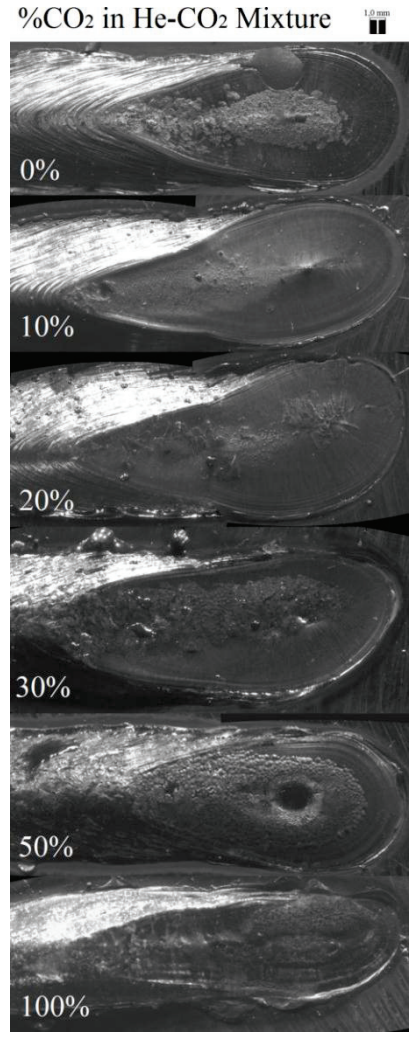

Fig. 12: End crater and bead shape of Ar-He and He-CO_2 mixtures. The tests were performed in identical conditions except the shielding environment. Pure He gas has created larger end crater and weld bead at 10 *bar* compared to the pure Ar. Higher CO_2 Percentage in He-CO_2 mixtures delivers higher energy as well as oxygen potential into the weld pool and results in metal boiling and oxidation in the weld pool.

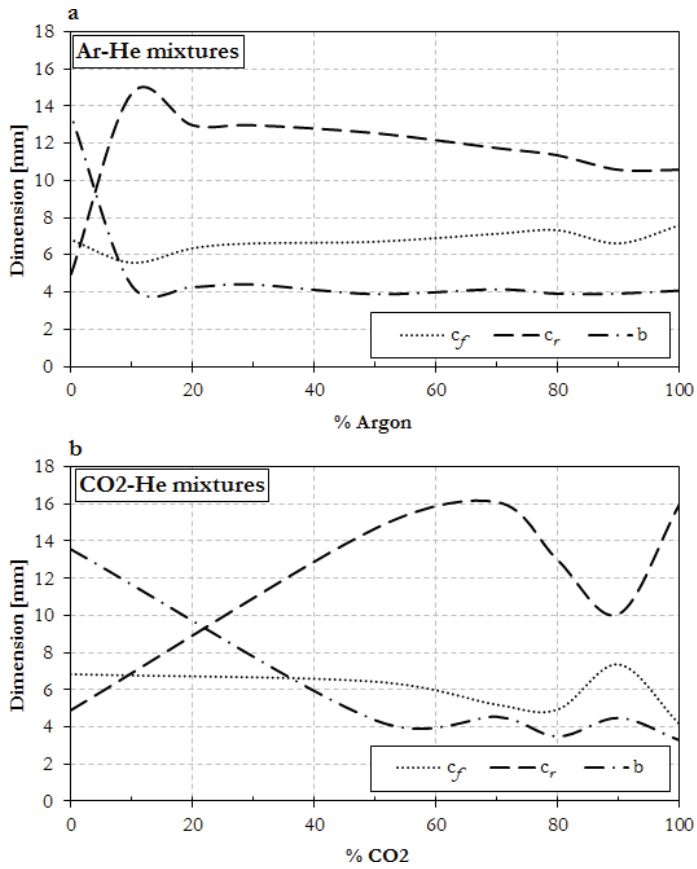

Fig. 13: Double ellipsoid heat source parameters variation in different chamber gas mixtures. (**a**) Ar-He mixtures and (**b**) CO_2-He mixtures.

Chapter 4

Stochastic Analysis of Electrical Data

As discussed earlier in chapter 3, ambient pressure has profound effects on the arc characteristics. In other words, in dry hyperbaric welding, the arc column size and its root constriction is a function of pressure. Hence, the pressure will affect the weld bead geometry as well as other weld characteristics as mentioned in section 3, chapter 3. Although it was believed that increasing the ambient pressure might imply an unstable welding process in terms of spattering and efficiency, traditional analyses barely utilized proper tools for identification of the weld characteristics. For instance, the mean voltage value has been observed to alter very little with respect to the pressure and the bead geometry was observed to remain constant after a certain pressure level [8]. However, Manual Metal Arc (MMA) data in hyperbaric condition showed that the frequency of voltage oscillation in a certain period increases by increasing the pressure in spite of unchanged mean value. Therefore, such variations demand new mathematical approaches to find the pressure dependency. Allum [49] has shown that there is an exponential relationship between the welding mean voltage and pressure as below:

$$V \propto P^n \quad \textbf{(13)}$$

Discussions were raised about defining the exponential value *n*. Deriving complicated expressions for constricted plasma arc case (including welding torch geometry working in limited parametric ranges) resulted in $P^{0.5}$ ($n=0.5$) relationship [50]. Since it was reported that the *n* value varies in the range of 0 to 1 in extreme conditions, it was not well described whether relationship of this kind may explain the instability of the process or not. Allum *et al.* [51] have published their results addressing the arc stability focusing on the shielding gas mass flow criterion and defined the typical pressure of 5 *bar*, which separates the laminar and turbulent gas flow regions.

The latter relationship refers to the condition that the pipeline weld repair habitat gas is tailor-made for divers with a noticeable amount of breathing air (He containing some O_2) while another shielding gas (70%Ar-30%He) was employed to protect the weld pool. Though, if the operation is performed remotely, there will be no need for habitat and shielding gas separation [52]. Accordingly, the initial assumption for the remote hyperbaric GMAW process operation is without shielding gas.

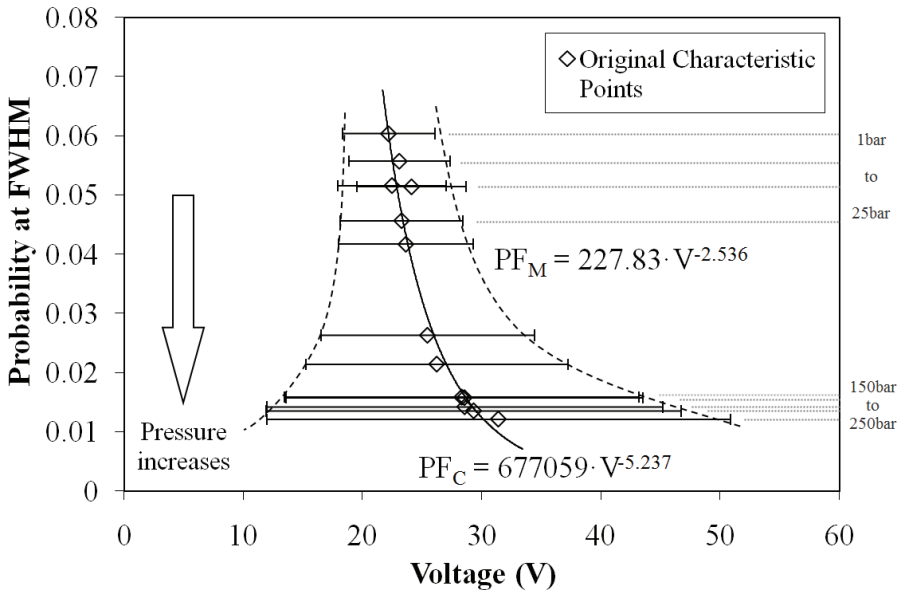

Fig. 14: FWHM and interpolation of voltage mean points.

Considering the welding current and voltage transient waveforms, the shape and sequences of certain occurrences as well as their amplitude may convey information about the effect of the welding parameters. Stochastic analyses can help to characterize waveform details, which bring the arc characteristic identification about. Thereafter, their significance can be determined by interpreting the effect of welding parameters.

Gaussian distribution can be used to analyze the voltage waveform. Fig. 14 shows how different pressure range affects the voltage root-mean-square as well as its distributional full-width-half-maximum (FWHM). The open symbols in Fig. 14 are the characteristic points for each pressure voltage waveform and a positioning function (PF_C) shows the locus of these points. The same regression has been performed for maximum band of FWHM (outer right locus) representing the variation of peak voltages (PF_M). The locus located on the outer left represents the variation of base voltage disobeying direct mathematical power relationship. It should be noticed that the extension of FWHM on the right and the left side of a characteristic point are equal but the variation of peak voltages is more outstanding since the characteristic points were shifted to the right as pressure increased.

The major achievement of this investigation is that the weld bead geometry can be related to the ambient pressure stochastically while classical approaches were not able to formulate such variations.

Chapter 5

Materials, Consumables and Experiments

Recently, high strength pipelines are demanding due to the higher requirements of sub-sea oil and gas transportation industry. A number of organizations have developed specification codes with regard to the materials, service conditions, manufacturing and repair circumstances. The most commercially well-known standard is from American Petroleum Institute (API), which names the pipeline material as two or three codes proceeded by 'X'. The digits show the specified minimum yield strength of the material in *ksi*. For instance, X42 according to API standards should have the minimum yield strength of 42 *ksi* corresponding to 289 *MPa* and minimum tensile strength of 413 *MPa*. As a result, higher grades of these material exhibit higher mechanical properties compared to lower ones. For full details see the API Specification for Line Pipe (API Specification 5L) [53].

Standard offshore requirements sets the minimum values of mechanical properties of welds described in AWS D3.6, BS 4515 and DNV-OS-F101. The welding parameters and conditions should be set in order to meet all these requirements.

The majority of sub-sea pipelines are manufactured using X42 to X65 grades. The selection of a specific grade depends on the requirements and design considerations as well as wall thickness and cost. Lower grades of API gain their strength from carbon-manganese constituents in normalized condition while the higher grades are strengthened by micro-alloying elements as well as controlled thermo-mechanical operation succeeded by a quenching and tempering [54]. In X70 and X80 materials, the carbon content has been lowered and more micro-alloying elements were added. Thus, the weld microstructure of these types is generally bainitic depending on the cooling rate. The chemical composition of X70 material has been reported in Table 2.

The tabulated chemical composition of X70 material is one of the Nordstream pipeline batches taken just before bending to form the pipe. This material was used throughout the entire experimental work of this study.

Table 2: Chemical composition of X70

	Chemical composition (%wt)										
	C	**Si**	**Mn**	**P**	**Ni**	**Cr**	**Mo**	**Cu**	**V**	**Ti**	**N_2**
X70	0.047	0.1	1.74	0.09	0.235	0.055	0.045	0.21	-	0.01	0.003
Max	0.08	0.28	1.85	0.015	0.31	0.1	0.06	0.3	0.01	0.02	0.008
Min	0.04	0.05	1.5	0.008	0.11	0.05	0.04	0.1	-	0.006	-

1. X70 pipeline material and weld properties

Since the latest developments are focused on the high strength materials, this study will review the properties of API-X70 steel. Optical microstructure sample of API-X70 is depicted in Fig. 15.

Performing a sound welding operation in micro-alloying steels with non-equilibrium microstructure can be challenging. The higher grades of API pipeline materials are more characteristic in terms of mechanical properties. Hence, it will lead to thinner wall thickness selection. Apart from the welding and transportation costs, thicker pipeline wall entails more passes of welding which in turn exhibits the problematic phase constituents as a result of embedded transformations. In other words, the thicker the pipeline wall becomes, the more unwanted phase constituents appear which may lead to in-service fracture. For instance, in the Inter-Critically Grain Coarsened Heat Affected Zone (ICGCHAZ) of a multi-pass weld metal, some brittle phases may appear named Martensite-Austenite (M-A) constituents which deteriorates the crack-tolerant characteristics.

Lambert *et al.* [55] have discussed the detrimental effect of M-A constituent on the cleavage fracture properties of multi-pass welded materials. Akselsen *et al.* [56] have observed the same constituents when welding with inappropriate filler metal in hyperbaric GTA welding. Thus, in order to reduce the sites that are prone to failure, stronger material is desirable. However, stronger materials contain more micro-alloying elements that may depress the weldability of the metal.

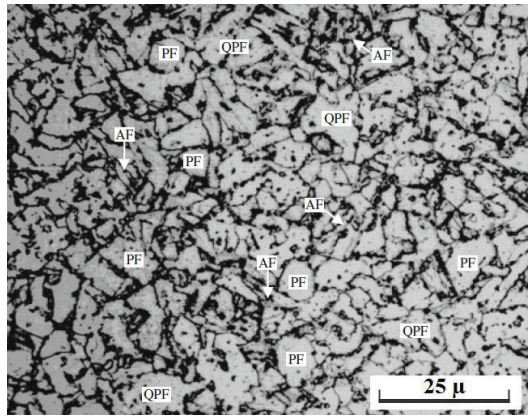

Fig. 15: Optical microstructure of API-X70: PF(Polygonal Ferrite), AF(Acicular Ferrite), QPF(Quasi-Polygonal Ferrite). Micrograph from [57].

In general, higher strength is achieved at the expense of reduced ductility and fracture toughness [58]. Amongst the test methods, Charpy impact test and Drop Weight Tear Test (DWTT) according to US standards, and SENT and CTOD according to EU standards are mostly used in quantifying the structural integrity of the pipelines [59].

Fracture mechanics sets a fracture into three stages; Initiation, Propagation and Final rupture. Crack initiation refers to the presence of mechanical damages or physical flaws. Mechanical damages can be of notch, scratch, dent *etc.* type. Physical flaws are those that are affecting the crystal structure of materials making it less strong compared to the requirements. Corrosion products, Hydrogen concentration and induced stress fields *etc.* can be of this kind. When these cracks reach to a critical size and stress level, they will start propagating through the material until the remaining cross section cannot withstand the mechanical loading condition at which final rupture takes place. There are many factors in pure material that can assist or resist this process. Nevertheless, welding microstructures can add more to these factors.

Tougher steels will postpone the crack initiation stage and leave the flaws detectable prior to final rupture [60]. Many researchers have been involved for many years to propose a model that can effectively predict the relationship of microstructure and flaw size known as 'flaw tolerance' [61]. So far, the general trend of relationship between the grain size and fracture toughness is well-understood (Multi-Barrier model) [62]. It infers that when welding, the different grain size across the HAZ may exhibit different behavior regarding to the crack propagation. Consequently, the amount of heat input and other critical welding parameters are of crucial importance in order to have a tougher and more crack resistant weld microstructure.

Hwang *et al.* [58] have studied the effect of in-range chemical composition on the fracture toughness of X70. They showed that the specimens with lower amount of C and Mo form acicular and polygonal ferrite and decreased fraction of M-A constituent compared to the others. These specimens were found to have higher upper-shelf energy in the Charpy impact test and lowest energy transition temperature among the others. It implies that the material with lower C and Mo content has improved mechanical behavior rather than the other specimens with higher in-range C and Mo content. They have also shown that the overall properties of the steels rolled in the single-phase region are better than those rolled in two-phase region.

Li *et al.* [57] investigated the effect of cooling time on the Coarse Grain Heat Affected Zone (CGHAZ). They showed that the microstructure of CGHAZ in X70 mainly consists of granular and lath bainite. They also observed the M-A constituents accumulated in lath boundaries. M-A constituents were seen to change their shape from elongated to massive as the cooling time was increased. It was found that M-A constituent is not the only governing mechanism in fracture but coarse bainite sheaves can assist initiating the cracks. They proposed $\Delta t_{8/5}$ of 8 sec.

as an optimum solution for X70 pipelines to obtain controlled microstructure as well as improved toughness. The predicted CCT diagram of X70 steel is shown in Fig. 16. Onsøien *et al.* [63] have constructed the CCT diagram of X70 steel by means of dilatometry and metallographic analyses. Their reported CCT diagram is very similar to the predicted one in terms of the transformations start and finish lines.

Spivakov *et al.* [64] presented that increased Mo content in X70 produces more amount of bainite for a certain cooling rate compared to those with lower Mo content. They also described the severe sensitivity of this dependency in the sense that a very small increase in Mo content expands the bainitic transformation drastically.

Richadson *et al.* [12] discussed the effect of weld metal overmatching on hyperbaric welding. Their effort focused on locating the plastic strains on the parent metal rather than weld metal. However, Thaulow *et al.* [65] and Minami *et al.* [66] argued that the weld metal strength overmatch can be detrimental with respect to the toughness of the HAZ in brittle fracture*. On the other hand, since the cracks have tendency to grow on slant planes with reference to the weld metal position, less weld metal is included in the process zone, which results in reduced effect of mismatching. Based on Multiple Barrier (MB) model by Lambert *et al.* [55], the cracks will be arrested once they are extending beyond the strength level of embedded material unless sufficient energy provides the required driving force for crack growth.

Consequently, the mismatching effect should be designed based on the service conditions. Thaulow *et al.* [67] concluded that evenmatching or undermatching is suitable for the components that will burden higher strains and stresses under lower service temperature condition. Overmatching was found beneficial otherwise. The choice of weld metal mismatch was advised with respect to the in-service conditions instead of its mechanical properties under standard testing conditions.

Nevasmaa *et al.* [68] showed that for a given steel, the heat input may not have substantial influence on the toughness of HAZ. Nevertheless, they reported the higher scatter in toughness results when welding with higher heat input. Dolby [69] discussed the presence of an exception that the HAZ exhibited lower toughness. The toughness of steels with high micro-alloying elements was found deteriorated when welded with higher heat input. This is in agreement with the aforementioned findings about the role of Mo content in bainitic microstructure by Spivakov *et al.* [64].

Moreover, Richardson *et al.* [12] performed some investigations on the effect of pressure on toughness. They found that the impact toughness of the weld does not follow any general trend for the welds produced at 160, 200 and 250 *bar*. As discussed earlier in chapter 3, increased pressure results in arc root constriction and

* Cleavage

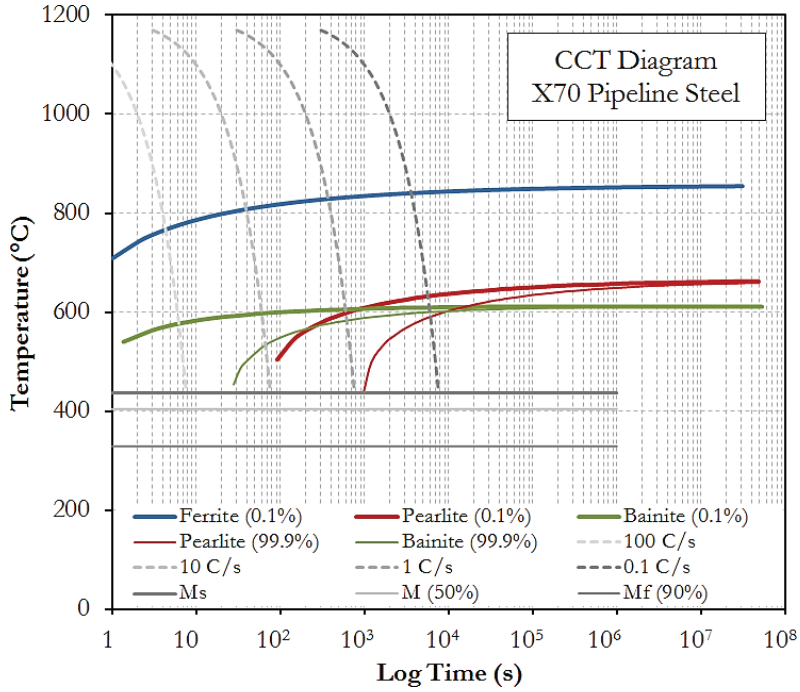

Fig. 16: Thermokinetic CCT diagram of API-X70 (Calculated by JMatPro Software).

heat concentration. Similarly, higher pressure has shown slightly higher process voltage, which infers higher heat input. According to the aforementioned sentences, the higher the pressure, the higher the heat input will be. It implies that heat input may not influence the general trend of weld toughness in dry hyperbaric welding. The latter sentence is in agreement with the reviewed researches.

2. Welding wire development

As described previously, arc stability is the major problem in hyperbaric welding. The welding wire in GMAW plays an important role in stabilizing the arc by employing a number of chemicals. Thus, the target in developing such a wire should be set in metal-cored type to include the effect of chemistry. Metal-cored wires consist of a metallic sheath with a hollow core filled with powdered materials. ESAB Company has been involved in this development for many years with diversity of products. These products were named HBX after "hyperbaric experimental". As it was discussed in section 2 in chapter 3, for obtaining a high strength and tough weld metal when welding in pure argon environment, higher level of oxygen is required for achieving acicular ferrite microstructure.

In 2003, ESAB came up with a series of tailor-made wires ranging from HBX6 to HBX13. They were different in nickel, titanium and oxygen level while the other elements were nominally identical. Many experiments were performed in order to find the optimum mixture of nickel, titanium and oxygen. They were all set to have 450 *ppm* as target level of oxygen in the weld metal.

Prior to this development, other providers released a number of products for this purpose. Thyssen K-Nova, ESAB XTi and ESAB Spoolarc 120 were amongst those. However, newer approaches set the requirements of producing more sustainable wires. The main problem with other wires was the root-bead toughness that showed very scattered and lower than minimum results in some occasions.

After a number of mechanical properties and corrosion tests including tensile test, hardness measurements, Charpy V-notch, borderline Crack Tip Opening Displacement (CTOD) and Sulfide Stress Corrosion Cracking (SSC), it was confirmed that newer revisions of wire offers improved characteristics. A subsequent revision from ESAB had lower manganese content to reduce the strength and hardness whilst maintaining ductility.

According to the producers, actual chemical analysis may not be carried out due to non-metallic inclusions. However, the chemical composition for these wires exists after calculated analysis. Table 3 shows the chemical composition of HBX12 and 13. It is worth noting that the HBX13 was the wire used in the experiments of this thesis. The chemical composition of the weld metal after deposition on X70 plate is tabulated in Table 4.

Table 3: Chemical composition of HBX wires

	Chemical composition (%wt)					
	C	**Si**	**Mn**	**Ni**	**Ti**	**O_2**
HBX12	0.06	0.5	1.84	0.5	0.02	600 *ppm*
HBX13	0.04	0.5	1.3	0.5	0.02	600 *ppm*

2

Table 4: Actual chemical composition of weld metal after welding

	Chemical composition (%wt)									
	C	**Si**	**Mn**	**P**	**Ni**	**Cr**	**Mo**	**V**	**O_2**	**N_2**
HBX12	0.073	0.42	1.86	0.012	0.53	0.03	0.011	0.011	485 *ppm*	42 *ppm*
HBX13	0.074	0.38	1.4	0.012	0.51	0.033	-	-	360 *ppm*	80 *ppm*

3. Welding Trials

Woodward [48] conducted comprehensive studies on the welding parameters at different pressure ranges for both single pass and multi-pass welds. Both pulsed and short circuit settings were reported in his work. The welding trials in this thesis were following the parameters optimized for the pulsed welding. The values are tabulated in Table 5. The welding was performed in controlled atmosphere, which means that the chamber was depressurized to 0.1 *bar* and flushed several times to reduce the environmental gases like oxygen and nitrogen inside the chamber. Except some test cases, the majority of the trials were in the form of bead-on-plate, 1G flat position.

Table 5: Welding parameters for 15 $V < V_{arc} < 90\ V$

I_p, Peak Setting	173 A
I_b, Base Setting	125 A
V_{TGT}, Target Arc Voltage	24 V
I_{TGT}, Target Welding Current	205 A
t_p, Peak Duration	4 ms
t_b, Base Duration	4 ms
Peak and Base Slopes	23 $V/100\ A$
Transition Dynamics	500 A/ms
Pulse to End Peak/Base	No
Welding Speed	7 mm/s
Wire Feeding Rate	135 mm/s

4. Weld Characterization and Testing

In this thesis, the microstructure of the weld metal is investigated for a number of samples welded under different shielding environment. Scanning Electron Microscopy (SEM) was employed rather than the optical microscope for the 2% Nital etched samples. Some of the microstructures are discussed in the accompanying paper VI.

The Electron Backscattered Differaction (EBSD) method was used to determine the effect of texture and crystal orientation with respect to the trasformation. The details of this study is given in the accompanying paper V. A new method for sample preparation was proposed. The target area to investigate was defined in the reinforcement of the weld samples close to the centerline of the weld bead. The samples were mounted in a conductive resin and automatically ground and polished to a very fine surface finish. To remove the deformation layer on the surface, 10 minutes of colloidal silica suspension polishing with pH of 9.8 and particle size of approximately 0.04 μm was used. The EBSD patterns were collected using Zeiss Supra 55 VP, low vacuum field emission gun scanning electron microscope. The EBSD detector could record at most 30 online patterns per second. The working distance was set to 20 mm with the tilt angle of 70° under a high-current electron beam. The accelerating voltage of the gun was adjusted to 20 kV.

In the mechanical properties tests, both tensile and single-edged notch bending (SENB) tests were performed. One tensile and three SENB specimens were machined from each weld bead for double clip gauge CTOD tests. All tensile specimens were positioned within the deposited weld bead while only the notch region of SENB specimens was extracted from the weld metal. The notch was positioned at the backside of the weld bead with a fatigue pre-crack extended into the weld metal around the weld centerline for all the samples. The diameter of the tensile specimen was about 2.5 mm and the length of the parallel section was

7.5 *mm*. A servo-hydraulic machine was used to perform both tensile and SENB tests. The strain rate was set to 0.113 $mm.min^{-1}$ in the tensile tests and 0.3 $mm.min^{-1}$ in the SENB tests. The tensile test was performed at room temperature while the ambient temperature of the SENB tests were set to -20°*C* to assess the possibilities for brittle behavior.

Electron-probe microanalysis (EPMA) was performed over the area on which the EBSD scans were taken. Quantitative measurements of nine elements (Al, N, S, Cr, Si, O, Ti, Mn and Fe) were registered for this analysis.

Chapter 6

Summary of Publications

Paper I

Statistical Analysis of the Arc Behavior in Dry Hyperbaric GMA Welding from 1 to 250 *bar*.

Journal of Materials Processing Technology 212 (2012) 211– 219.

Amin S. Azar, Neil Woodward, Hans Fostervoll, Odd M. Akselsen.

In this paper, mathematical approaches were developed for predicting the hyperbaric GMAW process arc behavior and stability. Bead-on-plate single pass welds were deposited under 14 pressure levels (1, 3, 5, 10, 15, 20, 35, 100, 125, 150, 175, 200, 225, 250 *bar*), representing low to high ambient pressure ranges. The electrical data including voltage and current waveforms were recorded for further analyses. Fourier transformation was used to resolve the dominant frequencies in the frequency domain of the waveforms. Prior to this analysis, the significance of the recorded data was identified for data adequacy purpose. The power spectral density (PSD) figures showed frequency ranges at about 125 and 375 *Hz*. The variation of stochastic parameters is related to the electrical stability that can be resolved into a number of varying parameters. The results show that most of the arc instability can be traced to the frequency domain of the voltage or current waveform. Uncorrelated current and voltage wave frequencies at higher pressures are found to have a great influence on process stability. The abrupt fluctuations of the arc current and voltage waveforms in the time domain is possibly the reason why low frequency peaks appear at high pressure range. Using the correlogram current data analysis revealed that the base currents are generated more randomly than the peak currents at all the pressures.

Paper II

Analytical Modeling of Weld Bead Shape in Dry Hyperbaric GMAW Using Ar-He Chamber Gas Mixtures.

Journal of Materials Engineering and Performance, Accepted.

Amin S. Azar, Sigmund K. Ås, Odd M. Akselsen.

In order to analyze the behavior of the arc under ambient pressure, a model is required to estimate the arc efficiency. A distributed point heat source model was developed to take the effect of ambient pressure into account. In this model, new parameters were introduced that defines the spatial point heat source resolution.

The simulated isotherms were calibrated iteratively to fit the actual bead cross section. By fine-tuning the distances between heat sources, the arc efficiency could be calculated. Basic gas mixture rules and models were used to calculate the thermal properties of the low-temperature shielding gas under the ambient pressure of 10 *bar*. Nine bead-on-plate welds were deposited each of which under different Ar-He chamber gas compositions. The average current and voltage recordings during the process showed that the average current decreases in the expense of increase in average voltage as He-to-Ar ratio increases. The thermal properties of the X70 base material were calculated using JMatPro® software. The well-known correlation between arc efficiency (delivered heat) and the thermal conductivity was established for different gas mixtures. The arc efficiency was considered separately for the transverse and perpendicular heat sources in order to approximate the weld bead shape accurately. It was found that assigning single heat efficiency factor for the entire arc, which is usually below unity, causes a noticeable underestimation for the heat transfer in the perpendicular direction and a little overestimation in the transverse direction.

Paper III

Prediction of the Thermal Cycles in Dry Hyperbaric GMA Welding Using Partial Differential Heat Transfer Equations.
Trends in Welding Research, 4-8 June 2012, Chicago, USA.
Amin S. Azar, Hans Fostervoll, Odd M. Akselsen.

In this study, the welding thermal cycles at three different pressure levels were investigated through experiments and simulations. Conventional thermocouple measurements were utilized along with a 2D heat flow model to identify the effect of weld pool shape on the thermal cycle of the weld. A new approach was assumed for considering the effect of third dimension. In this approach, the volume of the cuboid that embraces the actual heat source approximated by Goldak was identified upon which the two-dimensional heat source dimensions can be calculated. It was found that increasing the pressure results in minor changes of characteristic weld thermal cycle features. These variations were considered dependent upon the weld pool shape and size. Good agreement was observed between simulated and experimental results.

Paper IV

Determination of Welding Heat Source Parameters from Actual Bead Shape.
Computational Materials Science 54 (2012) 176–182.
Amin S. Azar, Sigmund K. Ås, Odd M. Akselsen.

In this study, the dimensions of a welding heat source model were considered based on experimentally observed weld pool sizes. An analytical approach called 'discretely distributed point heat source model' was used for this purpose as an intermediate stage between the experiments and the numerical model. In the

numerical approach, the heat source will be split into two perpendicular 2D ellipsoidal sources that correspond to the double-ellipsoidal heat source model. The third dimension of the heat source will be measured from the top-view of the end crater. The arc efficiency factor was calculated based on the findings in paper II. The contribution of each heat source was determined equal to the product of voltage and current multiplied by the heat flux fraction of the other heat source. In this condition, the heat flow from both sources was normalized and their contribution was equalized. WeldSimS and Matlab codes were used for finite element and analytical investigations respectively. In the Matlab code, the dimensions of the double ellipsoidal heat source model were calculated based ion the distributed point heat source model. Then the heat possible heat fluxes from both heat sources were mapped and the heat input value was normalized based on the flux generated by the overlapping heat source. Then, the values were used as input to the heat source parameters in 3D simulations using WeldSimS. Both models were compared and analyzed with respect to similar boundary conditions. Numerical simulations show good agreement with the analytical approach calibrated by actual weld dimensions. This approach obviated the need for time-consuming trial and error step in finding the right input for the heat source design.

Paper V

Effect of Hyperbaric Chamber Gas on Transformation Texture of the API-X70 Pipeline Weld Metal.

Metallurgical and Materials Transactions A, Published Online 05 April 2012.

Amin s. Azar, Erling Østby, and Odd M. Akselsen.

The development of the texture components in the X70 weld metal under several shielding environments was investigated using the electron-backscattered diffraction (EBSD) and orientation imaging microscopy (OIM) techniques. A new method for assigning the reference direction (RD), transverse direction (TD), and normal direction (ND) was introduced based on the morphological orientation of the grains. The main coordination axes were rotated with respect to the peak morphological distribution within the scanned area. The analyses showed that different shielding gases affect the weld metal texture and orientations. The shielding environment with pure argon shows the highest orientational pole density values and dominant acicular ferrite microstructure. The solid-state transformation of acicular ferrite was determined to follow the K-S orientational relationship on the (001) pole figure. However, the adjacent transformation patches, which were mainly within prior austenite grains, revealed no identical orientational relationship. This represents the fact that the grains near the centerline of the weld do not follow epitaxial nucleation and growth from the base metal. It also verifies that the acicular ferrite transformation takes place heterogeneously. Texture components allow determining the effect of shielding gas on the proportion of epitaxial or heterogeneous nucleation and growth. More textured transformation means that the employed shielding gas provides unsuitable thermodynamical conditions for heterogeneous nucleation. In this circumstance, the acicular ferrite formation may

be suppressed. It was also observed that the distribution of misorientation angle and special coincidence site lattice (CSL) grain boundaries play significant roles in determining the tensile characteristics of the weld samples. Moreover, the bainite lattice orientation was found dependent on the directional heat flow unlike the other detected constituents.

Paper VI

Effect of Hyperbaric Gas Composition on Mechanical Properties of the Weld Metal.

Materials Science and Engineering A, Online First.

Amin S. Azar, Hans I. Lange, Erling Østby, Odd M. Akselsen.

Selection of chamber gas composition for a viable and time-consuming underwater repair operation is influenced by the final mechanical properties that each shielding environment can offer. Tensile and fracture toughness tests were performed on five bead-on-plate test samples that were welded under different chamber gas environments (*i.e.* pure Ar, pure He, pure CO_2, 50%He+Ar, 50%He+CO_2) at 10 *bar*. The chemical composition, microstructure and mechanical properties of the weld metal were investigated. Electron Probe Micro-Analysis (EPMA) was used to identify the distribution of nine most important elements (Al, N, S, Cr, Si, O, Ti, Mn and Fe). Severe Mn and Si loss was detected when CO_2 chamber gas was used. Tensile and fracture toughness tests were performed on the bead-on-plate passes. Small size specimen were machined and prepared for tensile and single edged notch bending (SENB) tests. The fracture toughness test was carried out at -20°*C*. Crack resistance curves were constructed for all the samples with respect to the loading and unloading conditions. During the fracture toughness tests, acoustic emission (AE) sensors were used to identify the number and location of quasi-cleavage brittle fracture events. It was found that the pure He chamber gas offers the best visual and mechanical properties required by standards despite of its high costs. CO_2 chamber gas was discovered to introduce abundant micro and nano pores in the matrix that can potentially degrade the mechanical properties. He-CO_2 mixture however, was assessed to be detrimental due to both a dominating bainite transformation and distributed pores in the weld metal. The properties of the weld metal using Ar and Ar-He mixtures were found slightly poorer than the properties in pure He case, yet better than the rest of the samples. The number of fracture events recorded by AE sensors was consistently in agreement with the fracture resistance curves; the poorer the fracture resistance, the higher the recorded acoustic emission will be.

Chapter 7

Discussion

The present piece of research was structured in three categories to disclose a number of unknowns in dry hyperbaric welding. The first step is developing a new approach for arc monitoring using the electrical data during a hyperbaric welding process. The second step is introducing 2D-FEA, 3D-FEA and analytical models that incorporate the effect of pressure on the arc characteristics. The third step is investigating the phase evolutions and mechanical properties of the weld metal when welding parameters are varying.

Electrical Data Analysis

The findings in the first step accommodate the idea of monitoring the metal transfer by applying the Fourier transformation on the weld electrical data to visualize the traces of instability in the waveforms. This approach helped to identify the source of instability at high-pressure ranges. It was shown that the required power for maintaining the arc follows an increasing regime as ambient pressure increases. Moreover, near constant weld bead shape proposes that the arc efficiency factor is relatively low at high-pressure range because of excessive energy loss. For a typical density spectrum of the current, it was observed that the energy is more concentrated at around 100–150 Hz representing the pulsing frequency of 125 Hz. This interval represents the frequency of formation and detachment of the droplet. Comparison of the electrical data at different pressures reveals the fact that governing droplet transfer regime does not change as the pressure increases. However, if the ambient pressure increases, more energy is concentrated in the frequency region below 100 Hz, which could be explained as the existence of less frequent droplet transfer events. In other words, abrupt fluctuations of the current and voltage influence the frequency domain and relocate the peaks towards lower frequency ranges.

Analytical Model, 2D and 3D-FEA

From the prediction point of view, the knowledge of arc efficiency factor and arc constriction factor is of great interest in order to model the welding procedure with precision. The second step emerged as a respond to such interests. In this step, an analytical model was primarily developed to embed the pressure effect. This model, which was initially proposed by Myhr and Grong, provides the grounds for calibration using actual bead shape. It means that the deposited weld beads on plate under different pressure conditions were used to calibrate the novel parameters of the model. These parameters include the spatial resolution of the point heat sources

that cannot be defined in its original form. Once the model was trained, the arc efficiency factors can be calculated for variety of pressures and shielding environments. Stepwise increments of the He-to-Ar ratio were used at 10 *bar* in this study. The arc power increases systematically as He level increases. Nevertheless, the depth-to-width ratio decreases steadily to about 70%He-Ar and increases dramatically as it approaches to pure He. Such contradiction suggests the presence of other factors (e.g. gas thermal properties) in determination of the weld bead shape. The calculations of thermal conductivity values suggest that the variation of either pressure or temperature has the same magnitude of effect in pure Ar while pure He is affected more by temperature rather than pressure. It is worth noting that a comprehensive model that can predict the thermal conductivity of Ar-He mixtures at high pressure and temperature ranges is not available by far.

In 2D-FEA approach, the welding thermal cycles with respect to the pressure changes were studied both experimentally and numerically. It was found that placing the thermocouples in the same level close to the fusion line in the simulation phase shows a minor increase in austenite retention time. One of the fundamental differences in the simulated and experimental thermal cycle results is in their heating rate. Experimental curves are showing steeper rate compared to the simulated counterparts. This can be the major reason for time scale drift of simulated peak temperatures and cooling cycles. No obvious trend was recognized for a few points as pressure increases. Nevertheless, the cooling rate varies as pressure changes which results from the effect of pressure on arc efficiency factor. Moreover, investigation of the weld metal shows that minor variations of $\Delta t_{8/5}$ has imperceptible effect on the microstructure because the cooling curves are possibly passing the same transformation region of the respective CCT diagram.

In 3D-FEA simulations, the well-known double-ellipsoid heat source model after Goldak was used. However, for fine-tuning the weld bead shape, at least two superimposed heat sources were required each of which with different parametric values that can only be calculated using an analytical model or trial and error. The aforementioned analytical model, which was already calibrated by a real weld bead, was considered to calculate the required 3D heat source dimensions. The best fit was found when equal amount of heat dissipates from both sources. In order to equalize the heat input values of both heat sources, the product of voltage and current of each was multiplied by the heat flux fraction of the other one. Consequently, the heat fraction of each heat source should be calculated prior to the modeling phase.

Electron BackScattered Diffraction (EBSD)

The effect of different conventional shielding gases and mixtures on the transformation texture and mechanical properties of the weld metal was scrutinized in the third step. These gases include pure Ar, pure He, pure CO_2, 50%Ar+He and 50%He+CO_2. A novel approach in determining the area of investigation and sample extraction was also needed in the third step to represent the characteristics of entire weld metal. Electron backscattered diffraction (EBSD) method was used

to identify the effect of crystal orientations, symmetry, grain boundaries and grain sizes on the mechanical properties of the weld metal using a number of shielding gases. It was shown that high grain boundary length, especially the high-angle boundaries impede the dislocation movement from grain to grain and results in higher yield strength. The most textured weld metal sample appears when the pure Ar chamber gas was used. The analysis of all samples for their average elastic stiffness in terms of the crystal orientations and applied stress direction showed that the development of textured bainite constituents promotes the elasticity. However, grain boundary characteristics, confines the plastic deformation when 50%He+CO_2 mixture was used that results in limited plasticity. The η-fiber texture shows the variation in the orientation function for all planes and <001> parallel to the reference direction. Therefore, it is obvious that the growth of bainite constituents consistently follows the characteristic heat flow in welding.

Mechanical Properties

Investigating the effects of microstructure and chemical composition due to different shielding environments was a part of third step. Findings from this step can be traced to the second step for phase transformation simulations and better future predictions. The discovery of columnar bainite (CB) in the high-pressure, high carbon sample was a guideline in analyzing the effect of poor mechanical properties when high percentage of CO_2 gas was used. High carbon content in the weld metal coming from either the environment or consumables may have the same results when welding under high-pressure conditions. The presence of CO_2 in the chamber gas increases the oxygen potential particularly at higher ambient pressures. It was shown that the quantitative level of Mn in the matrix decreases when CO_2 chamber gas is utilized. Lack of Mn causes a shift in the CCT diagram towards enhancing the formation of more high-temperature transformation phases. Conversely, the limited growth of prior austenite grains impeded by oxide particles, may not lead to acicular ferrite transformation. Pure CO_2 or addition of CO_2 to He were found deleterious due to insufficient acicular ferrite transformation across the weld metal.

Overall

The general requirements of a sound spatter- and fume-free, high quality welds that possess the best possible mechanical properties are obtained when pure He gas was employed. The effect of very high pressure on pure He gas is not yet studied, though, medium pressure range qualification revealed promising properties. The main reason of high scale mechanical properties of the weld metal when using He gas can be traced to the first and second steps. The microstructural evolution during solidification and phase transformation are also expressing the reason for better mechanical properties. High distribution of special grain boundaries and favorable phase constituents were offering the best arrangement using pure He as an alternative. The necessity of studying the bead-on-plate welds is its resemblance to the root pass weld inside the joint preparation. Currently, the concept of butt-

welding of the replaced section in a damaged pipeline is being studied, which requires the detailed knowledge of root pass properties.

Chapter 8

Conclusions

In the earlier chapters, the challenges and studies of the preceding researchers about the effect of ambient pressure on the weld bead shape and characteristics were reviewed in detail. To the best of author's knowledge, the quantitative trend of the pressure increments on the weld bead morphology was never investigated systematically. The core of this work was to understand how different shielding gases influence the final properties of the weld.

Electrical Data Analysis

In the early stages of the project outline, a method was desired to compensate the lack of arc monitoring facilities. A Fourier transformation was applied to the electrical data of pulsed hyperbaric GMAW to monitor how the mass transfer changes as the ambient pressure increases. It was observed that by using the pulsed welding settings, the general trend of mass transfer could be controlled. Since the droplet transfer frequencies are almost intact, the sources of electrical instability can be easily traced to both the frequency and time domain of the waveforms. Two frequencies were found to be influential. One is around 125 Hz, where the pulsing frequency is set, and the other is 375 Hz, which depends on the mains and converters. The calculated arc power argues that more energy is required to maintain the arc at higher pressures, which is not transferred to the weld pool. Hence, the arc efficiency is expected to be influenced.

Analytical Model, 2D and 3D-FEA

The distributed heat source model can be used to estimate the arc efficiency factor for transverse and perpendicular directions. This is essentially beneficial for finite element modeling where a superposition of at least two heat sources is used. It was shown that by introducing the spatial resolution terms that define how large the distance between each point should be, the developed model could be adapted to the hyperbaric welding case. The cooling curves and weld bead shape as results of welding parameters can be now predicted by the developed models. Moreover, arc constriction at 10 *bar* is less pronounced for He-rich mixtures since both transverse and perpendicular dimensions with respect to the weld bead cross section are larger than that of Ar for the same power source settings. The quantification of the weld bead shaped in this model suggests that using pure He gas or a high He concentration mixture is potentially beneficial, depending on the required mechanical properties.

The most outstanding finding in the modeling is the distribution of the welding arc efficiency. The calculations demonstrated that appointing a unique arc efficiency value for the entire process could be incorrect. It was shown that by splitting the transferred heat in perpendicular and transverse directions, the arc efficiency factor could be higher or lower than the assigned unique value. The calculated arc efficiency using this model can be utilized in the finite element models to regulate the transferred heat source without spending time on a single step of trial and error.

2D simulation of the thermal cycles using partial differential heat transfer equations showed good agreement with the obtained experimental results. Despite simplified boundary conditions, the results show that using such simple software as well as the employed approach can be useful in terms of understanding the effect of weld pool shape. No dominant trend was observed on the variation of $\Delta t_{8/5}$ with respect to the ambient pressure.

In 3D simulations of the welding process, a correlation between analytical and numerical models was established. It was shown that the analytical model of a heat source, calibrated using the actual weld bead geometry, could be implemented in the numerical simulations. Due to the fast computational speed of this analytical method, the required heat source parameters in 3D models can be calculated in fairly a short time.

Electron BackScattered Diffraction (EBSD)

The microstructural and atomic scale (EBSD) studies of the transformed weld metal using five different shielding gases (*i.e.* pure Ar, pure He, pure CO_2, 50%Ar+He and 50%He+CO_2) was performed. It was illustrated that the grain boundary types (e.g. coincidence site lattice (CSL) and high/low angle boundaries) and distribution play an important role in determining the final mechanical properties of the weld metal. The minor variation in the cooling rate and the altered weld pool size and dynamics because of elevating ambient pressure did not reveal any substantial changes in the microstructure of the weld metal. However, the shielding gas plays an important role in determining the final microstructure and mechanical properties of the weld. It was found that the heat flow direction influences the morphology and lattice orientation of the bainite constituents nucleated from the grain boundary. The development of η-fiber ($\langle 001 \rangle \| \mathrm{RD}$) confirms this phenomenon. In general, a combination of low and high misorientation angles as well as low-to-high CSL boundaries number fraction determine the dislocation density and plastic behavior of the weld samples.

Mechanical Properties

The mechanical properties tests showed that pure He as a chamber gas offers the optimum properties required according to the standards (*i.e.* DNV-OS-F101 and DNV-RP-F113), notwithstanding the associated costs. It was observed that the degree of dilution and loss of elements could indirectly alter the fracture toughness of the weld metal through microstructural evolutions. It was also observed that fracture properties are mostly influenced by the microstructure rather than the

presented defects. In one of the samples that associated with the use of 50%He+CO_2 chamber gas, columnar bainite constituent was found. Relatively high ambient pressure and carbon pickup in the S5 sample provided grounds for such phase transformation. Acoustic Emission (AE) sensors were employed to record the generated noises from cracking events. The numbers of AE signals were consistent with the amount of damage in the CTOD tests; less crack resistant materials generated more signals.

Overall

Finally yet importantly, the general overview on the findings and discoveries of this piece of research suggest that replacing the chamber gas by He is promising in terms of the required mechanical properties and welding characteristics. However, understanding the effect of using He as chamber gas in position welding and multi-pass welding entails more investigations.

Chapter 9

Future Work

The proposed approach in predicting the effect of pressure on the arc physics offers the possibility of using this method for even higher pressure. The trend of welding instability should be studied at even higher pressures as soon as new facilities launch in order to verify the predictability of this approach.

The emphasis of this work is on studying the effect of shielding environment and final properties of the weld. The experimental work is mainly carried out at the pressure level of 10 *bar*. Although successful alternatives were screened out of the proposed mixtures (*e.g.* pure He) and it was predicted that the pressure level should have imperceptible effect on the arc characteristics, high pressure trials need to be settled and investigated in detail. The diffusion behavior of He gas, which possesses a small atom, is not yet well understood under high ambient pressure conditions.

Moreover, due to the fact that the evolution of brittle phases in welding (*e.g.* M-A phase) is a function of thermal cycles and that different shielding environment presumably results in different heat input, the presence of such phases requires more investigation should the chamber gas be optimized. The effect of multi-pass deposition and inter-pass temperature should definitely be studies prior to gas selection.

The physical properties of the pure gases and especially the gas mixtures are not well practiced ever since. There is a great enthusiasm among the welding communities and physicists for such data based on which, better models can be proposed. The effect of pressure on arc efficiency factor was not studied in the present work, due to lack of befitting data, which requires more examinations.

In the modeling phase, a quantitative analysis of the effect of pressure and shielding environment on the heat source design was performed. The defined welding heat sources in this work are not used for multi-pass constructions so far, which is craved for developing the microstructural models. The implementation of such heat sources in multi-pass complex depositions requires more investigation. WeldSimS simulation code was used to implement the welding models as it appears in the accompanying paper IV. The root-pass and multi-pass constructions should be modeled in this software for further verifications.

The foundation of the analytical point heat source model is on 2D and weld cross section. However, this model potentially encompasses the capability of predicting along the third dimension providing that the model is followed up and

new equations are devised. Better definition of double ellipsoidal heat source model can be presented should the third dimension emerge.

A large number of fractured samples from mechanical properties tests entail more work on fractography and microscopy. Running EBSD studies on the fractured samples to determine the effect of orientations and grain boundaries on the crack initiation and trajectory is truly desired.

The effect of weld pool chemical composition and phase evolution as a function of pressure should be studied more in detail. In addition, position welding in hyperbaric condition for verifying the robustness of the circumferential welding is desired from industrial applications viewpoint.

By the time the new facilities launch in Killingøy, Haugesund, more research and development activities should be devised. For instance, very high pressure and temperature properties and behavior of different gas mixtures can be experimented.

References

[1] Jones GR. High pressure arcs in industrial devices: diagnostic and monitoring techniques: Cambridge University Press, 1988.

[2] Nixon JH. Underwater Repair Technology: Abington Publ., 2000.

[3] Richardson IM. Properties of the constricted gas tungsten (plasma) welding arc at elevated pressures: Cranfield Institute of Technology, 1991.

[4] Proceedings of the International Conference on Offshore Mechanics and Arctic Engineering (OMAE). In: OMAE Conference Committee, American Society of Mechanical Engineers. Offshore Mechanics, Arctic Engineering Division, American Society of Mechanical Engineers, editors: American Society of Mechanical Engineers, 2000.

[5] Apeland KE, Berge JO, Verley R, Armstrong M, Woodward N. Deepwater remote welding technology for pipeline repair and hot-tapping. Offshore 2006;66:52.

[6] Woodward N, Knagenhelm HO, Berge JO, Verley R, Armstrong M. Hyperbaric GMA welding for contingency repair using a fillet welded sleeve at 1,000 m water depth, Proceedings of the International Offshore and Polar Engineering Conference, 2007, p.3403.

[7] Woodward N, Fostervoll H, Akselsen OM, Ahlen CH, Berge JO, Armstrong M. Evaluation of welding procedures and consumables for hyperbaric GMAW for diverless retrofit tee hot-tap applications. International Journal of Offshore and Polar Engineering 2008;18:149.

[8] Fostervoll H, Woodward N, Akselsen OM. The effects on process performance of reducing the pressure from 36 to 1bar in hyperbaric mig welding. OMAE 2009, 2009. p.197.

[9] Richardson IM, Woodward NJ, Billingham J. Deepwater Welding for Installation and Repair - A Viable Technology? ISOPE. Kitakyushu, Japan, 2002. p.295.

[10] Sakakibara J, Hamasaki M. Study on Underwater Dry Hyperbaric TIG Welding, Part I: Effect of Ambient Pressure on Electrode Erosion and Arc Characterisitcs. J. High Temp. 1983;9:27.

[11] Nixon JH, Allum CJ, Lowes JM. Underwater Welding - A Review. Conference Internationale - Penetration Sous-Marine.;Paris, Fr, 1982. p.147.

[12] Richardson IM, Nixon JH, Nosal P, Hart P, Billingham J. Hyperbaric GMA Welding to 2,500m Water Depth. Joint International Conference ETC/OMAE. New Orleans, USA, 2000.

[13] Cotton HC. Welding Under Water And in The Splash Zone - A Review. Founding, welding, production (FWP) journal 1983;23(9), p.63.

[14] Richardson IM, Nixon JH. Deepwater hyperbaric welding - initial process evaluation. ISOPE 1997. Honolulu, USA, 1997. p.493.

[15] Svensson LE. Control of microstructures and properties in steel arc welds: CRC Press, 1994.

[16] Jeffus LF. Welding: principles and applications: Thomson/Delmar Learning, 2002.

[17] Liu S, Olson DL, Siewert TA. ASM handbook. Vol. 6: Welding, brazing and soldering: ASM International, 1993, p.69.

[18] Stenbacka N, Persson KA. Shielding gases for gas metal arc welding. Weld J 1989;68:41.

[19] Dillenbeck VR, Castagno L. Effects of Various Shielding Gases and Associated Mixtures in GMA Welding of Mild Steel. Welding Journal (Miami, Fla) 1987;66:45.

[20] Schnick M, Dreher M, Zschetzsche J, Fuessel U, Spille-Kohoff A. Visualization and optimization of shielding gas flows in arc welding. Weld World 2012;56:54.

[21] Larson NE, Meredith WF. Shielding Gas Selection Manual. Union Carbide Industrial Gases Technology Corp. , 1990.

[22] Hilton DE, Norrish J. Shielding gases for arc welding. Weld. Met. Fabr. 1988;56:189.

[23] Shackleton DN, Lucas W. Shielding Gas Mixtures for High Quality Mechanized GMA Welding of Q&T Steel. Welding Journal (Miami, Fla) 1974;53:537s.

[24] Iota V, Yoo C-S. Phase Diagram of Carbon Dioxide: Evidence for a New Associated Phase. Phys Rev Lett 2001;86:5922.

[25] Reid RC, Prausnitz JM, Poling BE. The properties of gases and liquids, fifth ed. McGraw-Hill, 1987.

[26] Babu SS. Thermodynamic and kinetic models for describing microstructure evolution during joining of metals and alloys. International Materials Reviews 2009;54:333.

[27] Nishiyama N, Terashima H, Hart PHM. Effect of Al in C-Mn Steels on Microstructure and Toughness of Submerged-Arc Weld Metal (Report 1).

Yosetsu Gakkai Ronbunshu/Quarterly Journal of the Japan Welding Society 1984;2:533.

[28] Homma H, Ohkita S, Matsuda S, Yamamoto K. Improvement of HAZ Toughness in HSLA Steel by Introducing Finely Dispersed Ti-Oxide. Welding Journal (Miami, Fla) 1987;66:301. s.

[29] Hillert M. Phase Equilibria, Phase Diagrams and Phase Transformations: Their Thermodynamic Basis: Cambridge University Press, 2008, p.92.

[30] Christian JW. The Theory of Transformations in Metals and Alloys (Part I + II), 3rd Edition: Elsevier Science, 2002.

[31] Porter DA, Easterling KE. Phase transformations in metals and alloys: Chapman & Hall, 1992, p. 91.

[32] Babu SS, David SA, Vitek JM, Mundra K, DebRoy T. Development of macro- and microstructures of carbon, manganese low alloy steel welds: inclusion formation. Mater Sci Tech-Lond 1995;11:186.

[33] Babu SS, Bhadeshia HKDH. Transition from bainite to acicular ferrite in reheated Fe, Cr weld deposits. Mater Sci Tech-Lond 1990;6:1005.

[34] Jones SJ, Bhadeshia HKDH. Kinetics of the simultaneous decomposition of austenite into several transformation products. Acta Mater 1997;45:2911.

[35] Yu X. Characterization and Modeling of Heat Affected Zone Microstucture in a Blast Resistant Steel. Welding Engineering, vol. Master of Science: Ohio State University, 2009.

[36] Cho MH, Farson DF. Simulation study of a hybrid process for the prevention of weld bead hump formation. Miami, FL, ETATS-UNIS: American Welding Society, 2007.

[37] Subramaniam S, White D. Effect of shield gas composition on surface tension of steel droplets in a gas-metal-arc welding arc. Metallurgical and Materials Transactions B 2001;32:313.

[38] Heiple, CR, Roper, JR. Mechanism for minor element effect on GTA fusion zone geometry. Welding Journal 1982, 61(4), p.97.

[39] Mitra U, Eagar TW. Slag-metal reactions during welding: Part II. Theory. Metallurgical Transactions B 1991;22:73.

[40] Finn R. Capillary Surface Interfaces. American Mathematical Society 1999;46:770.

[41] Malkin A. The effect of Pressure and Sheilding Gas Composition on Hyperbaric GMAW Process in the Pressure Range 1 to 10 bar Absolute. vol. Master of Science: Cranfield University, 1988.

[42] Gaskell DR. Introduction to the thermodynamics of materials: Taylor & Francis, 2003, p.105.

[43] Richardson IM. Underwater Arc Welding - A Survey of Process Behaviour. Weld Rev. 1989:11.

[44] Matsunawa A, Nishiguchi K. Arc Characteristics in High Pressure Argon Atmosphere. International Conference of Arc Physics and Weld Pool Behaviour. London, 1979.

[45] Hajossy R, Pastva P, Morva I. Ignition of a welding arc during a short-circuit of melted electrodes. Journal of Physics D: Applied Physics 1999;32:1058.

[46] Kou S. Welding metallurgy: Wiley-Interscience, 2003.

[47] Connor LP, O'Brien RL, Society AW. Welding Handbook: Welding processes: American Welding Society, 1991.

[48] Woodward N. Feasibility Study into Deep Water Pipeline Repair. 2009. IsoTek internal report no. OPS-19-01.

[49] Allum CJ. Characteristics and structure of high pressure 0–42 bars welding. vol. PhD: Cranfield Institute of Technology, 1982.

[50] Allum CJ. Effect of Pressures on Arcs. 1983. p.171.

[51] Allum CJ, Pinfold BE, Nixon JH. Some Effects of Shielding Gas Flow on Argon-Tungsten Arcs Operating in High Pressure (1 to 14 bars) Environments. Welding Journal (Miami, Flo) 1980;59:199. s.

[52] Nixon J, Billingham J. A survey of underwater welding techniques. Endeavour 1987;11:143.

[53] American Petroleum Institute, Dept. APIP. Specification for line pipe, API Spec 5L, 1992.

[54] Review of Construction Technique and Pipeline Materials for Waimakariri Outfall. Singapore: Aker Kværner, Report No 4409-PLR-002, 2003.

[55] Lambert-Perlade A, Gourgues AF, Besson J, Sturel T, Pineau A. Mechanisms and modeling of cleavage fracture in simulated heat-affected zone microstructures of a high-strength low alloy steel. Metallurgical and Materials Transactions A: Physical Metallurgy and Materials Science 2004;35:1039.

[56] Akselsen OM, Fostervoll H, Hårsvær A, Aune R. Weld metal mechanical properties in hyperbaric GTAW of X70 pipeline. International Journal of Offshore and Polar Engineering 2006;16:233.

[57] Li C, Wang Y, Han T, Han B, Li L. Microstructure and toughness of coarse grain heat-affected zone of domestic X70 pipeline steel during in-service welding. J Mater Sci 2011;46:727.

[58] Hwang B, Kim YM, Lee S, Kim NJ, Ahn SS. Correlation of microstructure and fracture properties of API X70 pipeline steels. Metallurgical and Materials Transactions A: Physical Metallurgy and Materials Science 2005;36:725.

[59] Nyhus B, Polanco ML, Ørjasæther O. SENT specimens an alternative to SENB specimens for fracture mechanics testing of pipelines, Proceedings of the International Conference on Offshore Mechanics and Arctic Engineering - OMAE, vol. 3, 2003. p.259.

[60] Recommended Practice for Conducting Drop-Weight TearTests on Line Pipe. Washington D.C.: API, 1996.

[61] Shin SY, Gong G, Kim S, Lee S. Analysis of fracture toughness in the transition temperature region of API X70 pipeline steels rolled in two-phase region. Metallurgical and Materials Transactions A: Physical Metallurgy and Materials Science 2007;38:1012.

[62] Martín-Meizoso A, Ocaña-Arizcorreta I, Gil-Sevillano J, Fuentes-Pérez M. Modelling cleavage fracture of bainitic steels. Acta Metall Mater 1994;42:2057.

[63] Onsøien MI, M'Hamdi M, Mo A. A CCT Diagram for an Offshore Pipeline Steel of X70 Type. The Welding Journal 2009;88:1.

[64] Spivakov VI, Orlov EA, Litvinenko PL, Nogovitsyn AV. Kinetics of Austenite Transformation and Bainite Structure Formation during Strain-Heat Hardening of Low-Perlite Steel X70 (X65) API 5L Gr X-60, API 5L Gr X-70) Plates for Gas Pipelines. Metall. Min. Ind. 2010;2:39.

[65] Thaulow C, Ranestad Ø, Hauge M, Zhang Z, Toyoda M, Minami F. FE calculations of stress fields from cracks located at the fusion line of weldments. Eng Fract Mech 1997;57:637.

[66] Minami F, Ohata M, Toyoda M, Tanaka T, Arimochi K, Glover AG, North TH. Yield strength mis-match effect on fracture performance of girth welded joints of grade 550 pipeline steel. Proc. 14th Int. Conf. on Offshore Mechanics and Arctic Engineering, vol. 5. Copenhagen, 1995. p.145.

[67] Thaulow C, Zhang ZL, Hauge M, Burget W, Memhard D. Constraint effects on crack tip stress fields for cracks located at the fusion line of weldments. Comp Mater Sci 1999;15:275.

[68] Nevasmaa P, Cederberg M, Valipas M. Weldability of Accelerated-Cooled (AcC) High Strength TMCP Steel HT50. VTT Res., 1992.

[69] Dolby RE. HAZ Toughness of Structural and Pressure Vessel Steels - Improvement and Prediction. Weld J (Miami Fla) 1979;59:225s.

Paper I

Statistical Analysis of the Arc Behavior in Dry Hyperbaric GMA Welding from 1 to 250 *bar*.

Amin S. Azar, Neil Woodward, Hans Fostervoll, Odd M. Akselsen.

Journal of Materials Processing Technology 212 (2012) 211– 219.

Journal of Materials Processing Technology 212 (2012) 211–219

Contents lists available at SciVerse ScienceDirect

Journal of Materials Processing Technology

journal homepage: www.elsevier.com/locate/jmatprotec

Statistical analysis of the arc behavior in dry hyperbaric GMA welding from 1 to 250 bar

Amin S. Azar[a,*], Neil Woodward[b], Hans Fostervoll[c], Odd M. Akselsen[a,c]

[a] Department of Engineering Design and Materials, NTNU, Trondheim, Norway
[b] Isotek Electronics Ltd, Leeds, England, UK
[c] SINTEF Materials and Chemistry, Trondheim, Norway

ARTICLE INFO

Article history:
Received 4 August 2011
Received in revised form 9 September 2011
Accepted 12 September 2011
Available online 16 September 2011

Keywords:
Hyperbaric welding
Stochastic approach
GMAW
Ambient pressure
Fourier transformation

ABSTRACT

In this paper, mathematical approaches were developed for predicting the hyperbaric GMAW process arc behavior and stability. The variation of stochastic parameters is related to the electrical stability that can be resolved into a number of varying parameters. The results show that most of the arc instability can be traced to the frequency domain of the voltage or current waveform. Uncorrelated current and voltage wave frequencies at higher pressures are found to have a great influence on process stability.

1. Introduction

Acquisition and analysis of real-time electrical signals have been reported by a number of authors including Subramaniam et al. (1998). Because these data are produced in a sequence with defined intervals, Witt (2007) provided the possibility to consider them as stochastic variables and analyze the dataset as a time-series. Diongue et al. (2008) modeled time-series by developing the theory of seasonality that resulted in visualization of recurrent components of a waveform. Such analyses may form the basis of a model for further predictions. However, Dilthey et al. (1996) found that a universal model can be too intricate with regard to monitoring and predicting the effect of the welding parameters involved.

Jones (1988) has described that welding under high pressure conditions is often required in a variety of industries. One example is subsea pipeline tie-ins and hot tapping in the oil and gas industry. Such a welding process should be performed in a sustainable and reliable way, meeting the standard metallurgical and mechanical requirements for a welded joint. Performing the welding operation under the water without protecting the weld pool from water media can suffer from low toughness and ductility as well as low process productivity. Dry hyperbaric welding was developed to ameliorate the characteristics of wet welding. Nixon (1995) has defined different types of dry hyperbaric welding which generally require a chamber to protect and seal the workspace from seawater.

Waller et al. (1990) proposed implementing high-speed charge-coupled device (CCD) cameras inside the welding chamber to study metal transfer phenomenon. However, existing chambers do not offer enough space for such a device, and a suitable instrument for very high pressures does not exist. Moreover, this kind of data recording can also be very costly at the industrial scale. Thus, alternative methods are sought. According to Mazzaferro and Machado (2009), monitoring the welding voltage and current waveforms using stochastic approaches can be a reasonable substitute to correlate the behavior of a specific parameter with the stability of the welding process. However, the sampling frequency should be sufficiently high in order to achieve statistical significance. McLarty and Bahna (2009) discussed the effects of sampling frequency on waveform approximation and showed that high sampling frequency results in a longer analysis time, while lower frequencies result in data loss. Nevertheless, Zhu (2006) described the existence of a specific frequency above which the analyses do not show any major change in any subset of the waveforms, while the minimum statistical significance is met, which is an indication of ergodic behavior.

Oliveira and Werlang (2007) defined ergodicity of a signal when the frequency of a data collection is high enough to meet the statistical significance. They assigned "ergodic" to a process in which every sequence or sizable sample is equally representative of the

* Corresponding author at: Norwegian University of Science and Technology (NTNU), Department of Engineering Design and Materials, Richard Birkelands Vei 2B 7491, Trondheim, Norway. Tel.: +47 96833668.
E-mail address: amin.azar@ntnu.no (A.S. Azar).

0924-0136/$ – see front matter © 2011 Elsevier B.V. All rights reserved.
doi:10.1016/j.jmatprotec.2011.09.006

entire process. Alfaro et al. (2006) have applied the definition to the processes in which an event recurs with a dominant frequency, as in welding, where metal transfer occurs periodically.

A stable process could also show stationary behavior, which means that calculated stochastic parameters are similar to those of the "time-shifted" series. Once the welding process stabilizes after the ignition phase, such behavior can be observed. Newland (2005) argues that once a welding process shows both ergodic and stationary characteristics, it can be monitored using any subset of waveforms with a fixed number of samples. Thereafter, the statistical parameters of each subset can be compared to the adjacent set to study the instabilities during the process.

In the dry hyperbaric GMA welding case, Fostervoll et al. (2009) used the most outstanding statistical features on the entire process regardless of its variation in subset waves. Although the general trend was visualized, the optimization of the parameters and significance of the calculation could not be verified. The objective of this paper is to report on more advanced statistical analyses and signal processing techniques to ensure the trustworthiness of the trends.

2. Background

2.1. Stationary and ergodic processes

Box et al. (2008) defined a stochastic process as an infinite ensemble of random variables. Let Ω be the sample space that consists of members $\theta \in \Omega$. A continuum or discrete-time stochastic process can be denoted by $X(t,\theta)$, where there is one and only one random value for each time t.

Because θ is a random variable, it can take any real positive nonzero value from 1 to n. The number n shows how many times the process is repeated, and it is called the "realization" of the process. If these conditions are met, the group of $X(t,\theta)$ is representative of a single process.

Moreover, each random process exhibits a single probability distribution function (PDF), and a set of these functions represents $X(t)$ in particular. The number of functions that take the value between x and $x+\mathrm{d}x$ form the first probability distribution $f_X(x,t)\mathrm{d}x$. The joint probability distribution at times t_1 and t_2 can then be defined as $f_{XX}(x_1,t_1;x_2,t_2)\mathrm{d}x_1\mathrm{d}x_2$, and the third, fourth and subsequent distributions can be defined in the same way; representing a random process. The value of each function is positive, and the joint integration of all the functions is unity. In addition, it is assumed that PDFs are dependent on time intervals. Engelberg (2007) showed that if the following condition is met, the stochastic process will be of a stationary type:

$$f_X(x,t) = f_X(x), \quad f_X(x_1,t_1;x_2,t_2) = f_{XX}(x_1,t_1+\varepsilon;x_2,t_2+\varepsilon) \tag{1}$$

More restrictively, Porat (1994) stated that the ergodic process can be calculated as the expected values at time averages over a single instance of the stochastic process:

$$E(X(t,\theta)) = \lim_{T\to\infty}\frac{1}{T}\int_{-T/2}^{T/2} X(t,\theta=\theta_0)\mathrm{d}t \tag{2}$$

$$E(X(t,\theta)X(t+\Delta t,\theta)) = \lim_{T\to\infty}\frac{1}{T}\int_{-T/2}^{T/2} X(t,\theta=\theta_0)X(t+1,\theta=\theta_0)\mathrm{d}t \tag{3}$$

where the left hand sides of the equations are the expectations over all θ and the right hand sides are the expectations of a particular θ. If the time average is used in this way, the stochastic process must be stationary.

2.2. The auto-correlation function

According to Tabachnick and Fidell (2007), auto-correlation is a mathematical representation of the degree of similarity between a given time series and a lagged version of itself over successive time intervals. It gives the measure of the correlation of $X(t)$ with itself at two different times and is defined as

$$R_{XX}(t_1,t_2) \equiv E(X(t_1)X(t_2)) \tag{4}$$

If $X(t)$ is stationary, the auto-correlation could be defined as a function of time interval variable τ:

$$R_{XX}(\tau) \equiv E(X(t)X(t+\tau)) = \lim_{T\to\infty}\frac{1}{T}\int_{-T/2}^{T/2} X(t)X(t+\tau)\mathrm{d}t \tag{5}$$

A stochastic process where $E(X(t)) = \mu$ (μ: statistical average) and $R_{XX}(t_1,t_2) = R_{XX}(\tau)$ is called *wide sense stationary*. It is assumed that the welding waveforms are of this kind. According to the definition of an ergodic process, Eq. (5) shows that the ensemble average (right hand side) can be used to represent the time average (left hand side). The following equation describes this condition:

$$R(\tau) = \iint_{-\infty}^{\infty} x_1 x_2 f_{XX}(x_1,x_2;\tau)\mathrm{d}x_1\mathrm{d}x_2 \tag{6}$$

If x_1 and x_2 are not correlated, $f_{XX}(x_1,x_2;\tau) = f_X(x_1)f_X(x_2)$, which zeros Eq. (6). In other words, a perfectly random process has an auto-correlation value equal to zero. In addition, the auto-correlation of a periodic function is periodic, with the same period as events in the original signal. The auto-correlation function evaluates the time dependent behavior of a stochastic process.

2.3. Power spectral density (PSD)

Brockwell and Davis (2002) showed that the auto-correlation function does not resolve the periodicities of a waveform because it is periodic itself. Moreover, the power or energy of the waveform has not been taken into account because the auto-correlation function is only concerned with the statistical average of the waveform. As a result, the power state of the time series over a range of frequencies (ω) could be visualized by applying the Fourier transformation of the waveform:

$$\Phi(\omega) = \left(\int_{-\infty}^{\infty} f_X(t)\mathrm{e}^{-2\pi i\omega t}\mathrm{d}t\right)^2 \tag{7}$$

Nevertheless, because the time-series has been recorded discretely, the Fourier integral does not exist. Alternatively, according to the properties of the auto-correlation function and the Wiener–Khinchin theorem defined by Strube (1985), the power spectral density (PSD) can be calculated by applying the Fourier transform on the auto-correlation function.

$$\mathrm{PSD}_{\mathrm{average}} = \lim_{T\to\infty}\frac{1}{T}\int_{-T/2}^{T/2} E(|X(t)|^2)\mathrm{d}t = \int_{-\infty}^{\infty} \mathcal{F}(R(\tau))(\omega)\mathrm{d}\omega \tag{8}$$

According to Eq. (8), if the waveform being analyzed is the welding current, the standard deviation of the signal ($|I(t)|^2$) will represent the average power spectral density between the time set-points ($-T$, T). Moreover, according to Luksa (2006) and Joseph et al. (2003), the momentary arc power can be calculated by multiplying the average PSD with the momentary arc resistance. At high sampling frequencies, the average values can be calculated using

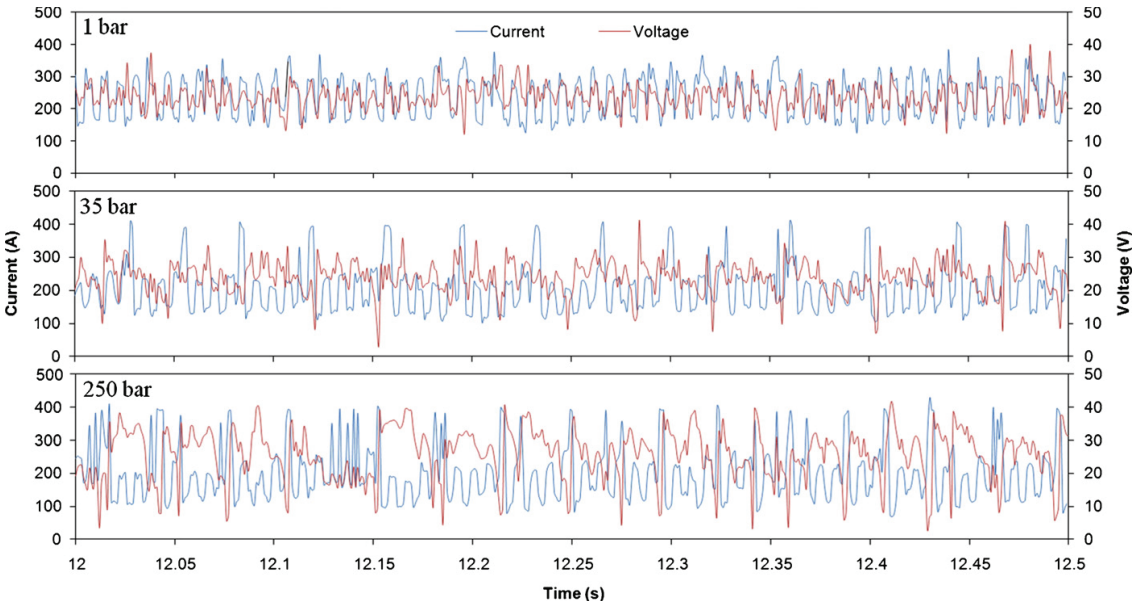

Fig. 1. Current and voltage waveforms of 1, 35 and 250 bar.

the momentary voltage and current samples given by the following equation:

$$\overline{P_m} = \sum_{i=1}^{n} \frac{I_i \cdot V_i}{n} \tag{9}$$

where n is the sampling frequency, i is the sample number and I_i and V_i are the arc current and voltage respectively.

3. Data significance

The analyses can be carried on the signals that are statistically stationary to verify the ergodic hypothesis. For this purpose, the starting point is the mean and deviation calculations that have been carried out by other authors. These data can be used afterwards for computing the auto-correlation function according to the definition of a *wide sense stationary* process in Section 2.2. Therefore, the time (T) average of the current and the voltage are as shown below, when the number of realizations (n) are approaching infinity:

$$\bar{V} = \lim_{n\to\infty} \frac{1}{T} \int_0^T V(t)\mathrm{d}t \quad \text{and} \quad \bar{I} = \lim_{n\to\infty} \frac{1}{T} \int_0^T I(t)\mathrm{d}t \tag{10}$$

To examine the process instability, the standard deviation should be calculated for discrete samples using the formula:

$$\sigma_{V,I} = \sqrt{\frac{1}{n}\sum_{i=1}^{n}(\theta_{V,I} - \mu_{V,I})^2} \tag{11}$$

The fluctuation amplitude of voltage and current can be defined as:

$$V_f = V_i - \bar{V} \quad \text{and} \quad I_f = I_i - \bar{I} \tag{12}$$

where the indices f and i represent the fluctuation and instantaneous values, respectively. Moreover, a normalized measure of data-point dispersion can be calculated using the voltage and current coefficients of variation (C_v):

$$\widehat{V}_f = \frac{\sigma_V}{\bar{V}} \quad \text{and} \quad \widehat{I}_f = \frac{\sigma_I}{\bar{I}} \tag{13}$$

where $\widehat{V}_f$ and $\widehat{I}_f$ are the C_v values of voltage and current respectively. Following Eqs. (12) and (13), the power input variation of each process is the product of $\widehat{V}_f \cdot \widehat{I}_f$ as calculated in Section 5. In the following sections, the sampling conditions and the welding process will be scrutinized according to the procedures used by Alfaro et al. (2006).

4. Experimental details

The datasets were acquired from several hyperbaric gas metal arc process experiments at different ambient pressures. The welding parameters including the electrical inputs were all set to constant values and verified. The control unit (Isotek Equipment ID: WPC1PA10) of the power supplies (Fronius TPS450×3, 200 V OCV) is an adaptive pulsed welding unit. The settings on the user interface display the current and the voltage and are recorded during the process. The current fluctuates adaptively around a set-point to provide the system with a specific power input. The power input varies proportional to the variations in voltage and current C_v. The initial current is introduced empirically based on the visual quality of the welds. Voltage and current recordings provide the waveforms upon which further analyses are based.

Pulsed mode bead-on-plate welds were performed based on a pulsing frequency of 125 Hz (8 ms period), with a 1.0 mm diameter metal cored HBQ wire, fed continuously at the speed of 8.0 m/min, and at a welding speed of 7.0 mm/s. The torch stand-off was 10 mm at ambient pressure levels from 1 to 250 bar. The chamber was pressurized using 99.98% pure argon gas after several initial pressurizations and depressurizations to reduce the ambient oxygen level. The data sampling frequency was set to 1 kHz. Because the weld bead was sufficiently long, the data could be divided into 40 realizations, each with a duration of 500 ms. Each realization was

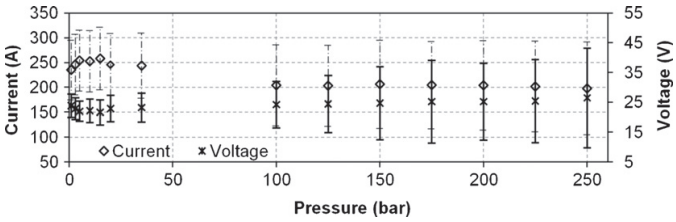

Fig. 2. Average voltage and current of process at different pressures, error bars represent standard deviations.

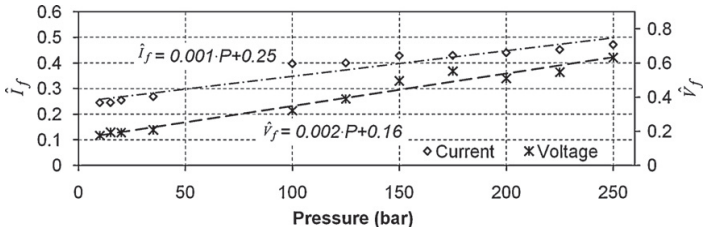

Fig. 3. Coefficient of variation of current and voltage at different pressures.

repeated 40 times to provide statistical significance. Thus, each realization shows the average voltage and current based on the window described.

5. Results

The current waveforms of the welding process in three different pressure ranges are shown in Fig. 1. The magnitude of the current peaks increases as the pressure rises. Statistically, the standard deviation of the current increases with pressure, as shown by the error bars in Fig. 2.

Fig. 3 depicts the trend lines of coefficient of current and voltage variation using Eqs. (10)–(13). It can be seen that both coefficients are increasing as pressure increases, indicating that the waveforms are fluctuating more severely at higher pressures. According to Eqs. (12) and (13), the coefficient of variation of power $\widehat{P}_E$ can be calculated from the product of the regressions in Fig. 3:

$$\widehat{P}_E = 2 \times 10^{-6} P^2 + 6.6 \times 10^{-4} P + 0.04 \quad (14)$$

where P is the ambient pressure. Note that data at three pressures (1, 3, 5 bar) were excluded from the regression due to a different dominant trend, as observed in Fig. 2. The variation of $\widehat{P}_E$ with pressure is shown in Fig. 4. The increasing fluctuation regime reveals the deterioration trend of the process as the ambient pressure increases. The deterioration in transient power stability is negligible in the early stages of a pressure increase, though the trend becomes linear in the higher pressure range. However, the arithmetic average of momentary arc power is very much dependent on the arc resistance rather than the momentary current. Fig. 5 shows the momentary arc resistance and momentary arc power averages at different pressures. It shows that the arc resistance is almost in the same level at lower pressures while showing increments as pressure increases.

Fig. 6 shows the calculated ensemble averages of each process, revealing that the processes stabilize after an initial stage. For the sake of comparability, the data gathered prior to stabilization were eliminated in further analyses. The existence of such data shows a departure from the stationary process assumption.

Once the process is stationary, the auto-correlation function can be calculated. Fig. 7 shows the correlograms of welding current signals at different pressures. The auto-correlation function decays exponentially as the time interval increases. When the auto-correlation function approaches to zero, the data-points become uncorrelated stochastically. As the ambient pressure increases, the decay rate increases, and the waveform becomes uncorrelated within smaller time intervals. The 95% confidence bands are drawn in the 1 bar and 250 bar subfigures. The decaying trend is quite different for peak and base currents. Peak currents become uncorrelated at longer time intervals compared to base currents. The same analysis was performed for voltage waveforms (not included here), which resemble those of the current diagrams unless otherwise indicated, as discussed later in this section.

As mentioned in Section 2.3, the power spectral density is the Fourier transformation of the auto-correlation function. Figs. 8 and 9 show the PSDs at different pressures.

PSDs visualize the periodic recurrence of mass transfer events during welding. Such cyclic variations are referred as "seasonality" in statistics. The underlying wave components will also be

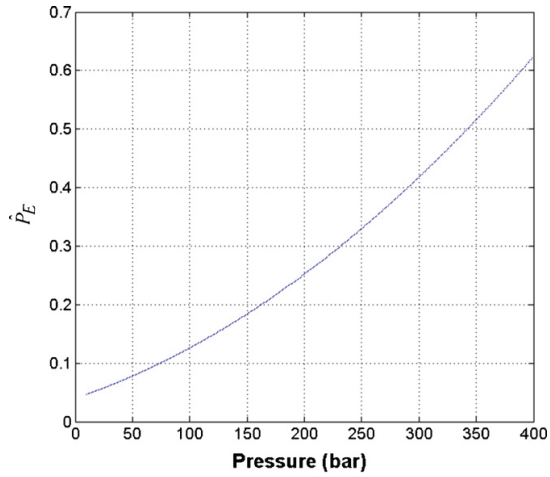

Fig. 4. The coefficient of variation of power for the dry hyperbaric GMA welding process at different pressures.

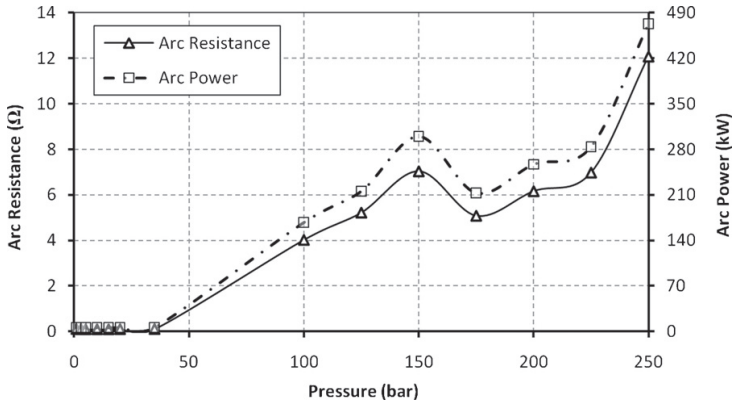

Fig. 5. Average momentary arc resistance and arc power at different pressures.

sorted with respect to their frequency range in PSD diagrams as proposed by Norton and Karczub (2003). Fig. 8 shows a spectral density trend of voltage at 225 bar. It is observed that at lower pressures, the voltage PSDs almost follow the same pattern as their corresponding current PSDs. However, they show more lower frequency components than the current spectrum when the pressure is high (as shown in Figs. 8 and 9). It is expected that because there is a limited correlation between voltage and current seasonality at higher pressures, the molten metal transfer undergoes a non-systematic behavior mentioned by Richardson et al. (2000). The deviation of seasonality incompatibility between voltage and current waveforms started at about 125 bar.

Fig. 10 depicts the variation of peak frequencies with welding time. It is obvious that the dominant frequencies of 100–150 Hz and 350–400 Hz do not change as the pressure increases. However, at higher pressures, even the main wave constituents are buried in the surrounding high amplitude signals, which are representative of arc instability.

Fig. 11 depicts the weld cross section micrographs at higher pressure range. Fostervoll et al. (2009) presented the lower pressure range micrographs earlier.

6. Discussion

Alfaro et al. (2006) applied the same approach to the study of dip and spray transfer methods of welding. They showed that a characteristic droplet frequency exists for the spray mode of transfer.

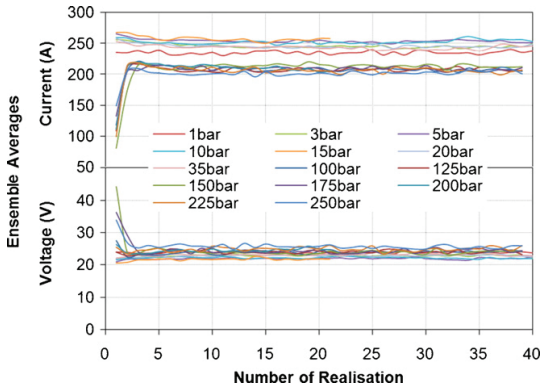

Fig. 6. Ensemble averages of voltage and current for each realization at different pressures.

Fig. 5 shows the average arc transient power at defined pressure levels. As it can be seen, the required power for maintaining the arc follows an increasing regime as ambient pressure increases. If other welding parameters were kept constant, the weld bead should have shown larger dimensions at higher pressure due to increased heat input and arc power. Nevertheless, near constant weld bead shape (Fig. 11) proposes that the arc efficiency factor is relatively low at high pressure range as a result of excessive energy loss.

In order to present the underlying coherency of random data, the ergodicity of the waveforms is investigated. Fig. 6 shows that the ensemble averages of the waveforms at different pressures are statistically stable, at least in higher realizations. The fluctuating behavior of ensemble averages at lower realizations shows unsystematic metal transfer in the ignition phase.

Hu and Tsai (2007) performed an extensive simulation on heat and mass transfer in GMA welding. Part of their studies showed how the current is distributed around the droplet while it is forming and transferring. They recorded the instances that special events (e.g. metal transfer, arc ignition and extinction) occurred accordingly. Fig. 12 shows the compatibility of statistical analysis with their findings. For a typical density spectrum of the current, the energy is more concentrated at around 100–150 Hz because the pulsing frequency is 125 Hz. This interval represents the frequency of the formation and detachment of the droplet. The highest spike in Fig. 12 represents the frequency of the highest current density distributed around the droplet. They reported that the current flows through the droplet before detaching and flows around the droplet after detachment. Two tributaries of current flow reunify once the droplet reaches the weld pool to form the weld bead. At the same time, another peak appears on the frequency spectrum field of the current reflecting the higher current density at shorter anode to cathode distance. The second peak was displayed at around 375 Hz in all of the experiments. Johnson et al. (1991) and Mazzaferro and Machado (2009) denoted such peaks as the third harmonic of the three-phase rectified frequency due to the transformer type. This frequency could be recorded when the arc exists between the anode and the cathode, but there is no droplet transfer event. Nevertheless, Joseph et al. (2003) pointed out that the power density of these peaks is fairly low, which may not lead to higher power transfer.

Comparison of the data in Fig. 9 reveals that the governing droplet transfer regime does not change as the pressure increases. However, if the ambient pressure is increased, more energy is concentrated in the frequency region below 100 Hz, which could be explained as the existence of less frequent droplet transfer events. Mazzaferro and Machado (2009) reported that the peaks at lower

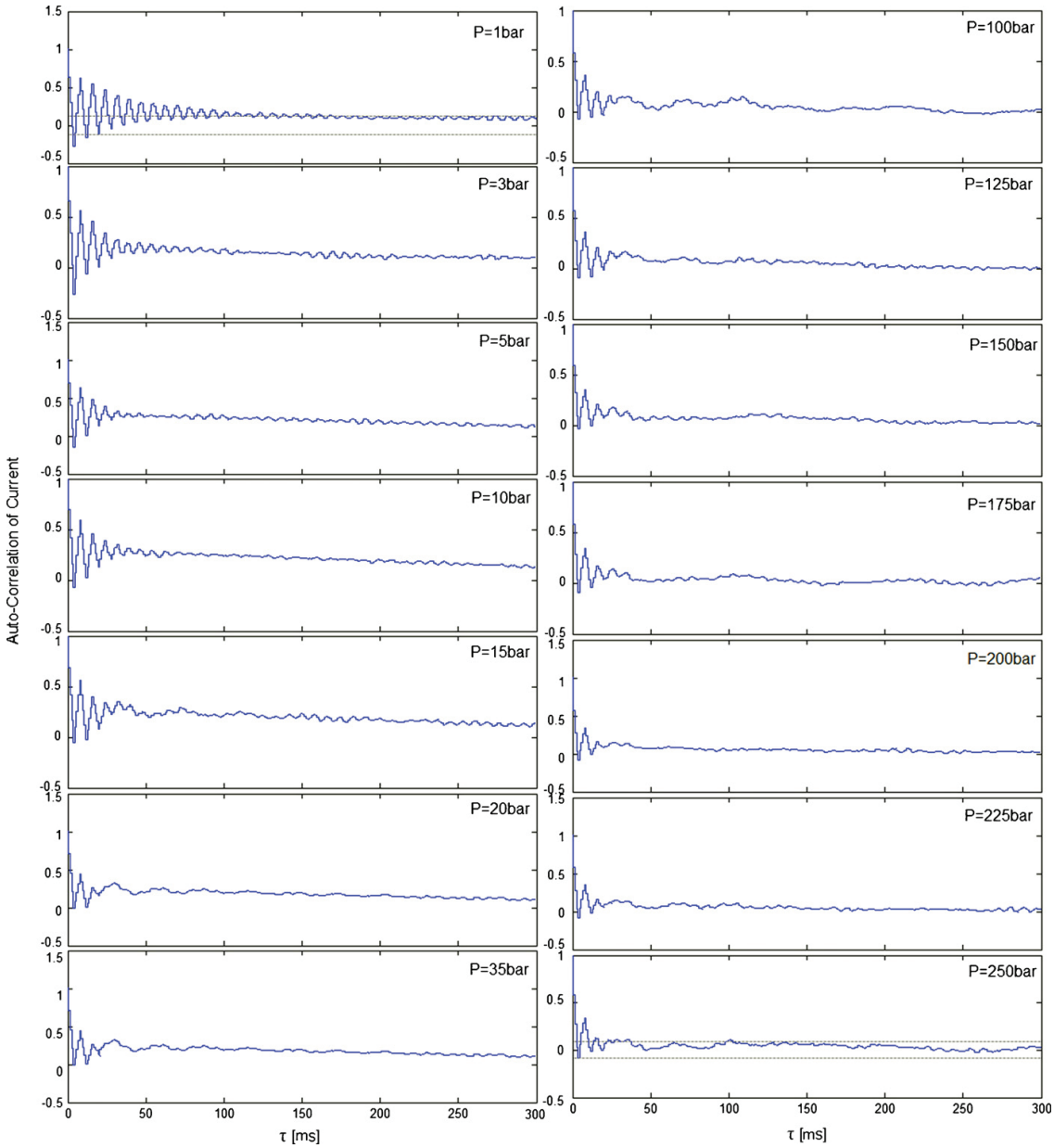

Fig. 7. Correlograms of current waveforms in different pressures.

frequencies are evidence of the short circuiting effect that can be observed in the time domain as well (see Fig. 1). Moreover, the energy state of the waveform increases outside the dominant frequencies, which leads to inappropriate detachments of molten metal at any undefined pulsed frequency. In addition, the increased power needed for arc formation at higher pressures, which is shown in Fig. 4, could be observed in Fig. 10 in terms of the higher spectral density (more shades of red color).

From Fig. 9, it can be deduced that lower frequencies appear as the pressure increases. The reason lies in very abrupt and severe fluctuation of the current and the very low pulse period. In conventional GMAW, the voltage and current are linked by negative static characteristic of the power source such that when the current peaks, the voltage falls and vice versa. Very low frequencies that appear at high pressures represent the arc instability as a result of relatively high background peaks of current. Thus, the Fourier transformation shows very low frequencies in the voltage waveforms at higher pressures. In other words, abrupt and less frequent pulses on voltage waveforms make it appear to be a DC plateau that is fluctuating with very small frequencies.

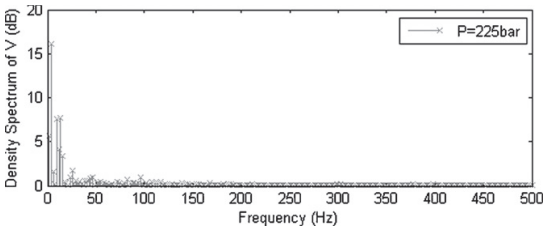

Fig. 8. Sample PSD of voltage waveform at 225 bar.

Although the voltage and current waves show harmonic behavior in the time domain at all pressures, it was observed that the lower frequency wave components prevail at higher pressures. Slania (1997) confirmed that there should be a strong relationship between the current and voltage waveforms in both time and frequency domains that were observed to be repelled at higher pressures. At lower pressures, the voltage and current waveforms show the same behavior in the frequency domain while at high pressures, voltage waveforms deviate from characteristic frequencies that are produced in the current waveforms. The net power, which is the product of the process voltage and current, appears

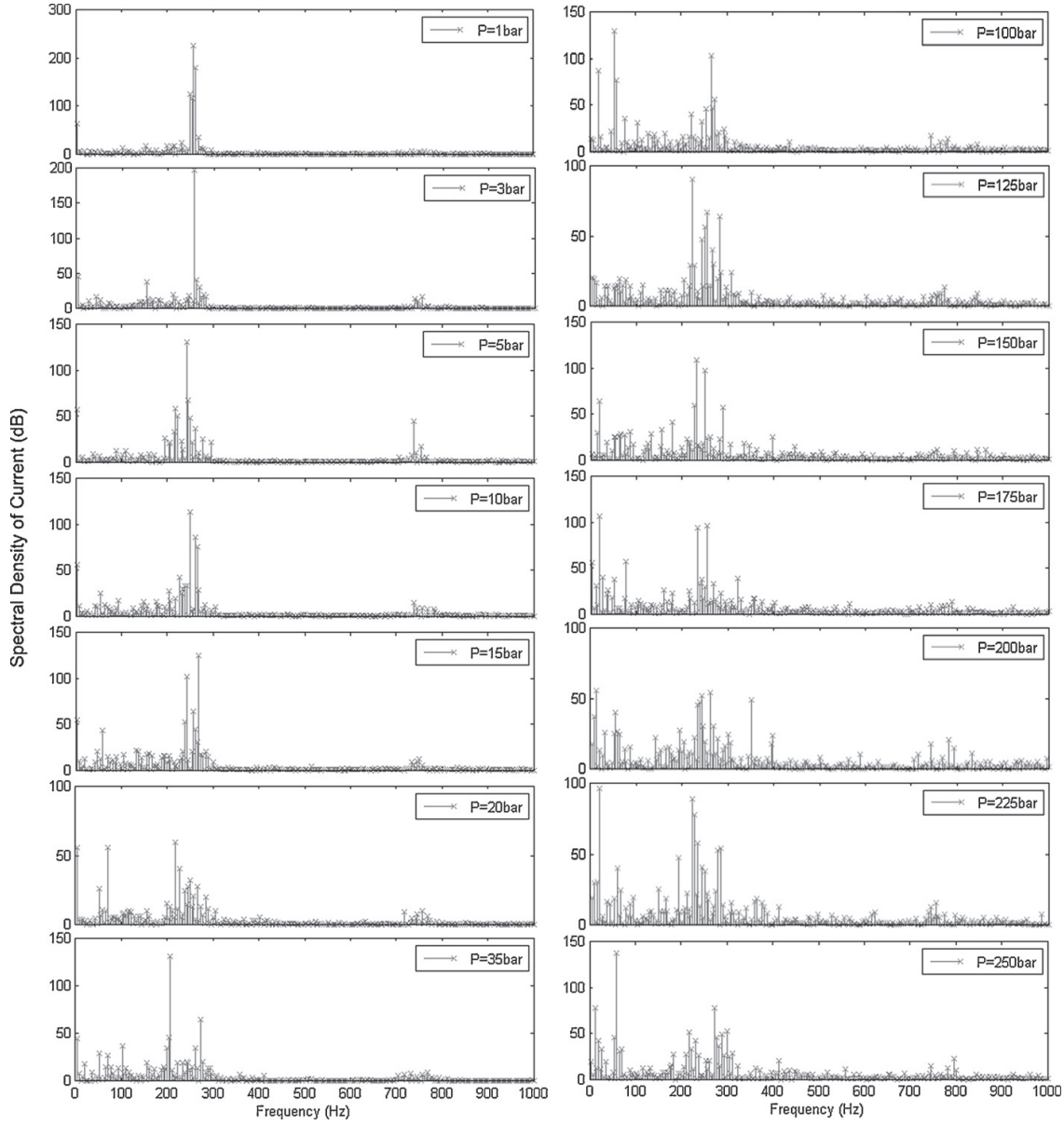

Fig. 9. Power spectral density of current waveforms at different pressures.

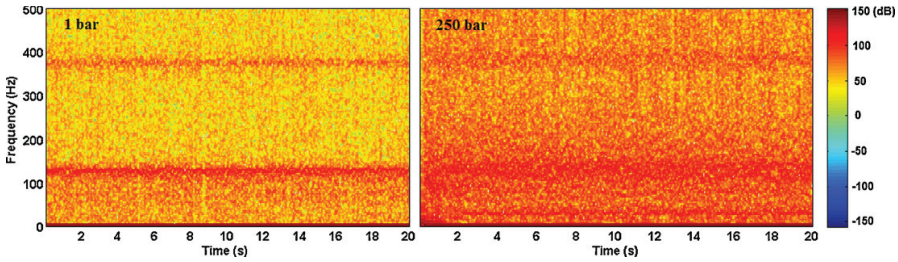

Fig. 10. Spectrograms of current at 1 and 250 bar.

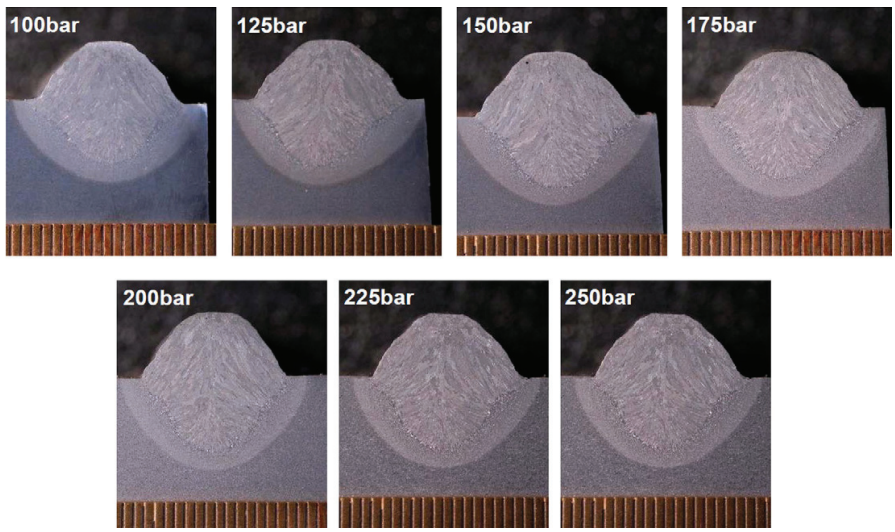

Fig. 11. Weld bead cross sections at pressures 100 to 250 bar.

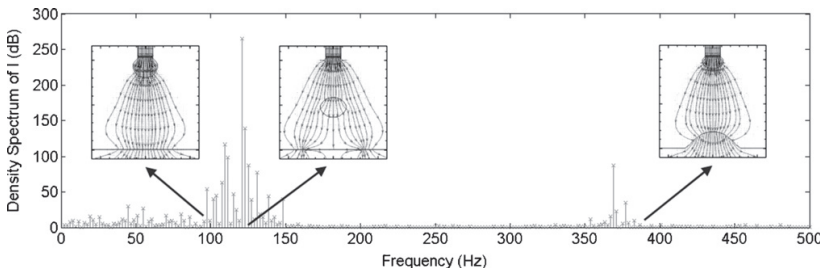

Fig. 12. Mass transfer monitoring by density spectrum of current [Simulation data from Hu and Tsai (2007)].

constant as the voltage and current power spectra become uncorrelated. It may explain the near-constant weld bead shape at higher pressure (Fig. 11) despite fundamental changes in the frequency domain.

Nixon et al. (2000) and Richardson et al. (2002) showed that there is no correlation between electrical stability and process stability. This approach indicates that the process stability may not be judged solely in the time domain.

7. Conclusions

A Fourier transformation was applied to the electrical data of pulsed hyperbaric GMAW to monitor how the mass transfer changes as the ambient pressure increases. The following conclusions can be drawn.

- The general trend of mass transfer follows the pulsed data of the current, which was set prior to welding. Moreover, the frequencies remain constant during the weld.
- Two frequencies were found to be influential. One is around 125 Hz, where the pulsing frequency is set, and the other is 375 Hz, which depends on the mains and converters. The latter is of less importance because its amplitude is less than 30% of the dominant frequencies.
- Lower frequencies were observed in current and voltage waveforms in the higher pressure range due to the very high pulse amplitudes and the very short pulse durations.
- Current correlograms show that the base currents are generated more randomly than the peak currents at all the pressures. They fall inside the 95% confidence band within a smaller time interval than the corresponding peak currents.
- Calculated arc power shows that at higher pressures, more energy is required to maintain the arc that is not transferred to the weld pool.

Acknowledgement

The financial support from the Norwegian Research Council (Contract No. 192967/S60), Statoil, Gassco, Technip and EFD Induction is gratefully acknowledged.

References

Alfaro, S.C.A., Carvalho, G.C., Da Cunha, F.R., 2006. A statistical approach for monitoring stochastic welding processes. J. Mater. Process Tech. 175, 4–14.
Box, G.E.P., Jenkins, G.M., Reinsel, G.C., 2008. Time Series Analysis, fourth ed. John Wiley & Sons. Inc., New Jersey.
Brockwell, P.J., Davis, R.A., 2002. Introduction to Time Series and Forcasting, second ed. Springer.
Dilthey, U., Reichell, T., Scheller, W., 1996. Statistical Process Parameter Surveillance in GMA Welding. Int. J. Join. Mater. 8, 120–126.
Diongue, A.K., Diop, A., Ndongo, M., 2008. Seasonal fractional ARIMA with stable innovations. Stat. Probab. Lett. 78, 1404–1411.
Engelberg, S., 2007. Random Signals and Noise. CRC Press.
Fostervoll, H., Woodward, N.J., Akselsen, O.M., 2009. The effects on process performance of reducing the pressure from 36 to 1 bar in hyperbaric MIG welding. In: Proceedings of the ASME 28th International Conference on Ocean, Offshore and Artic Engineering, OMAE'09, Honolulu, Hawaii.
Hu, J., Tsai, H.L., 2007. Heat and mass transfer in gas metal arc welding. Part I: The arc. Int. J. Heat Mass Transfer 50, 833–846.
Johnson, J.A., Carlson, N.M., Smartt, H.B., Clark, D.E., 1991. Process-control of GMAW – Sensing of metal transfer mode. Weld J. 70, S91–S99.
Jones, G.R., 1988. High Pressure Arcs in Industrial Devices. Cambridge University Press.
Joseph, A., Harwig, D., Farson, D.F., Richardson, R., 2003. Measurement and calculation of arc power and heat transfer efficiency in pulsed gas metal arc welding. Sci. Technol. Weld Joi. 8, 400–406.
Luksa, K., 2006. Influence of weld imperfection on short circuit GMA welding arc stability. J. Mater. Process. Tech. 175, 285–290.
Mazzaferro, J.A.E., Machado, I.G., 2009. Study of arc stability in underwater shielded metal arc welding at shallow depths. P. I. Mech. Eng. C – J. Mec. 223, 699–709.
McLarty, J.W., Bahna, S.L., 2009. Sampling and statistical inference. Ann. Allerg. Asthma Im. 103, S22–S25.
Newland, D.E., 2005. An Introduction to Random Vibrations, Spectral & Wavelet Analysis. Dover Publications, New York.
Nixon, J.H., 1995. Underwater Repair Technology. Gulf Professional Publishing.
Nixon, J.H., Hart, P.R., Richardson, I.M., 2000. Diverless underwater welding: theory and operation. In: Proc. Int. Conf. ICAWT'00, Orlando, FL.
Norton, M.P., Karczub, D.G., 2003. Fundamentals of Noise and Vibration Analysis for Engineers, second ed. Cambridge.
Oliveira, C.R., Werlang, T., 2007. Ergodic hypothesis in classical statistical mechanics. Rev. Bras. Ensino. Fis. 29, 189–201.
Porat, B., 1994. Digital Processing of Random Signals: Theory & Methods. Prentice Hall.
Richardson, I.M., Nixon, J.H., Nosal, P., Hart, P., Billingham, J., 2000. Hyperbaric GMA welding to 2500 m water depth. In: Joint International Conference ETC/OMAE OMAE 2000–2160, New Orleans, USA.
Richardson, I.M., Woodward, N.J., Billingham, J., 2002. Deepwater welding for installation and repair – A viable technology? In: 12th International Offshore and Polar Engineering Conference.
Slania, J., 1997. Use of Fourier transforms in analysis of pulsed MAG welding. Weld. Int. 11, 761–764.
Strube, H.W., 1985. A generalization of correlation-functions and the Wiener–Khinchin theorem. Signal Process 8, 63–74.
Subramaniam, S., White, D.R., Jones, J.E., Lyons, D.W., 1998. Analysis of arc voltage, current, and light signals in pulsed gas metal arc welding of aluminium. Sci. Technol. Weld. Joi. 3, 304–311.
Tabachnick, B.G., Fidell, L.S., 2007. Using Multivariate Statistics, fifth ed. Pearson International Edition.
Waller, D.N., Foster, C.J., Wagner, R., 1990. Real-time imaging for arc-welding. Int. J. Comp. Integ. M. 3, 249–260.
Witt, T.J., 2007. Using the autocorrelation function to characterize time series of voltage measurements. Metrologia 44, 201–209.
Zhu, Y.S., 2006. On statistical significance of signal. High Energ. Phys. Nuc. 30, 331–334.

Paper II

Analytical Modeling of Weld Bead Shape in Dry Hyperbaric GMAW Using Ar-He Chamber Gas Mixtures.

Amin S. Azar, Sigmund K. Ås, Odd M. Akselsen.

Journal of Materials Engineering and Performance, Accepted.

JMEPEG
DOI: 10.1007/s11665-012-0331-z

1059-9495/$19.00

Analytical Modeling of Weld Bead Shape in Dry Hyperbaric GMAW Using Ar-He Chamber Gas Mixtures

Amin S. Azar, Sigmund K. Ås, and Odd M. Akselsen

(Submitted March 12, 2012; in revised form July 12, 2012)

Hyperbaric arc welding is a special application of joining the pipeline steels under seawater. In order to analyze the behavior of the arc under ambient pressure, a model is required to estimate the arc efficiency. A distributed point heat source model was employed. The simulated isotherms were calibrated iteratively to fit the actual bead cross section. Basic gas mixture rules and models were used to calculate the thermal properties of the low-temperature shielding gas under the ambient pressure of 10 bar. Nine bead-on-plate welds were deposited each of which under different Ar-He chamber gas compositions. The well-known correlation between arc efficiency (delivered heat) and the thermal conductivity was established for different gas mixtures. The arc efficiency was considered separately for the transverse and perpendicular heat sources. It was found that assigning single heat efficiency factor for the entire arc, which is usually below unity, causes a noticeable underestimation for the heat transfer in the perpendicular direction and a little overestimation in the transverse direction.

Keywords distributed heat source model, dry hyperbaric welding, GMAW, weld bead geometry

1. Introduction

The temperature distribution around the weld bead is responsible for the final microstructure, residual stresses, and mechanical properties of the weld joints (Ref 1). Rykalin (Ref 2) and Rosenthal (Ref 3) have implemented the Fourier's law to describe the temperature variations when welding with a moving heat source. They assumed a dimensionless point heat source, which dissipates enormous amount of heat instantly. The latter sentence implies that such approaches cannot be applied for the heat sources with unequal transversal and longitudinal dimensions or for the processes with uneven heat distribution along different directions. Therefore, many researchers proposed a number of alternative approaches (Ref 4-11), each of which addressing specific boundary conditions.

In dry hyperbaric gas metal arc welding (GMAW), the arc column undergoes dimensional constriction as pressure increases (Ref 12-17). Higher ambient pressure reduces the arc root size resulting in smaller weld pool and various thermal gradients. The magnitude of such phenomena is also a function of chamber gas physical properties. Consequently, affected microstructure of the weld may alter the service life and other properties of the welds (Ref 18-24).

The global demand for remote subsea operations surges ahead because of ambitious oil and gas exploration at increased water depths. The high depth welding operations require fully stable process in terms of spatter generation and metal transfer consistency (Ref 25). As a result, the chamber gas should also be optimized for spattering, weld bead geometry, high productivity, and acceptable mechanical properties.

The effect of shielding gas on the weld characteristics, mode of metal transfer, weld bead profile, weld penetration, and weld pool dynamics is well established for conventional GMAW (Ref 26-31). Among the types of shielding gases, the most applied gases are argon and helium (Ref 32, 33) each of which possessing individual physical properties, i.e., thermal conductivity, density, and specific heat. However, these properties vary as pressure and temperature alter. The effects of ambient pressure on weld properties using pure Ar gas have been presented elsewhere (Ref 17).

The inherent characteristics of He, e.g., the ionization potential, result in noticeable formation of iron vapor which enhances the thermo-physical characteristics of the arc (Ref 34-38). It was found that the electrical conductivity of the arc is improved when iron vapor is present, which entails better arc stability. Other investigations show that iron vapor also increases the thermal conductivity of the arc column that can reduce the depth of penetration and increase the bead width accordingly. Rao et al. (Ref 32, 33) have performed a comprehensive simulation on Ar-He mixtures. They have excluded the effect of iron vapor for sake of simplicity. Zähr et al. (Ref 39) explicitly considered the temperature-dependent characteristics of Ar-He shielding gas mixtures in their simulations. Despite comprehensive investigations, the effect of environmental hyperbaric pressure as an additional process parameter on the behavior of the arc and iron vapor generation has not been determined by far.

A model is required to assess the weld bead profile variations based on the characteristics of employed shielding

Amin S. Azar, Department of Engineering Design and Materials, Norwegian University of Science and Technology (NTNU), Richard Birkelands Vei 2B, 7034 Trondheim, Norway; **Sigmund K. Ås**, SINTEF Materials and Chemistry, Trondheim, Norway; and **Odd M. Akselsen**, Department of Engineering Design and Materials, Norwegian University of Science and Technology (NTNU), Richard Birkelands Vei 2B, 7034 Trondheim, Norway; and SINTEF Materials and Chemistry, Trondheim, Norway. Contact e-mail: amin.azar@ntnu.no.

Published online: 03 August 2012

gases. In this study, the distributed point heat source model after Myhr and Grong (Ref 40, 41) will be developed to approximate the weld isotherms. The shape-dependent parameters of the model will be calibrated in accordance with the experimental data and will be reported for each mixture.

2. The Method

The welding experiments were carried out with different chamber gas mixtures starting from pure Ar ending in pure He. In order to identify the effect of the shielding gas, other welding parameters were kept constant. Bead-on-plate deposition in flat position was performed at 10 bar of ambient pressure. The base metal was API-X70 pipeline steel and the filler wire was HBQ Coreweld (φ = 1.0 mm) supplied by ESAB. The wire feeding rate was 135.0 mm/s and the welding speed was set to 7 mm/s. The torch standoff was 10 mm perpendicular to test plate. The control unit (Isotek Equipment ID: WPC1PA10) of the power suppliers (Fronius TPS450 × 3, 200 V OCV) is an adaptive welding system and the welding current and voltage were recorded continuously during the process. The average arc voltage and current values for each case is presented in Fig. 1.

The gases were mixed using two flow meters and a pressure sensor valve. Prior to pressurization with the target mixture, the chamber atmosphere was evacuated to 1 mbar and flushed twice by pure Ar gas at 10 bar to ensure the absence of the superfluous environmental gases. Following the last stage, the desired mixture of gas was filled into the chamber up to 10 bar which is the target pressure for all specimens. After welding, the specimens were sectioned, the bead profiles were etched by Nital 2%, and images were recorded at a constant magnification using a light microscope. In the next stage, the acquired images were imported to a Matlab code by which the welding parameters in the model were calibrated. The arc efficiency factor (η) was split into two coefficients; η_Y for transverse and η_Z for perpendicular heat sources.

3. The Model

In this model, the welding heat source is assumed as conformed discrete point sources in two dimensions (2D model). The array of these points forms distributions in both transverse and perpendicular directions as shown in Fig. 2(a). The plate thickness of d is taken into account similar to the medium thick plate solution proposed by Rosenthal (Ref 3). The shielding environment was stationary and no separately flowing gas was used in the experiments that can potentially reduce the convectional heat loss. On the one hand, the heat conductivity of the chamber gas is much less than that of steel plate. On the other hand, according to aforementioned models by Rosenthal and Rykalin, if a number of heat sources run in parallel, the heat flow between them converges to zero (i.e., adiabatic condition). Therefore, the only dominant heat-conducting media is the base metal, and it can be assumed that the surfaces of the plate are impermeable to heat. This assumption will be imposed on all samples and the probable effects of ignoring convectional heat loss will almost influence all quantification results at the same extent. When the distributed point heat sources emit transient heat, it flows through the plate thickness and raises the temperature. Since the surfaces are adiabatic, the excessive amount of heat should be reflected at the surfaces (no heat loss condition). The reflections are not considered if infinite plate condition is assumed. The aforementioned reflection pattern can be introduced using the method of imaginary heat sources (Ref 41). In this approach, a number of fictitious sources are placed above and below each point source, simulating the reflection from the surfaces. Perret et al. (Ref 42) and Azar et al. (Ref 43) have compared the analytical and numerical results and pointed out that there is a consistent agreement between two simulations.

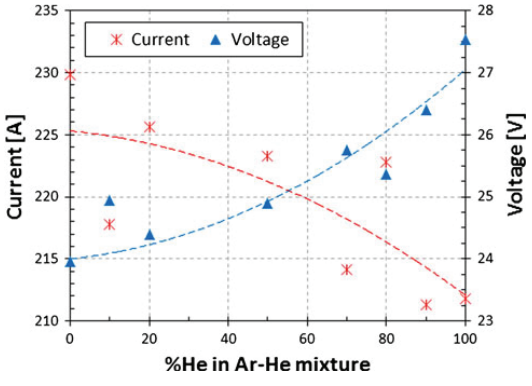

Fig. 1 The variation of current and voltage for different (Ar-He) mixtures

Figure 2(b) and (c) depict the relative positioning of the imaginary heat sources and distributed point sources. As shown in Fig. 2, the transverse and perpendicular arrays of the point sources (● shapes in Fig. 2) are set apart from each other with constant distances of ε and δ, respectively. The number of point sources is arbitrary, though, 8 to 10 sources were recommended by Grong (Ref 41) for obtaining good results. The sum of their heat emission should satisfy the following equation:

$$q_0 = \sum_i \left(q_t^i + q_p^i\right) = \eta UI \qquad \text{(Eq 1)}$$

where q_0 is the total heat flux, q_t and q_p are the heat flux from each transversely and perpendicularly arrayed point source respectively, η is arc efficiency factor, U is the average arc voltage, I is the average arc current and i is the respective heat source number. The number of imaginary heat sources (⊗ shapes in Fig. 2) can be selected as many as possible for precision, yet, it was found to have imperceptible effect if exceeded more than five points, since the value is affecting a parameter inside converging series as presented in Eq 4.

The contribution of all transversely arrayed heat source and respective images are as follows:

$$T(q_t) = \frac{q_t}{2\pi\lambda}\exp\left(-\frac{vx}{2a}\right) \times \left[\sum_{i=-\infty}^{+\infty}\frac{1}{R_i}\exp\left(-\frac{v}{2a}R_i\right)\right] \qquad \text{(Eq 2)}$$

where λ is the heat conductivity, v is the welding speed, x is the lateral distance from the y-z plane, a is the thermal diffusivity, and R_i is the distance vector from the observation point P (where the temperature rise is sought) to any transversely

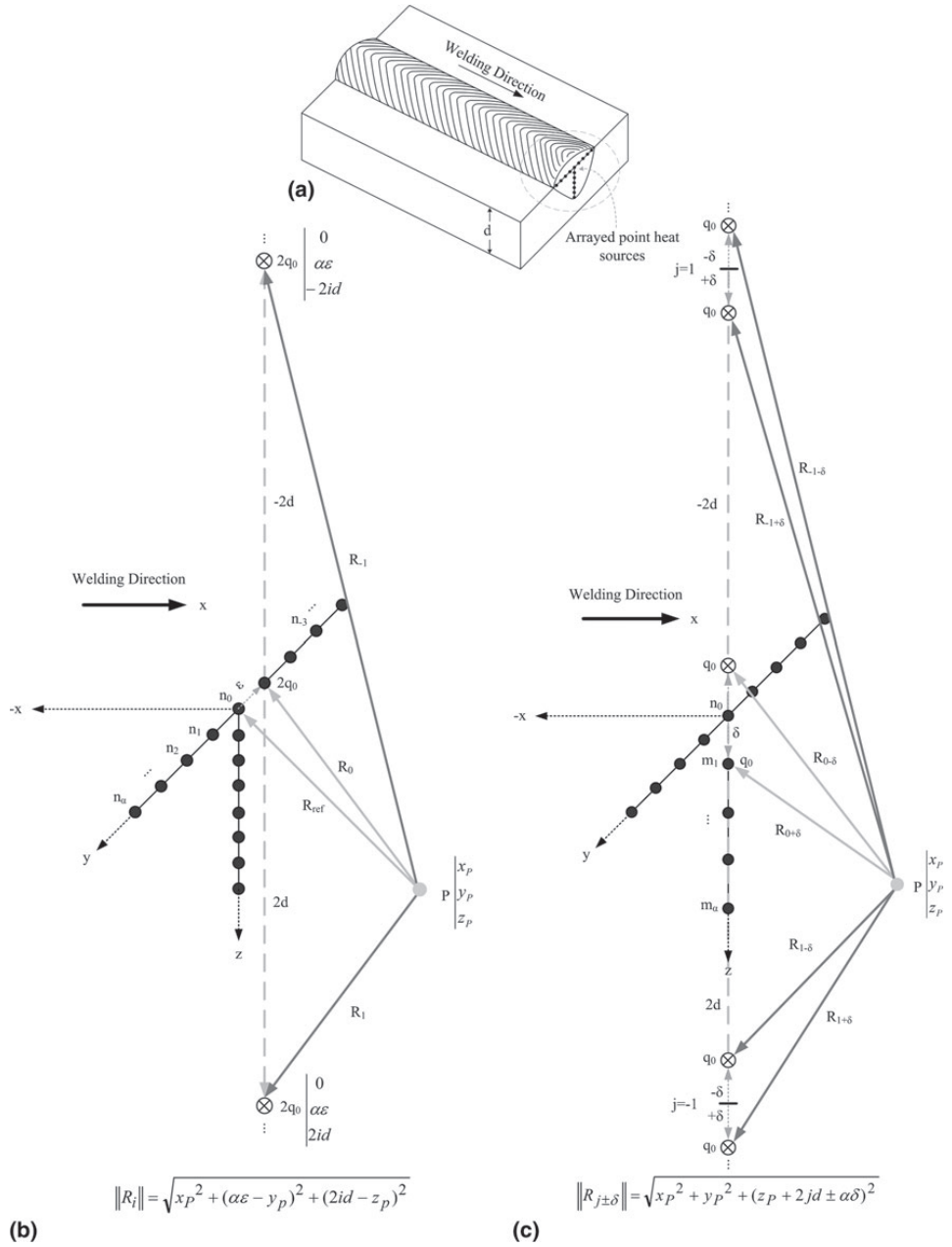

Fig. 2 (a) Arrayed point heat sources on the weld cross-section, (b) method of images for calculating the temperature field around the point heat sources displaced along the *y*-axis. n_i is the respective symbol for each point and R_{ref} is the reference vector from point of observation P to n_0, (c) method of images for calculating the temperature field around the point heat sources displaced along the *z*-axis. m_j is the respective symbol for each sub-surface point

arrayed point heat source. The size of R_i vector can be defined as below:

$$\|R_i\| = \sqrt{x_P^2 + (\alpha\varepsilon - y_P)^2 + (2id - z_P)^2} \quad \text{(Eq 3)}$$

where (x_P, y_P, z_P) is the Cartesian coordination of the observation point P, ε is the lateral distance between transversely arrayed point sources, and d is the plate thickness.

The contribution of all perpendicularly arrayed heat source and respective images are

$$T(q_p) = \frac{q_p}{2\pi\lambda}\exp\left(-\frac{vx}{2a}\right) \times \left[\sum_{j=-\infty}^{+\infty}\frac{1}{R_{j\pm\delta}}\exp\left(-\frac{v}{2a}R_{j\pm\delta}\right)\right] \quad \text{(Eq 4)}$$

where $R_{j\pm\delta}$ is the distance vector from the observation point P to any perpendicularly arrayed point heat source. The size of $R_{j\pm\delta}$ is

$$\left\|R_{j\pm\delta}\right\| = \sqrt{x_P^2 + y_P^2 + (z_P + 2jd \pm \alpha\delta)^2} \quad \text{(Eq 5)}$$

where δ is the lateral distance between any perpendicularly arrayed point source and the surface.

The temperature rise at point P is the sum of all arrayed and imaginary heat sources:

$$T_t - T_0 = \sum_i \left[\eta_Y \cdot T(q_t)_i + \eta_Z \cdot T(q_p)_i\right] \quad \text{(Eq 6)}$$

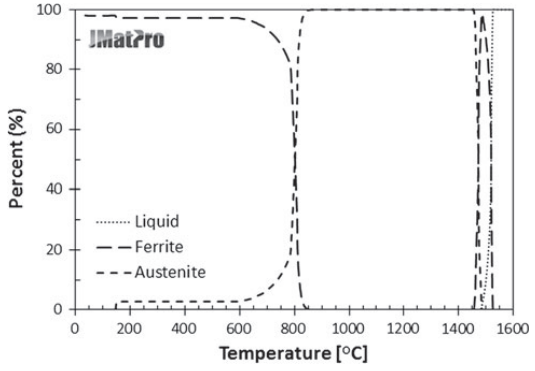

Fig. 3 Phase diagram of API-X70 when cooling at the rate of 100 °C/s

Table 1 Calculated temperature-dependent variables for three different ranges

Temperature range, °C	Phase	a, m²/s	λ, W/m·K
T_0-600	α	4.68×10^{-6}	25
600-825	α + γ	6.16×10^{-6}	30
825-1470	γ	4.51×10^{-6}	35

where T_0 is the preheating temperature and η_Y and η_Z are the arc efficiency factors for transverse and perpendicular heat sources respectively. The isotherms of interest can be plotted using Eq 6. The welding parameters were described in "The Method" section. Two separated arc efficiency factors can be later employed in finite element analyses where at least two heat sources are required for modeling the eventual weld bead shape. This approach was described by Azar et al. elsewhere (Ref 43).

The materials parameters like λ and a can be either measured or simulated. In this study, JMatPro software was utilized to compute the temperature-dependent physical properties as well as the required phase diagrams. Based on the investigation performed by Azar (Ref 44), it was found that the fusion temperature of the diluted weld metal was very close to the 50% base materials and 50% welding wire combination. Three characteristic temperatures were chosen based on the predicted phase diagram for cooling rate of about 100 °C/s, each of which determining the borders between fusion zone, HAZ and partially transformed zone. Figure 3 illustrates the predicted phase diagram. The cooling rate was chosen based on the earlier temperature measurements under hyperbaric condition (Ref 45).

The chosen λ and a parameters between the isotherms are the average of calculated values between the outer values. Table 1 shows the employed parameters for each range. The chemical composition of the base metal, welding wire, and weld metal after welding is tabulated in Table 2.

4. Results and Discussion

Distributed point heat source model was adapted based on its ability of being calibrated with respect to the actual bead shape. The model in its original form can hardly be calibrated with the real weld bead if some physical constants are not fine-tuned. Introducing the spatial distance between the points leads to a better control on the spread of the heat source in Y and Z directions disregarding the constant physical properties.

Figure 4 shows the calibrated isotherms for 100% Ar, 50% He-Ar, and 100% He chamber gases. Since the weld bead may not be symmetrical with respect to the centerline, the calibration procedure was performed for both halves separately, and the resultant values were averaged.

In order to calibrate the isotherms, the welding parameters were set to constants, identical to what were used or obtained during the experiments. The heat efficiency factors, however, were found by trial and error for both transverse and perpendicular directions separately to improve the degree of fit between the simulated isotherms and actual microstructural marks.

Table 2 Chemical composition of the base material, welding wire, and weld metal after welding

	Chemical composition, wt.%											
	C	Si	Mn	P	Ni	Cr	Mo	Cu	V	Ti	N_2	O_2
Max	0.08	0.28	1.85	0.015	0.31	0.1	0.06	0.3	0.01	0.02	80 ppm	…
Min	0.04	0.05	1.5	0.008	0.11	0.05	0.04	0.1	…	0.006	…	…
HBX13	0.04	0.5	1.3	…	0.5	…	…	…	…	0.02	…	600 ppm
Weld metal	0.074	0.38	1.4	0.012	0.51	0.033	…	…	…	…	80 ppm	360 ppm

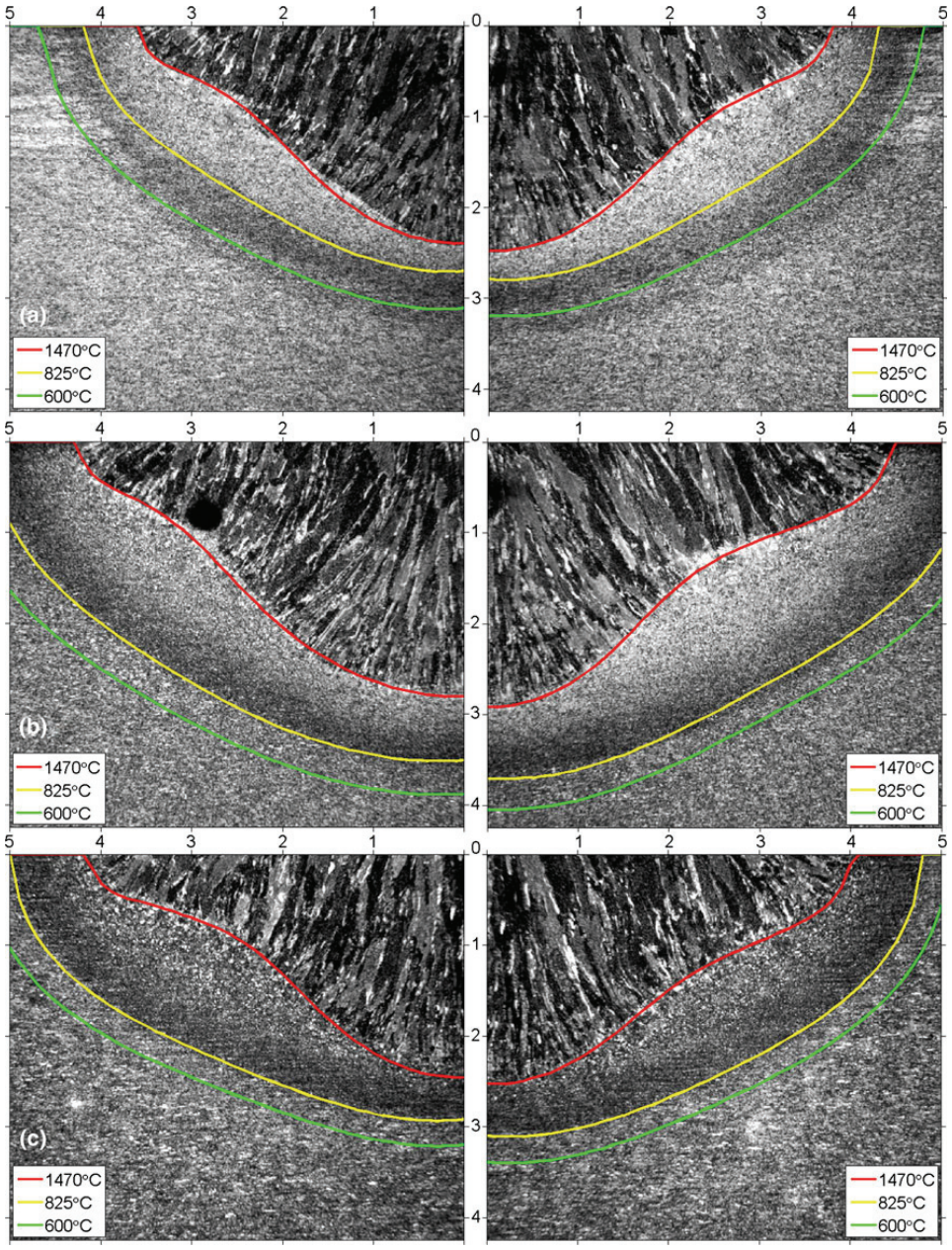

Fig. 4 Calibrated isotherms for (a) 100% Ar, (b) 50%He-Ar, and (c) 100% He shielding gases

Figure 5 depicts the arc power and depth-to-width (D/W) ratio of the sub-surface weld bead for different gas mixtures. For calculating the standard deviation of the delivered power, instantaneous current values are multiplied to instantaneous voltage values and averaged over the entire time domain (Ref 46). It is worth noting that the high standard deviation values in the graph are not representing instability since the distribution of the data points is intensely concentrated around the average point, and only some deviating data are building up the presented high values.

According to Fig. 5, the arc power increases systematically as He level increases. Nevertheless, the D/W ratio decreases steadily to about 70% He-Ar and increases dramatically as it approaches to pure He. Such contradiction suggests the

presence of other factors (e.g., gas thermal properties) in determination of the weld bead shape.

In dry hyperbaric welding, especially at high pressures, the arc plasma column is very small due to the arc root constriction phenomenon (Ref 47). As a result, the surrounding lower temperature gas that was not involved in the ionization process is responsible for conducting the heat away from the arc region (Ref 48).

According to Wassiljewa equation (Ref 49, 50), the thermal conductivity of binary gases at low pressure can be calculated using the following equation:

$$\lambda_{\text{mix}} = \frac{\lambda_1 x_1}{x_1 + A_{12} x_2} + \frac{\lambda_2 x_2}{x_2 + A_{21} x_1} \quad \text{(Eq 7)}$$

where x_1 and x_2 are the molar fraction of each gas in a binary mixture and A_{ij} is a combinational factor expressed by Mason and Saxena (Ref 51). Stiel and Thodos modification (Ref 52) was applied to correct for high-pressure effect; yet, the low-pressure range was calculated using Eq 7. Calculations show that the thermal conductivity at 10 bar has a linear relationship with temperature for all the mixtures. However, the slope is steeper for He-dominant mixtures which implies that the thermal conductivity increases rapidly with minor increments of temperature. Increasing the pressure shows a different behavior in Ar-dominant and He-dominant mixtures. Moreover, the average level of thermal conductivity for Ar is very low. Pure He on the other hand, possesses higher thermal conductivity level compared to Ar.

Figure 6 shows the variation of thermal conductivity at different temperature and pressure levels (confined to low-temperature range for peripheral gas). It can be inferred that at a given pressure, the thermal conductivity of pure He is very much dependent on the temperature compared to that of Ar. In other words, the variation of either pressure or temperature has the same magnitude of effect in pure Ar while pure He is affected more by temperature rather than pressure. The behavior of Ar-He mixtures fall between the latter cases.

According to researches by Kannappan and Bose on pure Ar (Ref 53) and pure He (Ref 54), the thermal conductivity of both gases increase as temperature rises to about 13,000 °C and decreases for the higher temperature range up to about 24,000 °C which is almost the maximum plasma jet temperature (Ref 55). A comprehensive model that can predict the thermal conductivity of Ar-He mixtures as a function of pressure and temperature is not available by far. However, referring to the data given in Kannappan and Bose (Ref 53, 54) on pure Ar and He, it can be inferred that the consistency of the arc characteristics from arc core to periphery is determined by temperature gradient instead of pressure difference which does not exceed more than several mbar (Ref 56). At high ambient pressure, such behavior is very favorable from the arc stability point of view since the consistency in power delivery across the arc is less pressure dependent. Nevertheless, the investigation of gas thermal conductivity in this study is following the nonionic gas rules due to the absence of a model that can predict the properties of ionic state at high-pressure ranges. According to Poling et al. (Ref 52), the properties of ionic and nonionic gases can be calculated using the existing methods, but the crossover of these two regions can show sharp property changes.

Figure 7(a) shows how the weld bead dimensions vary as the calculated thermal conductivity increases in a number of Ar-He mixtures at 10 bar. It shows that the transverse dimension (y) of the weld bead, which increases according to the illustrated power relationship, is more influenced by the heat conductivity of the peripheral low-temperature gas.

As presented earlier in Eq 6, the arc efficiencies were separated for transverse and perpendicular heat sources. Figure 7(b) presents how the simulated arc efficiency factors are varying with the calculated thermal conductivity value. Both η_Y and η_Z show increasing trend as He level increases (higher λ value).

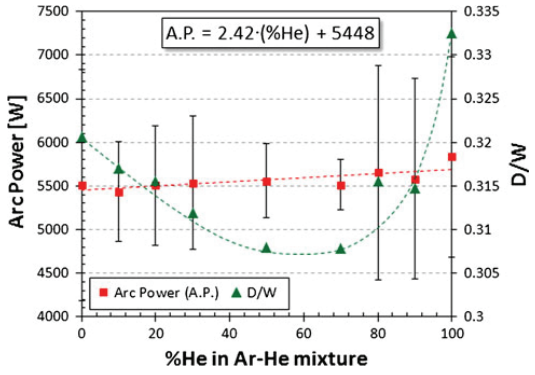

Fig. 5 Arc power and depth-to-width variations for different mixtures

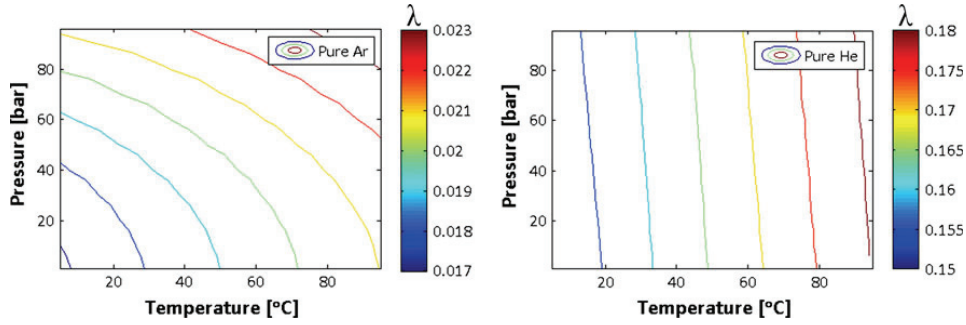

Fig. 6 Effect of pressure and temperature on the thermal conductivity of the arc surrounding gas. (a) Pure argon and (b) pure helium

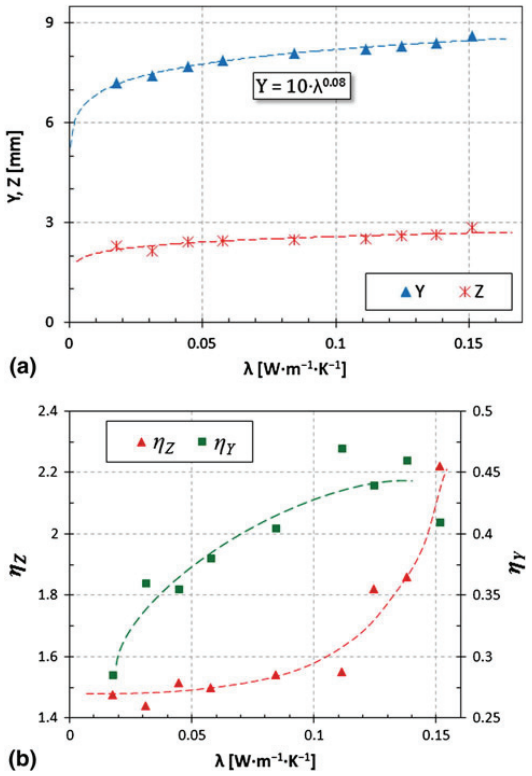

Fig. 7 (a) Variation of weld bead dimensions against the calculated thermal conductivity at low-temperature region. (b) Transverse and perpendicular arc efficiency factors varying with calculated thermal conductivity of the mixture

The perpendicular heat efficiency factor (η_Z) shows minor increments for the λ values below 0.11 (W/m·K) that corresponds to the 70% He-Ar mixture. Above this value, η_Z increases exponentially. On the other hand, η_Y increases monotonically with λ and reaches a plateau at He-dominant concentration. Comparing the data with depth-to-width variation in Fig. 5 reveals the effect of gas thermal conductivity on the weld bead geometry. High He concentration brings about a very high perpendicular thermal conductivity which in turn increases the width and throat dimension of the weld bead.

Figure 7(b) suggests that defining a unique arc efficiency factor for the entire process can potentially underestimate the arc core power and overestimate the energy transmission in the peripheral region. Values presented for the arc efficiencies can be good arguments for the arc constriction phenomenon since the power delivery coefficient in the core (η_Z) even at 10 bar is much higher than periphery.

Azar et al. (Ref 43) showed that the heat source parameters, which are widely used in finite element simulations, can be discovered from the actual weld bead. The estimated heat efficiency factors separated for transverse and perpendicular heat sources can be used in defining a justified heat source for those simulations.

5. Conclusions

- The distributed heat source model can be used to estimate the arc efficiency factor for transverse and perpendicular heat sources. This is essentially beneficial for finite element modeling where a superposition of at least two heat sources is used.
- A correlation was observed between the weld bead shape and low-temperature thermal conductivity of the surrounding gas.
- Arc constriction at 10 bar is less pronounced for He-rich mixtures since both *Y* and *Z* dimensions are larger than that of Ar for the same power source settings.
- Since the hyperbaric welding should be performed at even higher ambient pressures, employing gases that may result in better arc characteristics is desired. For instance, using pure He gas or a high He concentration mixture is potentially beneficial, depending on the required mechanical properties.

Acknowledgments

The financial support from the Norwegian Research Council (Contract No. 192967/S60), Statoil, Gassco, Technip, and EFD Induction is gratefully acknowledged. Special thanks to Dr. Sepehr Hatami at Chalmers University of Technology for his guidance on JMatPro software.

References

1. K.A. Lyttle, *ASM Handbook*, D.L. Olson, T.A. Siewert, S. Liu, and G.R. Edwards, Ed., American Society for Metals, Metal Park, OH, 1993, p 64–69
2. N.N. Rykalin, *Berechung der Wärmevorgänge beim Schweissen*, VEB Verlag Teknik, Berlin, 1953
3. D. Rosenthal, The Theory of Moving Sources of Heat and its Application on Metal Treatments, *Trans. ASME*, 1946, **68**, p 849–866
4. V.A. Zrazhevskii and G.I. Ignatchenko, Evaluating the Coefficient of Concentration for a Normally Distributed Source of Heat for Welding, *Autom. Weld. Ussr*, 1981, **34**(11), p 15–20
5. D.Y. Tzou and J. Li, Local Heating Induced by a Nonhomogeneously Distributed Heat-Source, *Int. J. Heat Mass Transf.*, 1993, **36**(14), p 3487–3496
6. N.R. Roshyara, Correct Modeling for Gaussian Distributed Heat Source on a Finite Thin Rod, *Heat Mass Transf.*, 2009, **45**(10), p 1253–1260
7. F.F. Ling and V.C. Mow, Surface Displacement of a Convective Elastic Half-Space under an Arbitrarily Distributed Fast-Moving Heat Source, *J. Basic Eng.*, 1965, **87**(3), p 729–734
8. C. Doumanidis and N. Fourligkas, Distributed-Parameter Control of the Heat Source Trajectory in Thermal Materials Processing, *J. Manuf. Sci. Eng. Trans. ASME*, 1996, **118**(4), p 571–578
9. P.V. Denisov and G.A. Mirlin, Calculation of Temperature to Which Thin Sheet-Metal Is Heated by a Normally Distributed Heat Source in Pulsed-Arc Spot Welding, *Weld. Prod.*, 1974, **21**(1), p 5–10
10. G.F. Alekseev, Formation of Maximum Permissible Gradient of the Temperature-Field in Local Heat-Treatment of Welded-Joints in Vessels with a Uniformly Distributed Heat-Source, *Weld. Prod.*, 1984, **31**(2), p 10–11
11. A.J. Goldak, A. Chakravarti, and M. Bibby, A New Finite-Element Model for Welding Heat-Sources, *Metall. Trans. B Process Metall.*, 1984, **15**(2), p 299–305
12. H. Ozden, Underwater Welding in Hyperbaric Conditions, *Sea Technol.*, 2008, **49**(6), p 52–54

13. A.E. Khairetdinov, A.G. Mazel, and S.V. Golovin, Technological Characteristics of the Welding Arc in a Hyperbaric Chamber, *Weld. Prod.*, 1981, **28**(6), p 11–13
14. O.M. Akselsen, R. Aune, H. Fostervoll, and A.S. Harsvoer, Dry Hyperbaric Welding of Subsea Pipelines, *Weld. J.*, 2006, **85**(6), p 52–55
15. J.A.E. Mazzaferro and I.G. Machado, Study of Arc Stability in Underwater Shielded Metal Arc Welding at shallow depths, *Proc. Inst. Mech. Eng. C J. Mech. Eng. Sci.*, 2009, **223**(3), p 699–709
16. P.R. Hart, J.H. Nixon, and I.M. Richardson, Diverless Underwater Welding: Theory and Operation, *Proceeding, International Conference ICAWT 2000*, Orlando, FL, 2000
17. N. Woodward, H. Fostervoll, and O.M. Akselsen, The Effects on Process Performance of Reducing The Pressure from 36 to 1 bar in Hyperbaric MIG Welding, *Proceedings of the ASME 28th International Conference on Ocean, Offshore and Artic Engineering, OMAE 2009*, Honolulu, Hawaii, 2009
18. E. Keehan, J. Zachrisson, and L. Karlsson, Influence of Cooling Rate on Microstructure and Properties of High Strength Steel Weld Metal, *Sci. Technol. Weld. Join.*, 2010, **15**(3), p 233–238
19. Y.W. Shi and Z.X. Han, Effect of Weld Thermal Cycle on Microstructure and Fracture Toughness of Simulated Heat-Affected Zone for a 800 MPa Grade High Strength Low Alloy Steel, *J. Mater. Process. Technol.*, 2008, **207**(1–3), p 30–39
20. K. Sivaprasad and S.G.S. Raman, Influence of Weld Cooling Rate on Microstructure and Mechanical Properties of Alloy 718 Weldments, *Metall. Mater. Trans. A*, 2008, **39A**(9), p 2115–2127
21. J.E. Ramirez, Characterization of High-Strength Steel Weld Metals: Chemical Composition, Microstructure, and Nonmetallic Inclusions, *Weld. J.*, 2008, **87**(3), p 65s–75s
22. Z. Praunseis, The Influence of Microstructure on Fracture Toughness of Undermatched Weld Metal, *Kovove Materialy Met. Mater.*, 1999, **37**(4), p 266–279
23. A.N. Kumar, R.K. Pandey, and P. Sundaram, Microstructure-Fracture Toughness Correlation in Weld Joints of Cr-Mo Steel, *J. Mater. Sci.*, 1995, **30**(13), p 3531–3538
24. M.J. Cieslak, J.J. Stephens, and M.J. Carr, A Study of the Weldability and Weld Related Microstructure of Cabot Alloy 214, *Metall. Trans. A*, 1988, **19**(3), p 657–667
25. I.M. Richardson, N.J. Woodward, and J. Billingham, Deepwater Welding for Installation and Repair—A Viable Technology?, *The Twelfth International Offshore and Polar Engineering Conference*, The International Society of Offshore and Polar Engineers, Kitakyushu, Japan, 2002
26. C.E.I. Baixo and J.C. Dutra, Effect of Shielding Gas and Transfer Mode on the Application of 625 Alloy in Carbon Steel, *Soldagem & Inspecao*, 2009, **14**(4), p 313–319 (in Portuguese)
27. M. Ebrahimnia, M. Goodarzi, M. Nouri, and M. Sheikhi, Study of the Effect of Shielding Gas Composition on the Mechanical Weld Properties of Steel ST 37-2 in Gas Metal Arc Welding, *Mater. Design*, 2009, **30**(9), p 3891–3895
28. I. Uygur and B. Gulenc, The Effect of Shielding Gas Compositions for MIG Welding Process on Mechanical Behavior of Low Carbon Steel, *Metalurgija*, 2004, **43**(1), p 35–40
29. N.M.R. de Rissone, I.D. Bott, L.A. de Vedia, and E.S. Surian, Effect of welding procedure (Welding Position, Number of Layers, Arc Energy, and Shielding Gas Type) on ANSI/AWS A5.20-95 E71T1 Flux Cored Wire Deposits, *Sci. Technol. Weld. Join.*, 2003, **8**(2), p 113–122
30. J. Haidar and J.J. Lowke, Effect of CO2 Shielding Gas on Metal Droplet Formation in Arc Welding, *IEEE Trans. Plasma Sci.*, 1997, **25**(5), p 931–936
31. T.K. Pal, S. Dutta, and S.K. Majumdar, Effect of Shielding Gas Composition on Chemistry and Mechanical Properties of Gas Metal Arc Weld Metal, *Trans. Indian Inst. Met.*, 1997, **50**(2–3), p 201–208
32. Z.H. Rao, J. Hu, S.M. Liao, and H.L. Tsai, Modeling of the Transport Phenomena in GMAW Using Argon-Helium Mixtures. Part I—The Arc, *Int. J. Heat Mass Transf.*, 2010, **53**(25–26), p 5707–5721
33. Z.H. Rao, J. Hu, S.M. Liao, and H.L. Tsai, Modeling of the Transport Phenomena in GMAW Using Argon-Helium Mixtures. Part II—The Metal, *Int. J. Heat Mass Transf.*, 2010, **53**(25–26), p 5722–5732
34. J. Haidar, The Dynamic Effects of Metal Vapour in Gas Metal Arc Welding, *J. Phys. D Appl. Phys.*, 2010, **43**(16), p 1–11
35. A.B. Murphy, The Effects of Metal Vapour in Arc Welding, *J. Phys. D Appl. Phys.*, 2010, **43**(43), p 1–31
36. A.B. Murphy, M. Tanaka, K. Yamamoto, S. Tashiro, T. Sato, and J.J. Lowke, Modelling of Thermal Plasmas for Arc Welding: The Role of the Shielding Gas Properties and of Metal Vapour, *J. Phys. D Appl. Phys.*, 2009, **42**(19), p 1–20
37. M. Schnick, U. Fuessel, M. Hertel, M. Haessler, A. Spille-Kohoff, and A.B. Murphy, Modelling of Gas-Metal Arc Welding Taking into Account Metal Vapour, *J. Phys. D Appl. Phys.*, 2010, **43**(43), p 1–11
38. S. Tashiro, M. Tanaka, K. Nakata, T. Iwao, F. Koshiishi, K. Suzuki, and K. Yamazaki, Plasma Properties of Helium Gas Tungsten Arc with Metal Vapour, *Sci. Technol. Weld. Join.*, 2007, **12**(3), p 202–207
39. J. Zähr, M. Schnick, U. Füssel, M. Lohse, and M. Sende, Numerical Investigations of Process Gases and Their Influence on TIG Welding, *Mathematical Modelling of Weld Phenomena 9*, H. Cerjak and N. Enzinger, Ed., Verlag der Technischen Universität Graz, Graz, 2009
40. O.R. Myhr and O. Grong, Dimensionless Maps for Heat-Flow Analyses in Fusion-Welding, *Acta Metall. Mater.*, 1990, **38**(3), p 449–460
41. Ø. Grong, *Metallurgical Modelling of Welding*, Institute of Materials, London, 1997
42. W. Perret, C. Schwenk, and M. Rethmeier, Comparison of Analytical and Numerical Welding Temperature Field Calculation, *Comput. Mater. Sci.*, 2010, **47**(4), p 1005–1015
43. A.S. Azar, S.K. Ås, and O.M. Akselsen, Determination of welding heat source Parameters from Actual Bead Shape, *Comput. Mater. Sci.*, 2012, **54**, p 176–182
44. A.S. Azar, *Modeling of Fatigue Crack Behavior and Microstructure in High Carbon High Strength Q/T Steel Welds*, Department of Materials and Manufacturing Technology, Chalmers University of Technology, Göteborg, 2009, p 102
45. H. Fostervoll and O.M. Akselsen, Deepwater Hyperbaric MIG Welding Procedures Evaluated for Use in Shallow Waters, SINTEF Internal Report, 2009
46. A.S. Azar, N. Woodward, H. Fostervoll, and O.M. Akselsen, Statistical Analysis of the Arc Behavior in Dry Hyperbaric GMA Welding from 1 to 250 Bar, *J. Mater. Process. Technol.*, 2012, **212**(1), p 211–219
47. I.M. Richardson, J.H. Nixon, P. Nosal, P. Hart, and J. Billingham, Hyperbaric GMA Welding to 2,500 m Water Depth, *Joint International Conference ETC/OMAE*, New Orleans, USA, 2000
48. J. Sakakibara and M. Hamasaki, Study on Underwater Dry Hyperbaric TIG Welding, Part I: Effect of Ambient Pressure on Electrode Erosion and Arc Characteristics, *J. High Temp.*, 1983, **9**(1), p 27–31
49. M. Yorizane, S. Yoshimura, H. Masuoka, and H. Yoshida, Thermal Conductivities of Binary Gas Mixtures at High Pressures: Nitrogen-Oxygen, Nitrogen-Argon, Carbon Dioxide-Argon, and Carbon Dioxide-Methane, *Ind. Eng. Chem. Fundam.*, 1983, **22**(4), p 458–463
50. P.C. Jain, The Computation of the Thermal Conductivity of Air in the Temperature Range 400-1600 K, *J. Phys. D Appl. Phys.*, 1977, **10**(17), p 2389
51. Y.S. Touloukian, P.E. Liley, and S.C. Saxena, *Thermal Conductivity: Nonmetallic Liquids and Gases*, IFI/Plenum, New York, 1970
52. B.E. Poling, J.M. Prausnitz, and J.P. O'Connell, *The Properties of Gases and Liquids*, McGraw-Hill, New York, 2001
53. D. Kannappan and T.K. Bose, Transport Properties of a Two-Temperature Argon Plasma, *Phys. Fluid*, 1977, **20**(10), p 1668–1673
54. D. Kannappan and T.K. Bose, Transport Properties of a Two-Temperature Helium Plasma, *Phys. Fluid*, 1980, **23**(7), p 1473–1474
55. W.A. Bowditch and K.E. Bowditch, *Welding Technology Fundamentals*, Goodheart-Willcox Company, Tinley Park, 1997
56. J. Hu and H.L. Tsai, Heat and Mass Transfer in Gas Metal Arc Welding. Part I: The Arc, *Int. J. Heat Mass Transf.*, 2007, **50**(5-6), p 833–846

Paper III

Prediction of the Thermal Cycles in Dry Hyperbaric GMA Welding Using Partial Differential Heat Transfer Equations.

Amin S. Azar, Hans Fostervoll, Odd M. Akselsen.

Trends in Welding Research, 4-8 June 2012, Chicago, USA.

Prediction of the Thermal Cycles in Dry Hyperbaric GMA Welding Using Partial Differential Heat Transfer Equations

Amin S. Azar, Odd M. Akselsen
Department of Engineering Design and Materials, NTNU, Trondheim, Norway
amin.azar@ntnu.no, odd.m.akselsen@sintef.no

Hans Fostervoll
SINTEF Materials and Chemistry, Trondheim, Norway
hans.fostervoll@sintef.no

Abstract

The deepwater hyperbaric GMA welding procedures for subsea pipeline repair are evaluated with respect to its behavior under shallow water conditions. In this study, the welding thermal cycles at three different pressure levels were investigated through experiments and simulations. Conventional thermocouple measurements were utilized along with a 2D heat flow model to identify the effect of weld pool shape on the thermal cycle of the weld. A new approach was assumed for considering the effect of third dimension. It was found that increasing the pressure results in minor changes of characteristic weld thermal cycle features. These variations were considered dependent upon the weld pool shape and size. Good agreement was observed between simulated and experimental results.

Keywords

C-Mn Steel, GMAW, Hyperbaric Welding, FlexPDE, JMatPro

Introduction

Welding under extreme conditions is often required in a variety of industries. Hyperbaric welding is an example that mostly takes place under high pressure subsea conditions [1]. According to earlier studies [2, 3], the welding arc tends to constrict in its root region if ignited under high ambient pressure. Increased pressure level results in a narrower and deeper weld bead shape on its cross section and longer weld pool tail on its top view [4]. Due to the effect of pressure on the size of the weld pool, the thermal cycles of these welds are of importance. The development of residual stresses after welding and microstructural transformations is based on the thermal cycles during the welding process. In this study, a set-up is constructed for recording the thermal gradients at different locations along a weld bead using embedded thermocouples. Additionally, partial differential equations (PDE) were employed to predict the state of transient temperature in a PDE solver with reference to the variations in weld pool size.

Background

Early studies [5] for calculating the temperature distribution around the weld bead consists of an analytical solution for special welding conditions. The heat source was considered as a dimensionless point that can dissipate enormous amount of heat instantaneously on a semi-infinite body. However, the assumptions made for simplicity had confining effects on implementation of those models. For instance, the calculated thermal cycles next to the heat source show an imminent singularity which is impractical experimentally. Nevertheless, the thermal cycles outside those regions can be calculated with a noticeable precision. Numerical models on the other hand, can predict the thermal cycles regardless of aforementioned limiting factors. A recent study [6] compares the analytical and numerical solutions for predicting the thermal cycles. It argues that since the source of implemented formulations is the same for both approaches, the results can be perfectly in agreement if the same boundary conditions are used.

Heat Equation

In order to achieve the heat distribution in a given region of a medium over time, a partial differential equation is defined. For a two dimensional transient pseudo-steady stated heat source, two Cartesian coordination systems can be assigned. A stationary coordination of (x',y) as a reference and a moving coordination system (x,y). x' and x are correlated through the following equation:

$$x = x' - v_x t \tag{1}$$

where v_x is the welding speed along the x axis and t is the arc-on time.
Considering $\mathcal{F}(x',y,t)$ the heat equation reads [7, 8]:

$$\nabla' \mathcal{F} + \rho c_p \frac{\partial T}{\partial t} = q \tag{2}$$

where ∇' is the Laplace operator effective over x', ρ is the density of the medium, c_p is the specific heat capacity, T is the temperature and q is the excessive internal heat including the latent heat of phase transformation.

Equation (2) can be written in the following format with regards to the moving coordination system:

$$\nabla \mathrm{F} + \rho c_p v_x \frac{\partial T}{\partial t} = 0 \qquad (3)$$

where ∇ is the Laplace operator over x. By defining the boundary conditions for Equation (3), a PDE solver can plot the heat distribution during the welding process.

Heat Source and Boundary Conditions

A Gaussian heat source travelling on the surface was considered in this simulation. Figure 1 shows the configuration of the heat source. The following equation was used to define the heat distribution on the surface [9]:

$$Q(x) = \frac{\eta UI}{2\pi\sigma^2} e^{-x^2/2\sigma^2} \qquad (4)$$

where Q is the distribution function over x, η is the arc efficiency factor, U is the arc voltage, I is the current and σ^2 is the distribution variance. The value of variance is a factor reflecting the dimensions of the heat source.

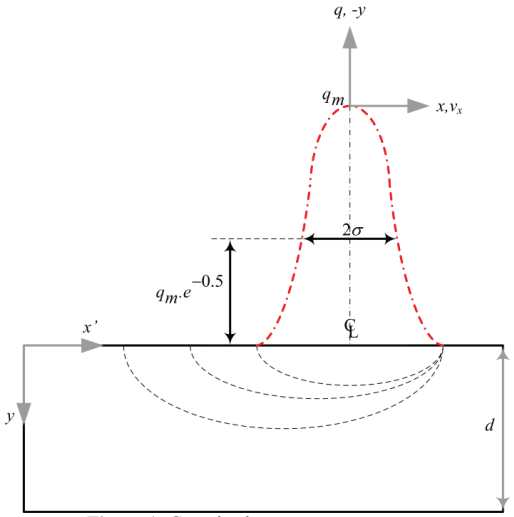

Figure 1: Gaussian heat source parameters.

Assuming that the effective heat flux is at about 99.7% of the distribution set [10], the widest part of the distribution bell on the surface should have the distance of 3σ from the center line. Thus, the dimension of the heat source on the surface should correspond to 6σ.

Experimental Investigations

To study the welding thermal cycles at different pressures, thermocouple measurements were carried out during the process. Three pressure levels of 1, 17 and 35 bar were chosen representing a low, medium and high pressure range. The experiments were performed in one pass bead-on-plate condition. The welding current and voltage used in this study are reported in Table 1. The welding speed was set to 7 mm/s. The boundary conditions except the heat source parameter were kept constant for all the cases. Since the convection and radiation are not affected by constant ambient pressure, the heat loss from the surface was considered negligible. However, for obtaining good results the arc efficiency factor should be calibrated with care. Moreover, the welding was assumed to be autogenous without any filler material.

Three R-type (Pt/Pt-Rh) thermocouples for each test weld were positioned in the heat affected zone (HAZ) region close to the fusion line as illustrated in Figure 2. Since the depth of penetration varies at different pressures, the distance between the thermocouples' head to the fusion line remains unknown until the welding is completed. However, the depth of thermocouple bores was chosen 27.5 mm for 1 bar welding and 26.5 mm for 17 and 35 bar cases. Figure 3 shows the post-welding test plate.

Figure 4 depicts the end craters of weld beads after welding. They represent the style of the weld pool from top view.

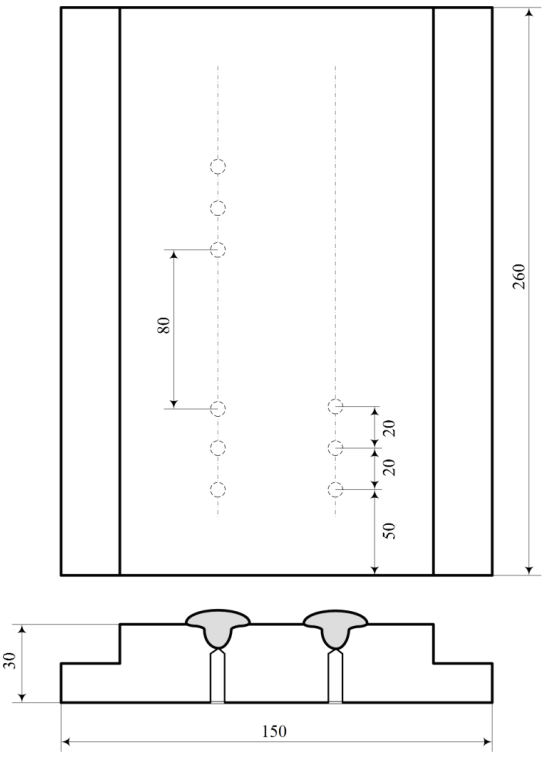

Figure 2: Arrangement of the thermocouples inside the test plate.

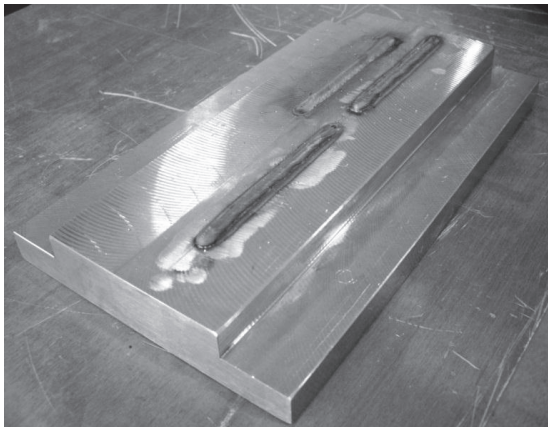

Figure 3: Instrumented test sample after welding.

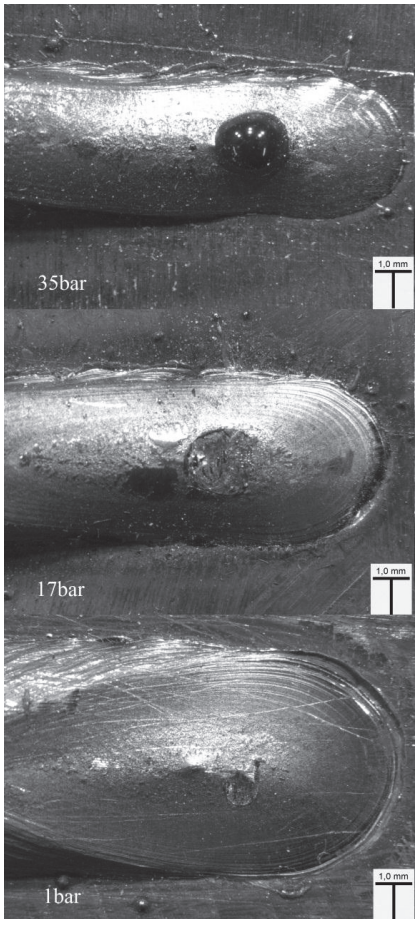

Figure 4: The end crater shape representing the weld pool size and style from top view

The Model

In two dimensional models, the effect of weld pool extension in the third dimension has always been ignored. In hyperbaric welding however, the size of the weld pool undergoes a variation in all three dimensions. In order to implement the correct weld pool size, the weld bead cross-section profile as well as the end crater was measured after welding. Figure 5 shows a schematic illustration of the weld pool with three representative dimensions. The measured values are reported in Table 1 with reference to Figure 5.

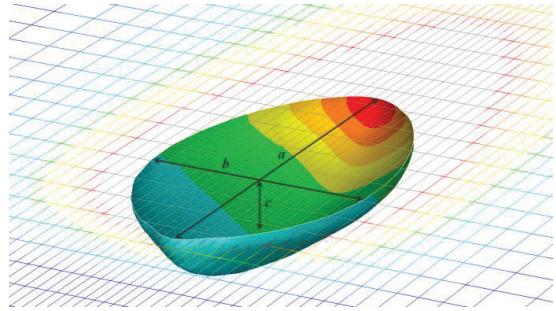

Figure 5: Schematic presentation of the weld pool.

A volumetric factor was defined which can be calculated by multiplying the dimensions of the weld pool. This factor is the volume of the smallest cuboid that embraces the weld pool. Because the Gaussian distribution is symmetrical in all three dimensions when stationary, the resultant weld pool on the surface should be circular from the top view. As a result, the rectangular surface of the cuboid may not fully surround the circle caused by Gaussian distribution unless it is a perfect square. For this purpose, the volume of the weld pool was considered a cube, each side equal to the cube-root of the pre-calculated volumetric factor. The latter value is equal to 6σ in the Gaussian distribution. Eventually, the input term of the modeled heat source dimensions can be calculated if the recent value is divided by 3. Several simulations have shown that the described approach can include the effect of the eliminated third dimension to a great extent. As a result, the initial calibrations were done on the welding data for the 1-bar-case and the rest were simply adjusted on their heat source dimensions. The 2σ value of 1 bar case was multiplied by 98.9% in 17 bar model and 101.4% in 35 bar model.

Since there is limited information about the thermal data of the base metal (C-Mn steel), the required information was computed by JMatPro software using the chemical composition of the material. Figure 6 shows how some thermal data are varying as temperature increases. It should be clarified that the average values were considered in the model for the sake of simplicity.

Pressure [bar]	Voltage [V]			Mean Current [A]			*a* [mm]	*b* [mm]	*c* [mm]	Volumetric Factor (*a* x *b* x *c*)
	Mean	**Min.**	**Max.**	**Mean**	**Min.**	**Max.**				
1	19.51	-22.75	50.46	235.56	47.26	474.64	12.3	8.4	2.2	228.7
17	18.16	-19.69	50.13	244.85	68.52	489.35	13.5	5.7	2.8	221.2
35	17.56	-22.94	56.28	255.81	58.13	473.96	15.8	4.2	3.6	238.9

Table 1: Welding parameters at three different pressures and the resultant weld pool dimensions.

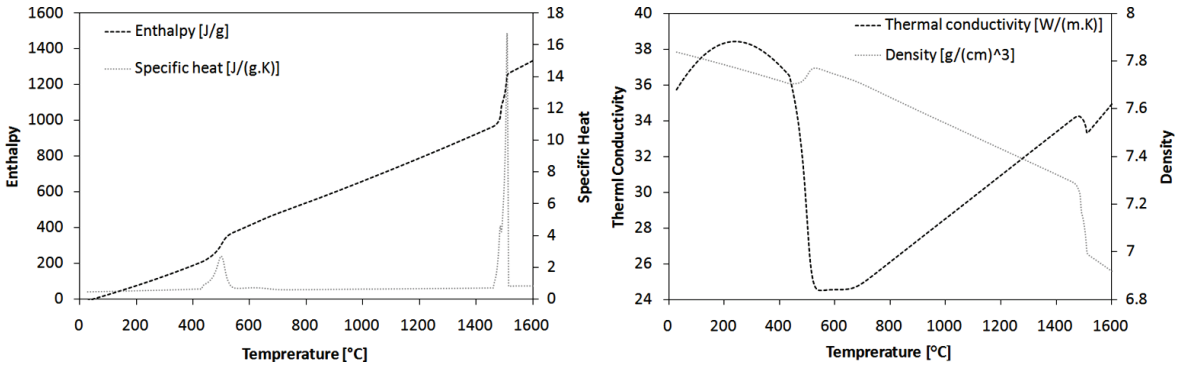

Figure 6: The variation of thermal properties with respect to temperature.

Results and Discussion

Figure 7 shows the heat flux vectors and temperature distribution in the material. In the temperature distribution figure, (**x**) mark is indicating the maximum and (**o**) mark is indicating the minimum temperature locations. It should be noted that the start and stop positions of the weld was defined according to the experimental process as shown in Figures 2 and 3. The locations of the thermocouples were also defined based on the measurements after experimental work. Table 2 presents some measured and simulated values of weld cooling cycles. The austenite retentions time may not be comparable in different curves since it is strongly affected by the position of peak temperature. However the simulations results are still comparable with experimental ones. Placing the thermocouples in the same level very close to the fusion line in the simulation phase has shown that the austenite retention time steps up very little since peak temperature at subsequent thermocouple locations increases compared to the earlier peaks.

Figure 8 illustrates the simulated and measured thermal cycles of the welds at 1, 17 and 35 bar. It can be seen that one of the fundamental differences in the simulated and experimental figures is in their heating rate. Experimental curves are showing steeper rate compared to the simulated counterparts. This can be the major reason for time scale drift of simulated peak temperatures and cooling cycles.

Figure 9 shows the visual comparison between the cooling rate and austenite retention time. No general trend can be detected in neither of the figures unless average values of both simulated and experimented cooling rates are considered for comparison. Figure 10 depicts the aforementioned average values. It can be seen that more concentrated heat generation at higher pressures results in higher localized heat accumulation which brings relatively faster cooling rate about. The cooling rate decreases a little at 35 bar since the overall combination of weld pool size and welding parameters are affecting the thermal cycles.

Investigation of the weld metal shows that minor variations of $\Delta t_{8/5}$ has imperceptible effect on the microstructure. Figure 11 illustrates the micrographs at three different pressure levels. It consists of acicular ferrite inside the prior austenite grains and some grain boundary ferrite. Widmanstätten ferrite and some bainite patches were also detected in all three micrographs. It was found that the number of bainite patches and their size decline when the cooling rate decreases. The microstructure of the weld metal may change if the dilution of the consumable and base material is susceptible to phase transformation in the variation range of $\Delta t_{8/5}$. Thus, the thermal properties and the susceptibility to phase transformation are determinant when selecting the base material.

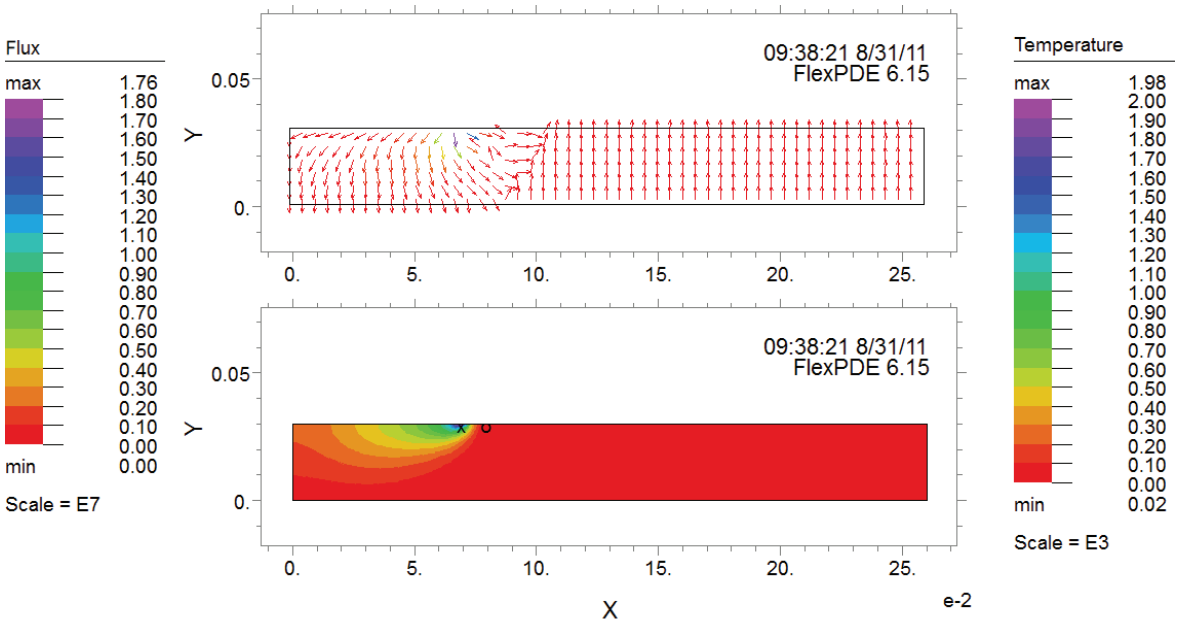

Figure 7: Heat flux (W/m^2) vector space and temperature (°C) distribution.

Pressure	#	Δt (800-500)		800°C Retention Time		Peak Temp. (°C)	
		Simulated	Experiment	Simulated	Experiment	Simulated	Experiment
1 bar	TC1	1.8	2.2	1.6	1.9	1452	1466
	TC2	2.9	2.5	1.9	2.2	1225	1285
	TC3	3.1	2.4	2.1	2.6	1291	1226
17 bar	TC1	1.1	2.1	1.1	0.8	1251	1295
	TC2	1.9	1.7	0.7	0.5	878	882
	TC3	2	1.5	1	0.6	961	948
35 bar	TC1	1.3	1.6	1.3	1.1	1413	1423
	TC2	2.1	1.8	1.6	1.3	1388	1404
	TC3	2.3	2	1.5	1.3	1277	1306

Table 2: Experimented and simulated characteristics of thermal cycles.

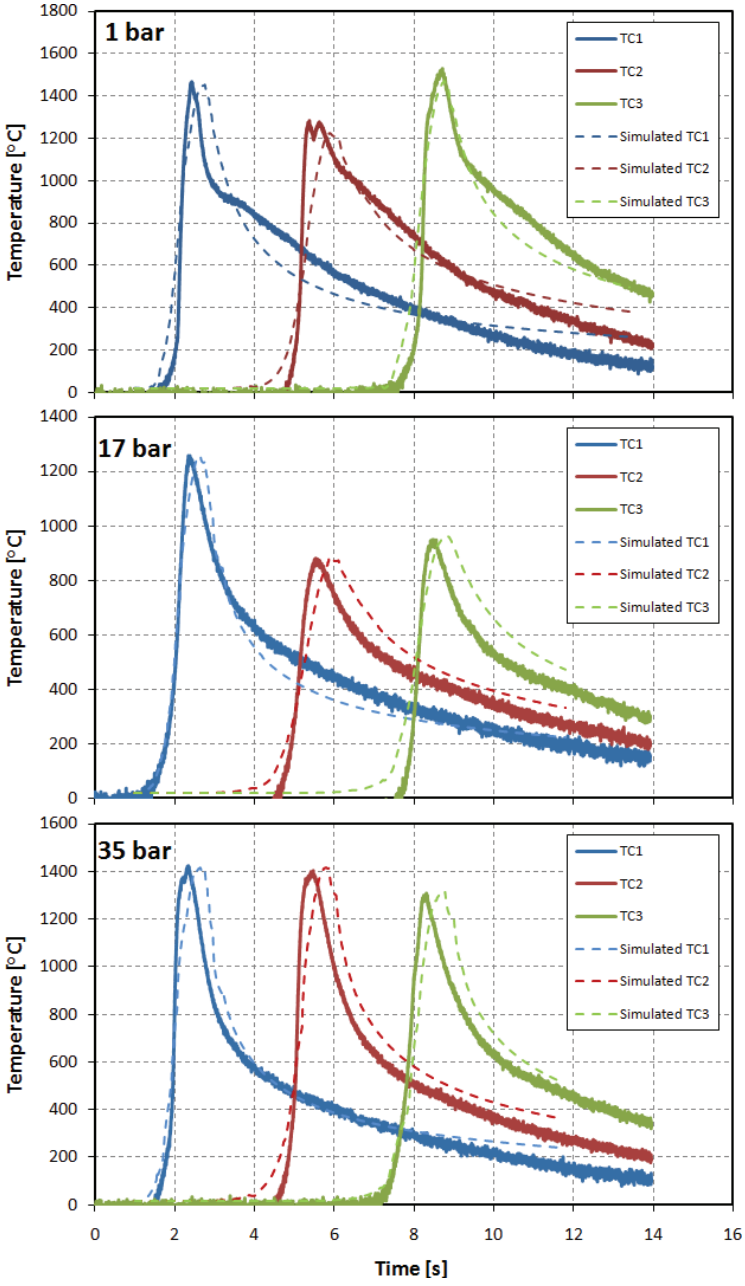

Figure 8: Thermal cycles at different pressures.

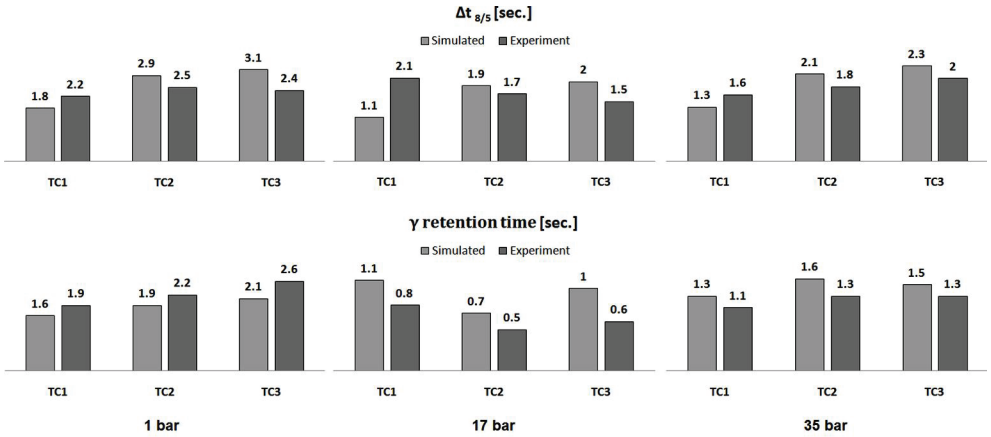

Figure 9: Visual presentation of cooling time and austenite retention time.

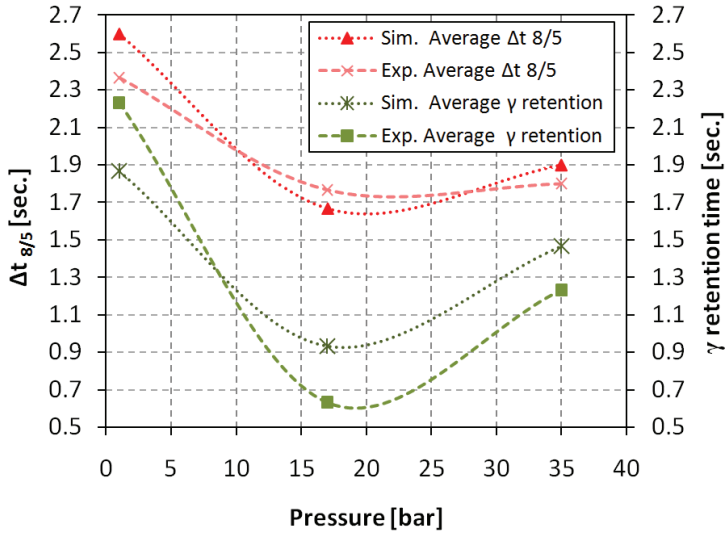

Figure 10: Comparison between simulated and experimented features of the thermal cycles.

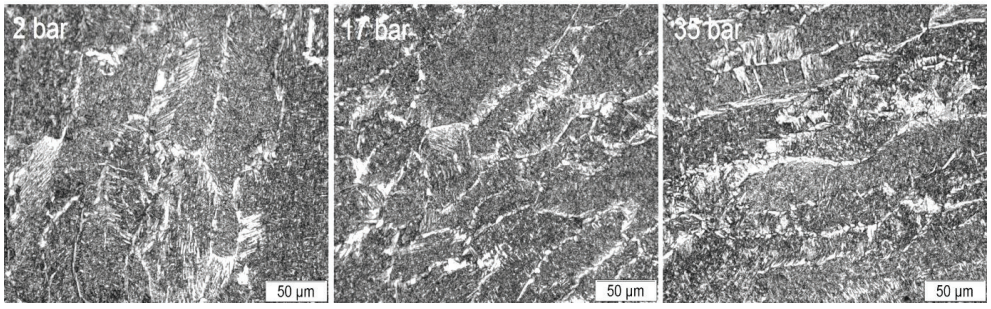

Figure 11: Microstructure of the weld metal at different pressure levels.

Conclusions

- Good agreement between simulated and experimental results was observed. Despite simplified boundary conditions, the results show that using such simple software as well as the employed approach can be useful in terms of understanding the effect of weld pool shape.

- A dominant trend could not be identified in any sub categories being investigated. The average values from different cases and further simulations revealed an undefined trend for $\Delta t_{8/5}$, austenite retention time and the peak temperature as pressure increased. Nevertheless, the range of variation was minor.

- The simulated cooling rates were underestimated or overestimated in different instances compared to the experiments. The deviation is fairly small, not exceeding more than 0.2 seconds in average. That might be due to some physical errors in the experimental data because of stray welding noises.

- The minor variation in the cooling rate and the altered weld pool size and dynamics because of elevating ambient pressure did not reveal any substantial changes in the microstructure of the weld metal.

Acknowledgments

The financial support from the Norwegian Research Council (Contract No. 192967/S60), Statoil, Gassco, Technip and EFD Induction is gratefully acknowledged.

References

[1] Jones, G. R., High Pressure Arcs in Industrial Devices, Cambridge University Press, 1988.
[2] Richardson, I. M., *Ph.D. Thesis*, Cranfield University, 1991.
[3] Richardson, I. M., Woodward, N. J., Billingham, J. "Deepwater Welding for Installation and Repair – A Viable Technology?", *The Twelfth (2002) International Offshore and Polar Engineering Conference, The International Society of Offshore and Polar Engineers, Kitakyushu, Japan, 2002.*
[4] Allum, C. J., "The Characteristics and Structure of High Pressure (1-42bars) Gas Tungsten Arcs"*, Ph.D. Thesis*, Cranfield University, 1982.
[5] Rosenthal, D., "The Theory of Moving Sources of Heat and its Application on Metal Treatments" Trans. ASME, (1946) pp.849-866.
[6] Perret, W., Schwenk, C., Rethmeier, M., "Comparison of analytical and numerical welding temperature field calculation", Comp Mater Sci, 47 (2010) pp.1005-1015.
[7] Backström G., Fields of Physics; by Finite Element Analysis, GB Publishing, Malmö, Sweden, 2005.
[8] Mills, A. F., Heat and Mass Transfer, Richard D. Irwin Inc., 1995.
[9] Tsai, N.S., Eagar, T. W., "Changes of Weld Pool Shape by Variations in the Distribution of Heat Source in Arc Welding", J. A. Dantzig, J. T. Berry (Eds.) *Modelling of Casting and Welding Processes II*, AIME, New York, 1984.
[10] Simon, M. K., Probability Distributions Involving Gaussian Random Variables: A Handbook for Engineers, Scientists and Mathematicians, Springer, New York, 2006.

Paper IV

Determination of Welding Heat Source Parameters from Actual Bead Shape.
Amin S. Azar, Sigmund K. Ås, Odd M. Akselsen.
Computational Materials Science 54 (2012) 176–182.

Computational Materials Science 54 (2012) 176–182

Contents lists available at SciVerse ScienceDirect

Computational Materials Science

journal homepage: www.elsevier.com/locate/commatsci

Determination of welding heat source parameters from actual bead shape

Amin S. Azar [a,*], Sigmund K. Ås [b], Odd M. Akselsen [a,b]

[a] Department of Engineering Design and Materials, NTNU, Trondheim, Norway
[b] SINTEF Materials and Chemistry, Trondheim, Norway

ARTICLE INFO

Article history:
Received 14 September 2011
Received in revised form 5 October 2011
Accepted 20 October 2011
Available online 13 December 2011

Keywords:
Distributed heat source
Double-ellipsoidal heat source
Weld bead geometry
WeldSimS

ABSTRACT

Analytical and numerical approaches are used to model a gas metal arc welding (GMAW) process. In order to simulate the detailed aspects of material changes during the process, it is important to implement the correct size and distribution of the heat source. In this study the dimensions of a heat source model in a welding case will be calculated based on experimentally observed weld pool sizes. An analytical approach called 'discretely distributed point heat source model' will be used for this purpose as an intermediate stage between the experiments and the numerical model. In the numerical approach, the heat source will be split into two perpendicular 2D ellipsoidal sources that correspond to the double-ellipsoidal heat source model. The third dimension of the heat source will be measured from the top-view of the end crater. WeldSimS and Matlab codes are used for finite element and analytical investigations respectively. Both models were compared and analyzed with respect to similar boundary conditions. Numerical simulations show good agreement with the analytical approach calibrated by actual weld dimensions.

1. Introduction

Fusion welding of metals is a process that comprises a heating and a cooling cycle. Quantifying the thermal gradients and temperature fields during successive welding cycles inside different groove geometries is of crucial importance since these may strongly influence chemical–metallurgical reactions in the liquid metal, grain growth, solid state phase transformations, and hence the resultant mechanical properties. In order to simulate the final properties of a weld, a realistic heat source shape and distribution is required [1].

Rykalin [2] and Rosenthal [3] were amongst those who developed heat sources using Fourier's heat conduction law which is applicable for moving heat sources. They considered the heat source as a dimensionless point that can supply a constant amount of net power as it moves steadily along a straight line. Even though this formulation leads to singularity of the heat flux and temperature distribution in the material adjacent to the heat source, the cooling rates can be calculated with reasonable accuracy.

Point heat sources are in many cases unable to represent the actual welding heat flux since the weld bead deviates from semi-circular shape due to a number of factors. Researches were carried out to define a better solution compared to the point heat source [4–8]. Prior to Rosenthal's moving point heat source model, Sprargen and Claussen [9] have reviewed the moving line heat source that had better control on the heat distribution in one dimension. However, a single line source can never be matched precisely to the geometry of the weld.

Amongst the early models, Pavelic et al. [10] suggested using a type of volumetric heat source. They assumed that the deposited heat flux is perfectly distributed with Gaussian characteristics over the surface of the material. However, the resultant weld pool was semi-hemispheric which can only be controlled in one dimension. The shape of this heat source on the surface is circular which is moving along the welding direction. Pavelic 'disc' was later implemented in FEM simulations [11,12]. A more complete history of transient heat source evolutions is given in [1].

Myhr and Grong [13,14] proposed a discretely distributed point heat sources model. This analytical model is calibrated using an actual weld cross section. However, it does not predict the heat distribution along the weld direction since the distribution of heat flux in the welding direction is ignored.

Goldak et al. [15] developed a model which approximated the weld pool geometry as a heat source using a three dimensional double-ellipsoidal configuration. They described the volumetric heat flux density distribution by the following equation:

$$q_s(x,y,t) = \frac{3Q}{\pi r^2} e^{-3[(-vt)^2]/r^2} e^{-3y^2/r^2} \quad (1)$$

where Q denotes the total power, v is the welding speed, t is the time and r is the surface heat source radius. Each of the volumetric

* Corresponding author. Address: Norwegian University of Science and Technology (NTNU), Department of Engineering Design and Materials, Richard Birkelands Vei 2B 7034, Trondheim, Norway. Tel.: +47 96833668.
E-mail address: amin.azar@ntnu.no (A.S. Azar).

0927-0256/$ - see front matter © 2011 Elsevier B.V. All rights reserved.
doi:10.1016/j.commatsci.2011.10.025

sources consists of the front and rear heat flux distribution ellipsoidals defined by the following equations:

$$q_{if}(x,y,z,t) = \frac{6\sqrt{3}f_f Q}{abc_f\pi\sqrt{\pi}} e^{-3|(x-vt)^2|/c_f^2} e^{-3y^2/a^2} e^{-3z^2/b^2} \quad (2)$$

$$q_{ir}(x,y,z,t) = \frac{6\sqrt{3}f_r Q}{abc_r\pi\sqrt{\pi}} e^{-3|(x-vt)^2|/c_r^2} e^{-3y^2/a^2} e^{-3z^2/b^2} \quad (3)$$

where i is 1 or 2 representing two volumetric heat sources and f_f and f_r are the front and rear distribution fractions respectively. a, b, c_f and c_r are the dimensions depicted in Fig. 1. The description of welding, transverse and perpendicular directions (x, y, z) are also given in Fig. 1 with respect to the implemented heat source.

It was shown that the models after Pavelic et al. [10], Paley and Hilbbert [16] and Westby [17] were special cases of this model. Although the Goldak's model is considered as the most complete one thus far, the formulation using a single heat source has shortcomings when investigating phenomena like argon finger and keyhole welding.

Aarbogh et al. [18] superimposed a number of double-ellipsoidal heat sources to produce a weld bead that is similar to the actual one. Despite satisfactory results, the identification of double-ellipsoidal heat source parameters was not straight forward. The volumes of heat sources, the dimensional values, the fraction of the heat flux per each heat source and the location of the heat sources with respect to each other were found by trial and error.

Even the parameters of single 'double-ellipsoidal' heat source may be identified with insufficient care. Gery et al. [19] visualized the heat flux distribution in the front and rear section of the heat source. Improper selection of fraction factors in the formula may result in a non-continuous maximum heat flux that may affect the simulation results.

The scheme of the present work is to find the primitive dimensional data that can be implemented in the finite element models. Since the analytical model after Myhr and Grong should be calibrated with an actual bead shape, this model was employed as an intermediate step towards finding the dimensions and distribution of double-ellipsoidal model. The parameters required by the latter model can be extracted from the analytical model without any single tentative step requirement.

2. Analytical model

In Myhr and Grong's model [13,14], the heat source is considered as discretely distributed point sources. These sub-sources are arrayed in perpendicular and transverse direction with respect to the welding direction as shown in Fig. 2A and the temperature rise at point P is sought. The plate thickness of d is taken into account similar to medium thick plate solution after Rosenthal [3]. The specimen surfaces are assumed adiabatic prohibiting any heat loss. As a result, the heat flux travels through the plate thickness and increases the temperature. Since the surfaces are impermeable to heat, the generated amount of heat should be reflected backwards if reached to the surfaces. The interference of the heat reflections from two parallel surfaces of the specimen brings the temperature attenuation about. The aforementioned reflections from the surface can be introduced using the method of imaginary heat sources [14]. In this method, a number of fictitious sources are placed above and below each sub-source for simulating the reflection of the surfaces. Fig. 2B depicts how the imaginary heat sources and sub-sources are arranged. The vectors are showing the distance between any real or imaginary heat source and the observation point P. The right hand side observation point P and vectors represent the arrangement of imaginary heat sources relevant to the distributed point heat sources on the surface. On the other hand, the left hand side observation point P and imaginary heat sources are representing the distributed heat sources with respect to the sub-surface points. It should be noted that only one observation point is required for all the heat sources, though, it is presented separately for better labelling.

It can be seen from Fig. 2 that the transverse and perpendicular arrays of the sub-sources (black nodes •) are set apart from each other with equal distances. The term δ is the distance between the first sub-surface heat source and the plate surface. The subsequent sub-surface heat sources are 2δ, $3\delta,\ldots,\alpha\delta$ away from the surface. The number of sub-sources (α) is arbitrary, though it was found that for obtaining good results, 8–10 sources are sufficient. Total heat emission should satisfy the following equation:

$$q_0 = \sum_i (q_t^i + q_p^i) = \eta UI \quad (4)$$

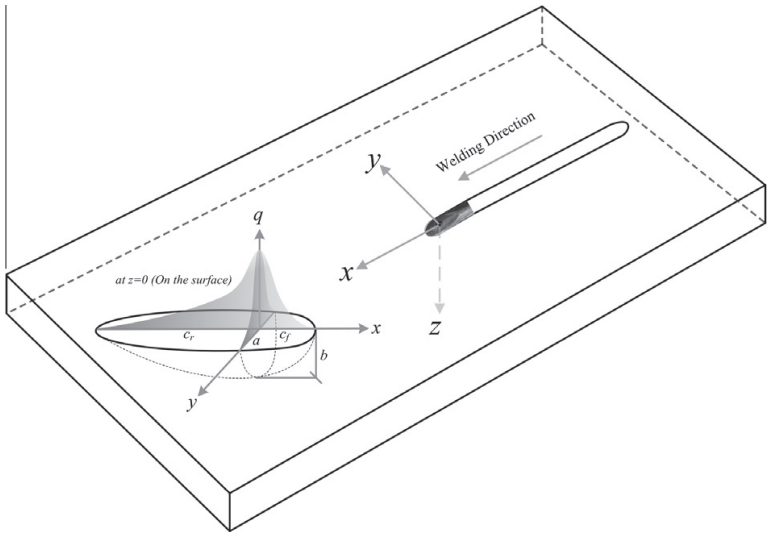

Fig. 1. Double-ellipsoidal (Goldak) heat source parameters.

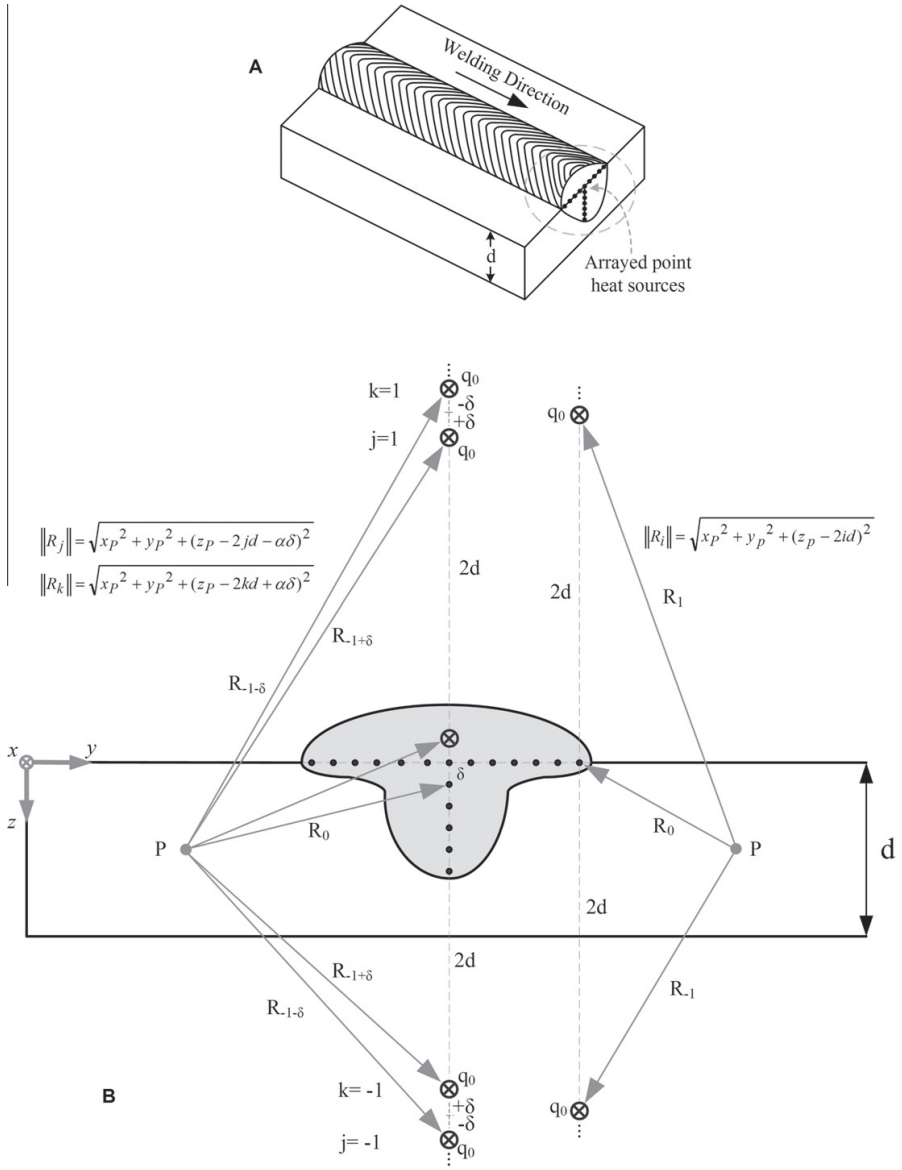

Fig. 2. The positioning of imaginary heat sources (A) sub-sources, (B) imaginary sources of transversal and perpendicular sub-sources.

where q_0 is the total heat flux, q_t and q_p are the heat flux from each transversely and perpendicularly arrayed sub-source, η is the arc efficiency factor, U is the arc voltage and I is the arc current. The number of imaginary heat sources (crossed-open nodes ⊗, however, was found to have a negligible effect if exceeded more than five in this case study. More reflections may be required for higher accuracy when the plate is thinner [20].

The contribution of all transversely arrayed heat sources and respective images at point P are described by the following equations:

$$T(q_t) = \frac{q_t}{2\pi\lambda}\exp\left(-\frac{vx}{2a}\right) \times \left[\sum_{i=-\infty}^{+\infty}\frac{1}{R_i}\exp\left(-\frac{v}{2a}R_i\right)\right] \quad (5)$$

where $R_i = \sqrt{x_P^2 + y_P^2 + (z_P - 2id)^2}$.

The contribution of all perpendicularly arrayed heat sources and respective images are:

$$T(q_p) = \frac{q_p}{4\pi\lambda}\exp\left(-\frac{vx}{2a}\right) \times \left[\sum_{j=-\infty}^{+\infty}\frac{1}{R_j}\exp\left(-\frac{v}{2a}R_j\right) + \sum_{k=-\infty}^{+\infty}\frac{1}{R_k}\exp\left(-\frac{v}{2a}R_k\right)\right] \quad (6)$$

where $R_j = \sqrt{x_P^2 + y_P^2 + (z_P - 2jd - \alpha\delta)^2}$ and $R_k = \sqrt{x_P^2 + y_P^2 + (z_P - 2kd + \alpha\delta)^2}$.

The temperature rise at point P is the sum of all arrayed and imaginary heat sources:

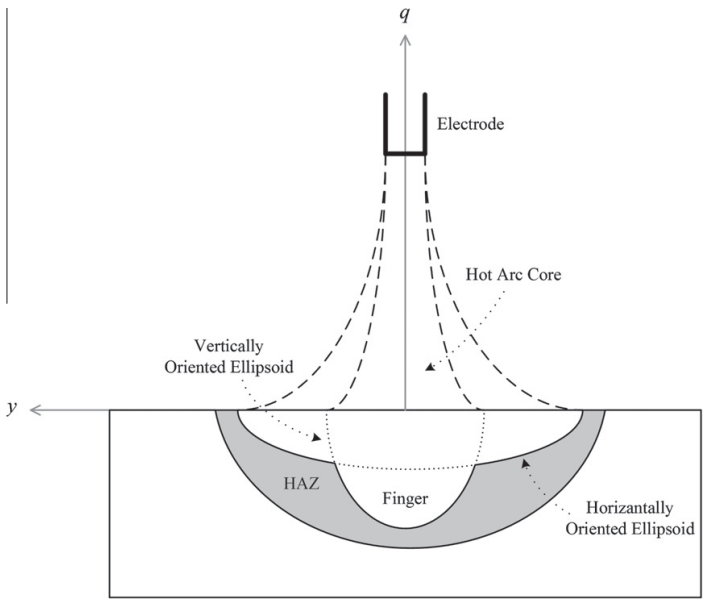

Fig. 3. Estimation of fusion zone by a couple of half ellipsoids.

$$T_t - T_0 = \sum_i [T(q_t)_i + T(q_p)_i] \quad (7)$$

The isotherms of interest can be plotted using Eq. (7). The physical properties of the materials such as λ and a, can be either measured experimentally or simulated.

When the cross section of the weld shows a finger or a deeper penetrated section, the area can be fit by a couple of vertically and horizontally ellipsoidal heat sources as depicted in Fig. 3, each of which constructed with respect to a and b parameters shown in Fig. 1.

Using Myhr and Grong's model, the vertically and horizontally oriented ellipsoids can be calculated if the presence of either of them is ignored. For instance, in order to calculate the locus of horizontally oriented ellipsoid, the presence of vertically arrayed sub-heat sources should be ignored. In this case, the extent of fusion zone that correspond to the double-ellipsoidal heat source parameters can be calculated. The maximum heat flux distribution was found through numerical iterations to prevent mismatching maximum temperature value in the front and rear sections of double-ellipsoidal heat source.

3. Numerical simulation results and discussion

Table 1 shows the welding parameters that are going to be applied in this investigation. The model after Myhr and Grong was programmed in Matlab to visualize the isotherms of interest. The physical properties as well as the isotherms of interest were chosen based on the thermal data of a conventional pipeline steel and the other variables were defined based on the calibration procedure. The three chosen isotherms are shown in Fig. 4. The left side of the isotherms were not calculated due to symmetry.

Fig. 5 shows the vertically and horizontally oriented ellipsoids. The red fusion line in Fig. 4 can be obtained if both ellipsoids contribute. The depth (z) and width (y) of both ellipsoids were reported as a and b respectively, corresponding to that of Goldak's double-ellipsoidal model. The front (c_f) and rear (c_r) dimensions

Table 1
Welding parameters.

Variable	Dimension	Value
Current, I	A	250
Voltage, U	V	30
Arc efficiency, η	–	0.8
Welding speed, V	mm s^{-1}	10
Preheating temperature, T_0	°C	20
Thermal conductivity, λ	W mm^{-1} $°C^{-1}$	0.036
Thermal diffusivity, a	mm^2 s^{-1}	8
Plate thickness, d	mm	18
Distance between subsurface heat sources, δ	mm	0.7
Number of vertical and horizontal heat sources, α	–	8

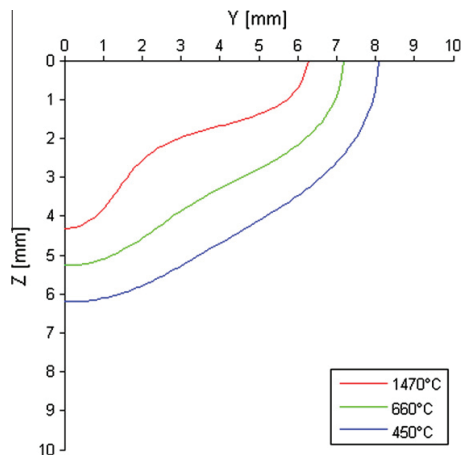

Fig. 4. Three isotherms based on Myhr and Grong's model.

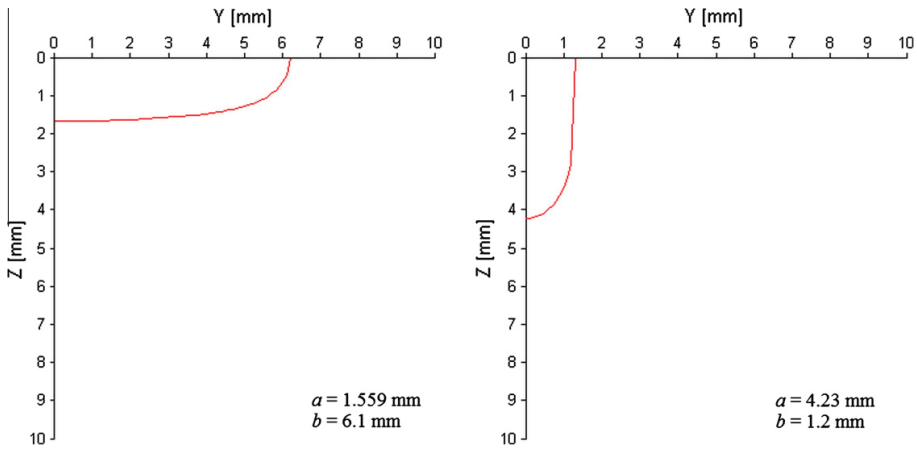

Fig. 5. Horizontally (left) and vertically (right) oriented ellipsoids of the fusion line shown in Fig. 4.

of the heat flux distribution were also obtained based on the calibration as shown in Fig. 6.

The front and rear fractions of heat flux distribution can also be calculated using the following equation [21]:

$$f_f = 2\frac{c_f}{c_f + c_r} = 2 - f_r \tag{8}$$

However, the best fit in the maximum front and rear flux was calculated using an iterative code in Matlab, confirming the obtained values from Eq. (8).

In Fig. 7, the calculated heat flux according to Eqs. (1)–(3) is shown. The wide and narrow heat sources are referred to those in Fig. 5 that were oriented horizontally and vertically respectively. The front and rear dimensions of the weld pool were adapted from a real case measurement shown in Figs. 6–8 depicts the superposition of wide and narrow heat sources with the cumulative flux level of both heat sources.

A finite element welding simulation code (WeldSimS) [22] was employed to implement the calibrated heat source parameters.

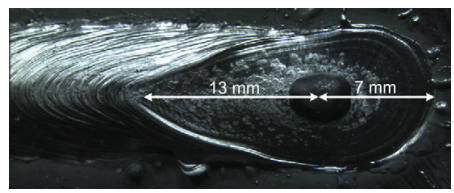

Fig. 6. Calibration of front and rear sections based on the end crater geometry.

Using the welding parameters in Table 1 and the heat source dimensions reported in Fig. 7, two simultaneous double-ellipsoidal heat sources were incorporated in the model. The model consists of a finite plate with a refined mesh around the welding region. Fig. 9 shows the plate and meshing quality.

The contribution of each heat source was adjusted using their maximum heat flux intensities as reported on the scale bars of Figs. 7 and 8. The best fit was found when equal amount of heat is dissipated from both sources. In order to equalize the heat input

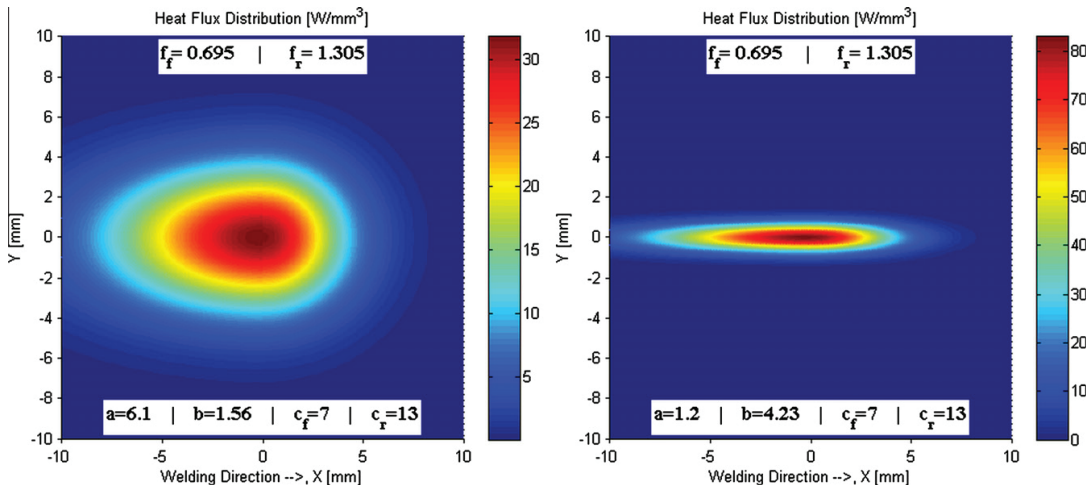

Fig. 7. Separate visualization of wide and narrow distributions in Fig. 5.

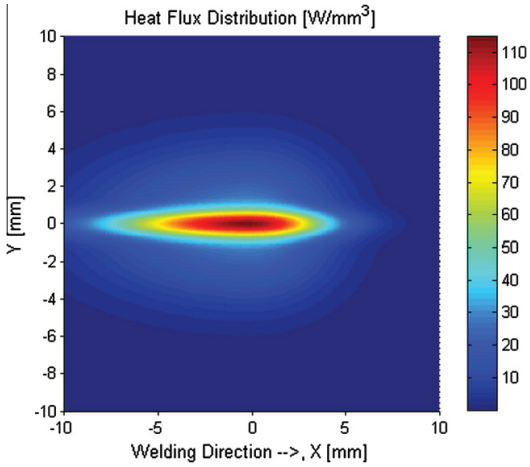

Fig. 8. Visualization of superimposed heat flux.

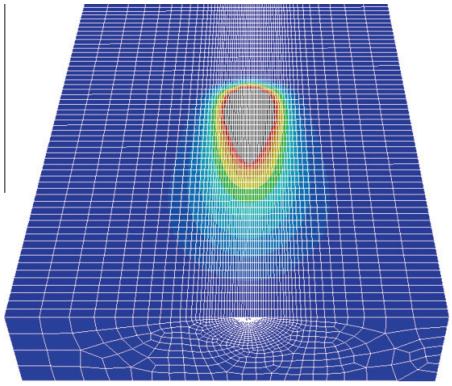

Fig. 9. The model of slab and meshing condition.

values of both heat sources, the product of voltage and current of each was multiplied by the heat flux fraction of the other one. In this case for instance, the wide heat source is about 27.3% of the total heat flux and the narrow heat source contributes 72.7%.

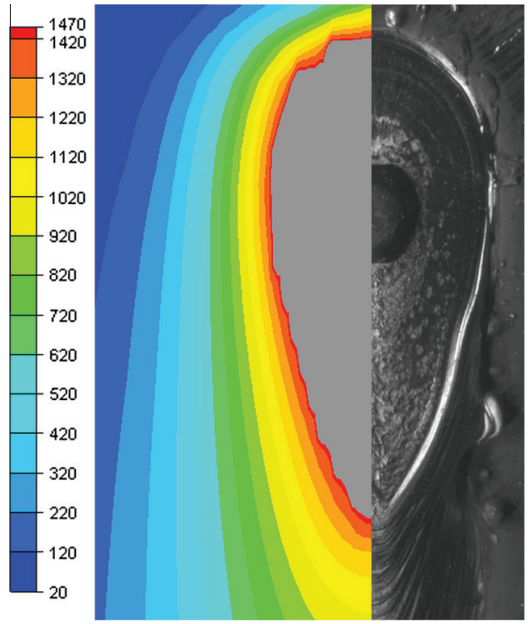

Fig. 10. Comparison between the simulated and experimented weld pool shape.

The start and stop positions of the welding were set about 20 mm from the edges in order to prevent heat permeation from side walls. In order to simulate the same conditions, the thermal properties were set to constant as reported in Table 1. Moreover, the heat loss from the surface following the Stefan–Boltzmann law was ignored to account for the net heat flux. The filler material was also ignored for the sake of comparability with the analytical model.

It can be seen from Fig. 8 that the superimposed heat source presents a sharp nose in the front section along the welding direction. Since the actual weld bead does not show such feature, it should be truncated. However, the truncation reduces the area over which the heat flux is distributed and results in an increased transfer of heat flux per unit area. In order to resolve this, the narrow heat source was set to start with a few milliseconds of delay, following the wider one. The outcome did not show any major change in the length of the weld pool.

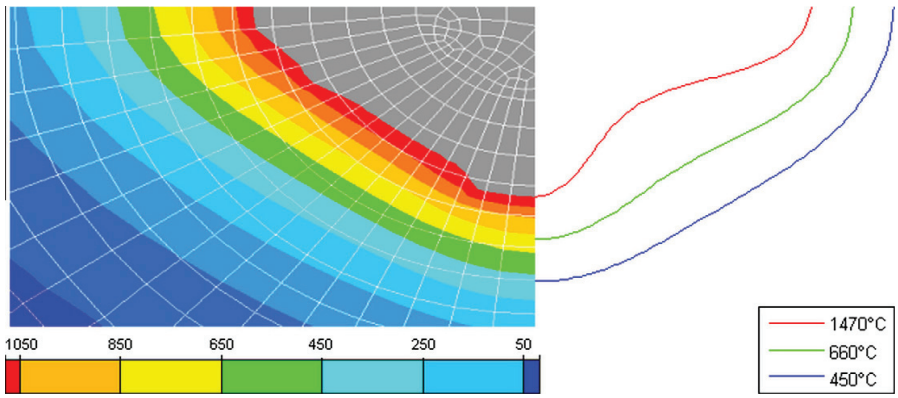

Fig. 11. Comparison between the numerical and analytical models.

Fig. 10 shows the simulated weld pool shape compared to the actual one. The border of the gray area is representing the 1470 °C isotherm which is the melting point of the base material. The unevenness of the fusion line is due to the meshing effect. Finer mesh elements are required for smoother curves.

Fig. 11 illustrates the comparison between the cross section of the double-ellipsoidal numerical model with Myhr and Grong's analytical solution. It shows that by applying the same parameters, the calibrated dimensions of the heat source may represent the post-weld actual bead geometry.

4. Conclusion

- A correlation between analytical and numerical models was established. It was shown that the analytical model of a heat source, calibrated using the actual weld bead geometry, can be implemented in the numerical simulations. Coming up with the correct welding heat source dimensions may be necessary for further simulations (e.g. microstructure modelling, residual stresses modelling, etc.).
- The spent time for finding heat source parameters by trial and error will be reduced noticeably. Due to the fast computational speed of this analytical method (about 2 s), the required parameters can be calculated in a fairly short time.
- Since the employed analytical model can be used for both thick and thin sheets with high precision, it can be used for calibrating almost any linear bead-on-plate configuration. Numerical model can predict the cases with more complex geometry using the same heat source parameters as calibrated with analytical model in advance.
- Using the reviewed procedure may promote the correct implementation of unconventional weld pool shapes as in laser and laser hybrid welds. The effect of shielding gases in GMAW could be studied with this approach as well.

Acknowledgment

The financial support from the Norwegian Research Council (Contract No. 192967/S60), Statoil, Gassco, Technip and EFD Induction is gratefully acknowledged.

References

[1] J.A. Goldak, M. Akhlaghi, Computational Welding Mechanics, Springer, US, 2005.
[2] N.N. Rykalin, VEB Verlag Teknik, Berlin, 1953.
[3] D. Rosenthal, Trans. ASME (1946) 849–866.
[4] C.S. Wu, H.G. Wang, Y.M. Zhang, Weld. J. 85 (2006) 284s–291s.
[5] T. Terasaki, T. Kitamura, T. Akiyama, M. Nakatani, Sci. Technol. Weld. Joint 10 (2005) 701–705.
[6] D.H. Bae, C.H. Kim, S.Y. Cho, J.K. Hong, C.L. Tsai, KSME Int. J. 16 (2002) 1054–1064.
[7] Z. Cai, S. Wu, A. Lu, H. Zhao, Q. Shi, Sci. Technol. Weld. Joint 6 (2001) 84–88.
[8] A. Okada, T. Kasugai, K. Hiraoka, Iron Steel Inst. Jpn. 28 (1988) 876–882.
[9] W. Spraragen, G.E. Claussen, Weld. J. 16 (1937) 4–11.
[10] V. Pavelic, R. Tanbakuchi, O.A. Uyehara, Weld. J. Res. Suppl. 48 (1969) 295–305.
[11] G.W. Krutz, L.J. Segerlind, Weld. J. Res. Suppl. 57 (1978) 211–216.
[12] E. Friedman, Press. Vessel Technol. 97 (1975) 206–213.
[13] O.R. Myhr, O. Grong, Acta Metall. Mater. 38 (1990) 449–460.
[14] Ø. Grong, Metallurgical Modelling of Welding, second ed., Maney Publishing, 1997.
[15] J. Goldak, A. Chakravarti, M. Bibby, Metall. Trans. B 15B (1984) 299–305.
[16] Z. Paley, P.D. Hibbert, Weld. J. Res. Suppl. 54 (1975) 385–392.
[17] O. Westby, T.T.U. Department of Metallurgy and Metals Working, Trondheim, 1968.
[18] H.M. Aarbogh, M. Hamide, H.G. Fjaer, A. Mo, M. Bellet, J. Mater. Process Technol. 210 (2010) 1681–1689.
[19] D. Gery, H. Long, P. Maropoulos, J. Mater. Process Technol. 167 (2005) 393–401.
[20] W. Perret, C. Schwenk, M. Rethmeier, Comp. Mater. Sci. 47 (2010) 1005–1015.
[21] V.D. Fachinotti, A. Cardona, in: A. Cardona, M. Storti, C. Zuppa (Eds.), Mecánica Computacional, San Luis, Argentina, 2008, pp. 1519–1530.
[22] H.G. Fjær, J. Liu, M. M'Hamdi, D. Lindholm, in: H. Cerjak, H.K.D.H. Bhadeshia, E. Kozeschnik (Eds.), Mathematical Modelling of Weld Phenomena 8, Gratz, 2007, pp. 96–99.

Paper V

Effect of Hyperbaric Chamber Gas on Transformation Texture of the API-X70 Pipeline Weld Metal

Amin S. Azar, Erling Østby and Odd M. Akselsen

Metallurgical and Materials Transactions A 43 (9) (2012) 3162-3178.

Effect of Hyperbaric Chamber Gas on Transformation Texture of the API-X70 Pipeline Weld Metal

AMIN S. AZAR, ERLING ØSTBY, and ODD M. AKSELSEN

The development of the texture components in the X70 weld metal under several shielding environments was investigated using the electron-backscattered diffraction (EBSD) and orientation imaging microscopy (OIM) techniques. A new method for assigning the reference direction (RD), transverse direction (TD), and normal direction (ND) was introduced based on the morphological orientation of the grains. The analyses showed that different shielding gases affect the weld metal texture and microstructure. The shielding environment with pure argon shows the highest orientational pole density values and dominant acicular ferrite microstructure. It was observed that the distribution of misorientation angle and special coincidence site lattice (CSL) grain boundaries play significant roles in determining the tensile characteristics of the weld samples. Moreover, the bainite lattice orientation was found dependent on the directional heat flow unlike the other detected constituents.

DOI: 10.1007/s11661-012-1157-x

I. INTRODUCTION

IT is well established that the processing of materials results in the inherent anisotropic crystal orientation. Among the metallic materials, advanced steels show more complicated transformations and strengthening mechanisms during the processing stage. The underlying preferential crystal orientation (namely texture) after the processing stage should be detected along with the affecting parameters to come up with a correct designation and choice of materials.

The effect of mechanical processing (*e.g.*, rolling, drawing, extruding, *etc.*) on the crystallographic texture evolution is reported in several publications.[1] Fusion welding is a process that enhances the directional solidification and phase transformation as a result of the moving heat source and directional thermal gradients.[2] For cubic metals, epitaxial growth occurs when the columnar or dendritic δ-ferrite grains align along the $\langle 100 \rangle$ crystallographic direction of pre-existing substrate grains adjacent to the weld fusion line.[3] The fast growing direction of $\langle 100 \rangle$ was found to deduce dendritic symmetry, although minor, when alloying elements are added.[4] However, for columnar or dendritic solidifications to take place, the kinetics and thermodynamics of the weld pool should be in a certain range; low growth rate (G)-to-temperature gradient (R) fraction results in equiaxed dendrites that is found to be independent of substrate crystal orientation because of the heterogeneous nucleation.[5,6] As a result of different thermal gradients across a single weld pool, there is no governing solidification mode. Along the fusion line, the solidification is controlled by the thermal gradient, which brings about the cellular or columnar growth, while as the weld center line is approached, the solidification undergoes a higher growth rate, resulting in the dendritic or equiaxed solidification modes.[7,8] The solidification phenomenon in the weld pool is also controlled by the cooling rate. Because the constitutional supercooling in the fast-moving, high heat input sources is significantly higher than equilibrium solidification, the dominant growth mechanism is equiaxed dendritic.[9] The solid-state phase transformation is dependent also on the crystal orientation of the prior grains. For instance, as illustrated schematically in Figure 1(a), the relationship of acicular ferrite plates with austenite grains and δ-ferrite is as follows[10]:

$$\{110\}_\alpha \,||\, \{111\}_\gamma \,||\, \{110\}_\delta \quad \text{and} \quad [111]_\alpha \,||\, [110]_\gamma \,||\, [111]_\delta$$

If the orientation of postsolidification weld metal is obtained, then the solidification and growth orientation of the prior phases can be calculated using either the Kurdjumow-Sachs (K-S) or Nishiyama-Wasserman (N-S) orientation relationship[11,12] which is in agreement with the aforementioned orientation description. The K-S relationship shows that the {001} poles can be arranged in eight variant positions for a ferrite phase starting from the (001)[100] position of an austenite grain. Figure 1(b) presents the relationship on the {001} pole figure.

According to Babu and Bhadeshia,[13] the "basket-weave" morphology of acicular ferrite plates can be changed to a nonrandom orientation if elastic stresses are applied during the phase transformation, as in welding where residual stresses are built up gradually in

AMIN S. AZAR, PhD Researcher, is with the Department of Engineering Design and Materials, Norwegian University of Science and Technology, Trondheim, Norway. Contact e-mail: amin.azar@ntnu.no ERLING ØSTBY, Senior Researcher, is with the SINTEF Materials and Chemistry, Trondheim, Norway. ODD M. AKSELSEN, Adjunct Professor with the Norwegian University of Science and Technology, and is also Senior Researcher with the SINTEF Materials and Chemistry.

Manuscript submitted December 6, 2011.
Article published online April 5, 2012

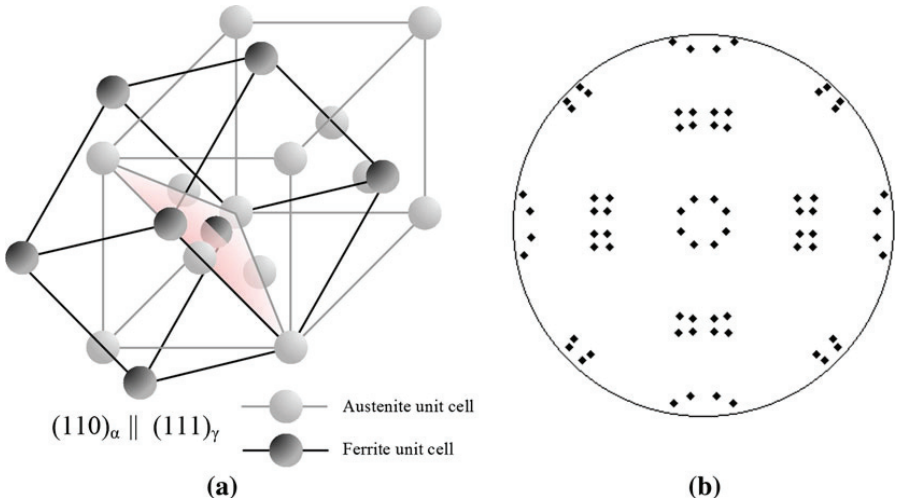

Fig. 1—(*a*) Schematic illustration of austenite to ferrite lattice relationship (*b*) (K-S) relationship on the (001) pole figure.

the elastic range during solidification. Gregg and Bhadeshia[14] discussed that the orientation of the acicular ferrite is very much dependent on both the morphology of the inclusion and the austenite lattice orientation that may decrease the probability of achieving orientation relationship between phases. Hence, the elastic stresses play an important role in the directional formation of the phases.

Shielding gas in gas metal arc welding (GMAW) has a determining effect on the dynamics of the weld pool.[15] The ionization energies of noble gases and dissociation energies of compound gases (*e.g.*, CO_2 and O_2) might bring different weld pool thermodynamics about which in turn affect the microstructure. A higher oxygen potential may result in more inclusions in the molten weld pool that affect the austenite-to-acicular ferrite transformation directly.[3]

The preferred orientation of a crystal lattice is explained by Euler angles for a quantitative description of macroscopic materials.[16] According to the Bunge description,[17] these angles are annotated by (φ_1, Φ, φ_2), in which φ_1, Φ, φ_2 are the angles between the atomic plane normal and the x, y, and z axes, respectively. Copper, S, Brass, and Goss are specified ideal texture components with defined miller indices and Euler angles.[18] In most instances, describing by the ideal components is inadequate, and the texture should be defined using a spread of orientations between two ideal components named "fiber." The detailed definitions of fibers can be found elsewhere.[19]

Ha *et al.*[20] investigated the effect of the welding heat input on the texture evolution of TRIP steel and found that the weld metal shows big grains as the heat input increases. Also, the coincidence site lattice (CSL) number fraction showed some variation in the low and high degrees of fit between the atomic structures of two grains ($\sum$), which is the reciprocal of the ratio of coincidence sites to the total number of sites. They could find no great evolution in the texture as a function of higher heat input. Yu[21] investigated the effect of texture on the crack propagation of the X70 pipeline steel and found that the $\{112\}\langle 110\rangle$ and $\langle 111\rangle$ fibers are improving the tearing resistance of the material despite the presence of M-A constituents. Zhong *et al.*[22] confirmed that the M-A constituent that contributes in the fracture process is dominantly body-centered cubic (bcc) and consists of fewer austenite phases. According to Farrar and Harrison,[23] the bulky type of M-A constituents are formed between acicular ferrite laths as a result of increased carbon content.

Shanmugam *et al.*[24] showed that the bainitic ferrite exhibits a [001] orientation with ferrite matrix, which means that the evolution of acicular ferrite can be traced to the {001} pole figure.

A recent work[25] on the role of crystallographic texture in hydrogen-induced cracking (HIC) of the pipeline steels revealed that the developed fiber components during rolling can decrease the susceptibility to HIC. Venegas *et al.*[26] described the effects, roles, and mechanisms of each fiber component on HIC in detail and determined that the presence of the γ-fiber component along with the low-angle grain boundaries can decrease the susceptibility to HIC. Hutchinson *et al.*[27] showed that the stored rolling energy of the crystallographic planes increases along the α fiber as Φ increases to 90 deg. This finding suggests that the textures with incremented intensity at high Φ angles possess increased internal energy that might be detrimental if stressed directionally.

The high-strength transport pipelines that are laid on the seabed might require reparation occasionally. Because the damaged sites are treated locally, the arc welding operation is an efficient alternative for joining the substituted sections.[28] The objective of this study is to define a region in the weld metal across which the microstructure may reflect the quantitative properties.

The applied survey on different samples using a single approach should be able to sort and describe the basic mechanical properties of the weld metal. Particular emphasis is also given to the methodology of the sample preparation by which multiphase samples can be studied. It is also intended to analyze the evolved microstructure in terms of the texture formation to be able to authenticate the potential mechanical properties. Moreover, once the mechanisms of weld texture and process parameters are known, high-quality joints, which are compatible with the required standards, can be achieved easily. The ultimate goal is to figure out how the mesoscale and the bulk properties of the materials are correlated. An electron-backscattered diffraction (EBSD) investigation will be carried out for several hyperbaric weld samples and the results will be classified.

II. HYPERBARIC WELD SAMPLES AND MATERIALS

The welding operation that is performed under the high ambient pressure is referred as hyperbaric welding.[29] One application is in the subsea pipeline repair and hot-tapping operations. Depending on the depth of operation, the ambient pressure varies; *e.g.*, the deeper the operation depth, the higher the pressure will be. Azar *et al.*[30] reported that as ambient pressure increases, the arc resistance steps up, and therefore, more energy is required to keep the arc on. Near-constant shapes of weld bead cross sections at a high ambient pressure range reveal that although more energy is consumed to maintain the arc, most of this energy is not transferred into the weld pool and the energy loss is higher at increased pressure levels. Nevertheless, the high ambient pressure level results in increased partial pressure of the surrounding gases, which can alter the kinetics and thermodynamics of the weld pool.[31]

Suban and Tušek[32] investigated the effect of different shielding gases on the deposition rate with respect to the physical characteristics of gas mixtures like ionization potential and thermal conductivity. Wang and Tsai[33] reviewed and modeled the effect of surface active elements on the surface tension and Marangoni phenomenon in GMAW. According to Ferrante and Farrar,[34] the amount of high-temperature transformation products (*e.g.*, proeutectoid ferrite and ferrite side plates) increase under elevated oxygen potential provided alongside the protective shielding gas. However, acicular ferrite content is also found to be dependent on the parent austenite grain size, which is controlled by the pinning effect of the inclusions.

In this investigation, five bead-on-plate weld samples were prepared using GMAW based on a short-circuiting frequency of 125 Hz (8 ms periods). The base metal is an API-X70 pipeline steel and the welding wire is 1.0 mm ESAB-HBQ core weld fed continuously at the speed of 135.0 mm/s, tailor-made for the hyperbaric operation. The chemical compositions of the base metal and filler wire are given in Table I. The welding speed was set to 7.0 mm/s. The torch standoff was 10 mm at the ambient pressure level of 10 bar for all five samples. The chamber was prepressurized and depressurized several times using 99.98 pct pure argon gas to reduce the partial pressure of the environmental oxygen. The chamber gases used for simulating the subsea condition as well as the average welding voltage and current are reported in Table II for each sample.

The selection of such a specific subsea pipeline grade depends on the requirements and design considerations as well as wall thickness and cost. Lower grades of API gain their strength by carbon-manganese constituents in normalized condition, whereas the higher grades are strengthened by microalloying the elements as well as the controlled thermomechanical operation succeeded by quenching and tempering. In API-X70, the carbon content has been lowered and more microalloying elements were added. Thus, the weld microstructure of these types is generally bainitic depending on the cooling rate.

III. SAMPLE PREPARATION AND ELECTRON BACK-SCATTER DIFFRACTION

Haldar *et al.*[1] cut the weld samples in a transverse section, *e.g.*, section *A* in Figure 2. Although it covers the phase evolutions across the weld bead, the morphological orientation of grains in weld metal can be mistreated. As depicted in Figure 3, the grains grow in a

Table II. Weld samples and Corresponding Average Current and Voltage Data

Sample	Chamber Gas	Average Current (A)	Average Voltage (V)	I·V (VA)
S1	Ar	229.84	23.96	5506.16
S2	He	211.82	27.54	5834.17
S3	CO_2	187.68	33.46	6279.23
S4	50 pct Ar-50 pct He	223.28	24.90	5560.2
S5	50 pct He-50 pct CO_2	217.97	26.13	5694.85

Table I. Chemical Composition of X70 and HBQ Filler Wire

		Chemical Composition (wt pct)										
		C	Si	Mn	P	Ni	Cr	Mo	Cu	V	Ti	O_2
X70	maximum	0.08	0.28	1.85	0.015	0.31	0.1	0.06	0.3	0.01	0.02	—
	minimum	0.04	0.05	1.5	0.008	0.11	0.05	0.04	0.1	—	0.006	—
HBQ		0.04	0.5	1.3	—	0.5	—	—	—	—	0.02	600 ppm

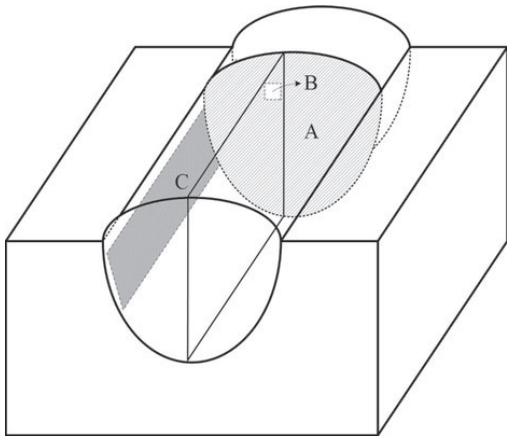

Fig. 2—Different sample sections for EBSD investigation.

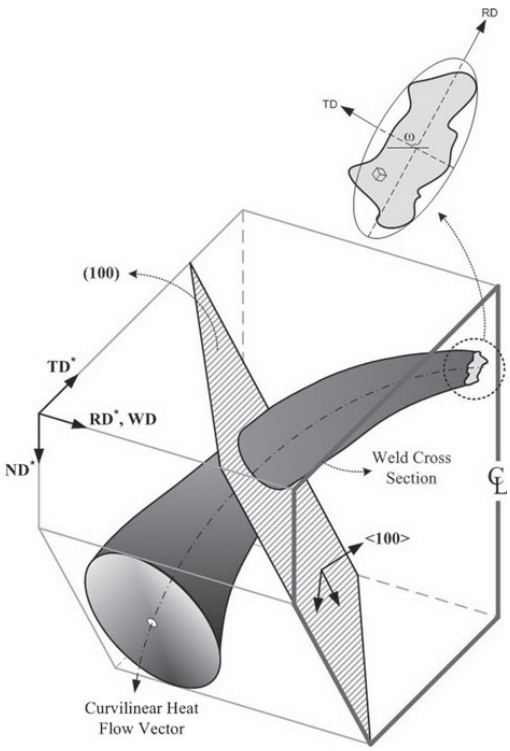

Fig. 3—Schematic illustration of 3-D grain morphology in arc welding.

three-dimensional order. Cutting the weld metal into two-dimensional slices causes orientation variation with respect to the preferred ⟨100⟩ growth direction. The heat flow in fast-moving arc welds follows a curvilinear path[35,36] that changes the relative orientation of fast growth plane with respect to the defined sample orientation (reference direction [RD*], transverse direction [TD*], and normal direction [ND*]) if cut in different positions. As a result, the choice of unique reference coordination system across the weld bead becomes inconvincible.

The weld samples can be cut in several sections, depending on the research interests. However, each section might have advantages and disadvantages of its own. Kluken *et al.*[10] prepared the samples on a slant section along the welding direction (WD) similar to section *C* in Figure 2. It was more toward the weld center line rather than the fusion line. Such preparation may not exhibit a unique solidification mode because it may vary from fusion line to center line. It is also possible to section very close to the fusion line, *e.g.*, section *C* in Figure 2 to ensure cutting through a uniform solidification mode. However, determining section *C* for irregular weld bead shapes is sometimes impossible. Svensson[3] described that such a section is free of weld metal morphological orientations.

In this study, the weld samples were prepared based on section *A* in Figure 2. To come over the presence of multiple morphological orientations of solidified grains, a limited area close to the weld centerline was chosen in all the samples (section *B* in Figure 2). The choice of sample orientation directions will be described in Section IV.

The samples were mounted in a conductive resin and automatically ground and polished down to a very fine surface finish. To remove the deformation layer on the surface, 10 minutes of colloidal silica suspension polishing with pH of 9.8 and particle size of approximately 0.04 μm was used.

The EBSD patterns were collected using Zeiss Supra 55 VP, low vacuum field emission gun scanning electron microscope (Carl Zeiss, Oberkochen, Germany). The EBSD detector (NORDIF UF750, Trondheim, Norway) can record at most 30 online patterns per second. The working distance was set to 20 mm with the tilt angle of 70 deg under a high-current electron beam. The accelerating voltage of the gun was adjusted to 20 kV.

Davut and Zaefferer[37] studied the effect of EBSD data points resolution over a certain area on the statistical reliability of phase fraction determination and defined a criterion below which the detected phase content was unreliable. The chosen 1-μm step size is based on the aforementioned criterion, meeting the statistical requirements.

IV. DETERMINATION OF SAMPLE REFERENCE ORIENTATION

To establish a relationship between the grain morphology and crystallographic orientation of the grains, the reference coordination system of each sample was selected based on the grain shape orientation. Grain shape is determined by fitting an ellipse to the points making up a grain as shown in Figure 4. The grain shape orientation is defined by the angle (ω) between the major axis of an ellipse fit to a grain and the horizontal

direction. The least-squares approach, adapted from Biggin and Dingley[38] for locating the X-ray source point in Kossel diffraction, was used to determine the shape orientation of entire grains on the covered area.

It can be observed from Figure 4 that the ω angle shows two peaks at approximately 26 deg and 116 deg for all five samples. It implies that most grains are elongated in these two directions that have the orientation difference of approximately 90 deg. The RD can be assigned along the grains that are representing a greater number fraction. Some satellites around the main peaks that also show 90 deg of angular difference. Because the shapes are exhibiting a 90 deg symmetry with respect to ω, their position with reference to RD and ND are constant.

The entire local crystallographic directions can be rotated based on the previously mentioned procedure after EBSD data acquisition. In this case, the dataset from different samples can be compared.

V. EBSD STUDY OF THE SAMPLES

A. *Base Metal (BM) and Heat-Affected Zone (HAZ)*

Figure 5 shows the evolution and distribution of bcc phase subgrains in the rolled substrate material based on the Bunge convention. Copper (green), S (blue), Brass (yellow), and Goss (red) components of β-fiber texture and their orientation concentration on pole figure and

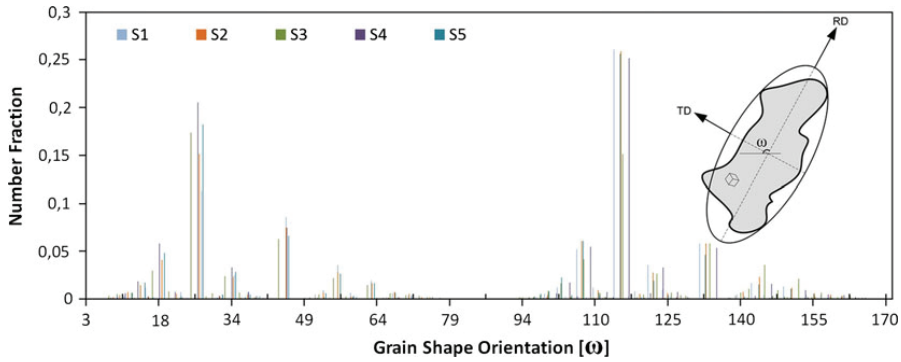

Fig. 4—Grain shape orientation and sample reference coordination system.

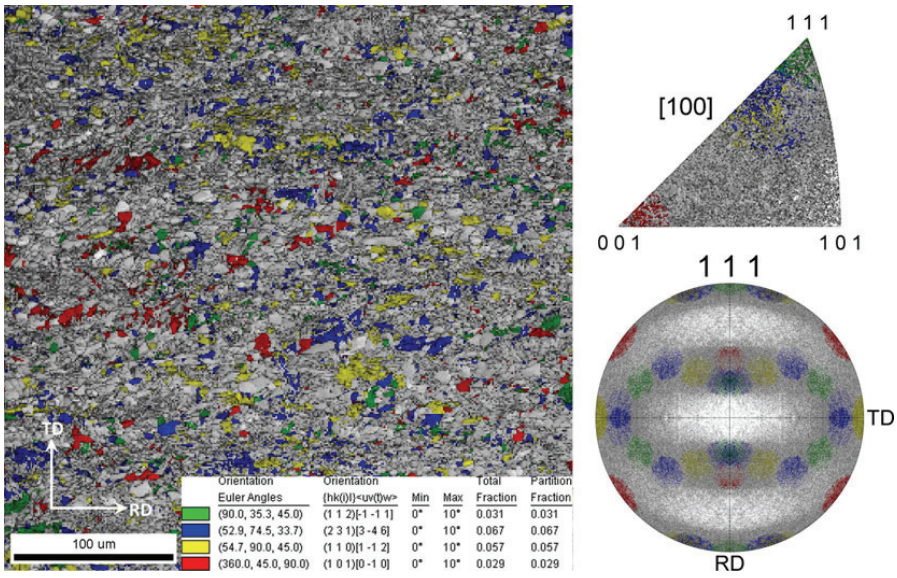

Fig. 5—β-fiber texture components of BM (Color figure online).

inverse pole figure are presented. Figure 6 shows the location of β-fiber components on the orientation density function (ODF) space.

Figure 7 shows the inverse pole figure mapping of the grains across the HAZ. Toward the left-hand side of the figure grains are larger than those at upper right corner that is the prepresentative of grain growth and partially transformed regions, respectively.

Figure 8 shows the (100), (111), and (110) pole figures for both BM and HAZ. In general, the pole figures of HAZ are decomposed versions of BM pole figures because of solid-state transformation. The location of high-intensity peaks on the (111) plane pole figures remained essentially unchanged; however, new intensity peaks emerge mostly along the TD. The overall intensity shows lower values in HAZ compared with those of BM, which is presenting the effect of thermal cycles on texture decomposition of the material. Maximum density components in the (100) and (111) pole figures of HAZ are approaching similar texture directions if the materials are exposed to such a thermal history.

Figure 9 depicts the [100] inverse pole figure (IPF) mapping of the material at BM and HAZ. It can be observed that the density contours around (111) has almost remained in position while (001) is suppressed in HAZ. In addition, high-CSL boundaries and planes like (114), (115), and (103) were developed in HAZ.

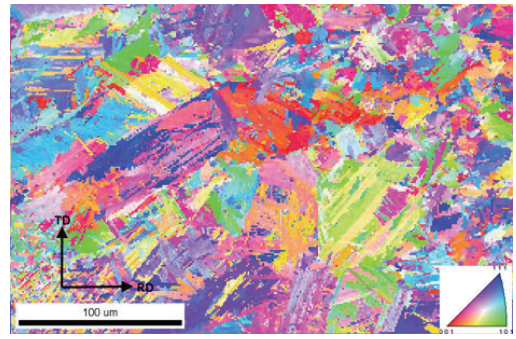

Fig. 7—IPF image of HAZ.

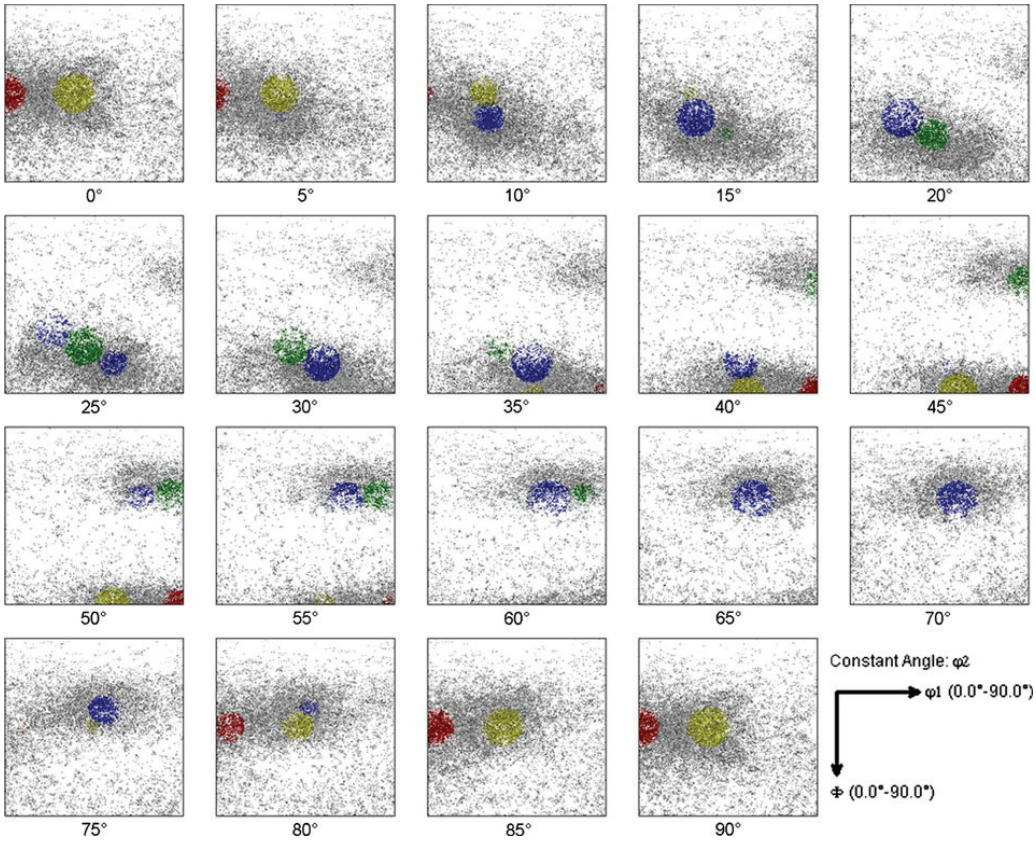

Fig. 6—ODF mapping of β-fiber components in BM.

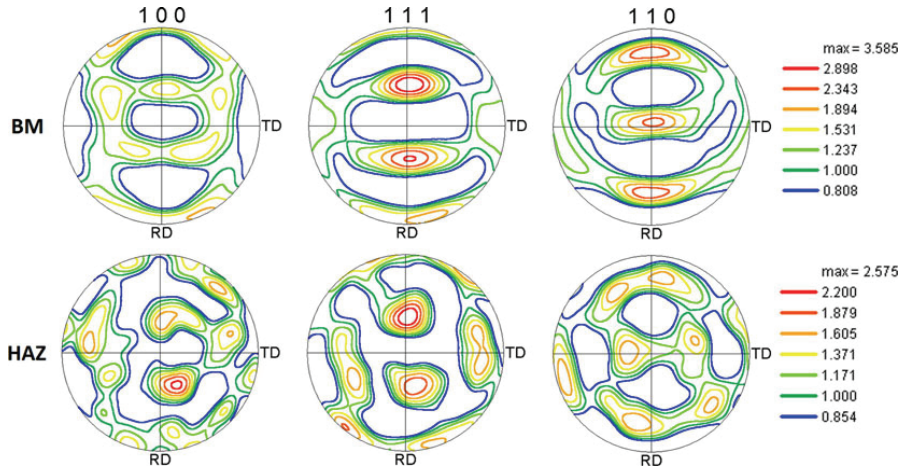

Fig. 8—(100), (111), and (110) pole figures of rolled BM and HAZ.

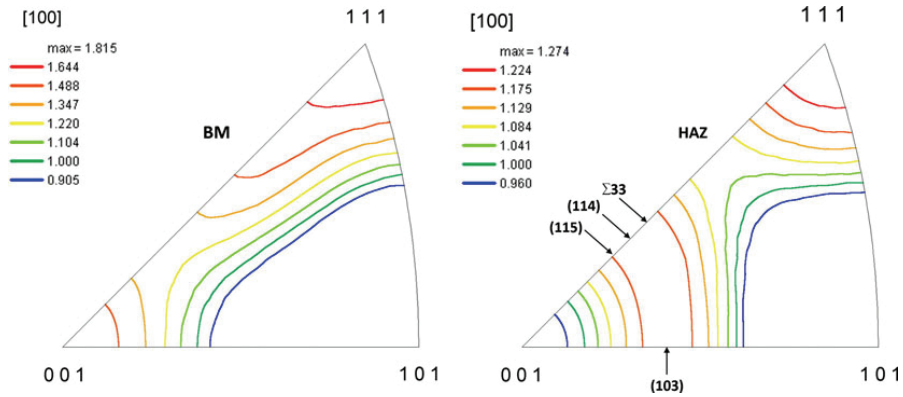

Fig. 9—[100] inverse pole figure of BM and HAZ.

B. *S1 Sample*

The lowest welding arc power is recorded for this sample. Argon is the most conventional shielding gas in hyperbaric welding technology. It is known for its effective weld pool protection and ultimate weld properties. However, spattering problem exists specially at high pressure levels, which makes this gas a poor candidate for long-term operations. Figure 10 shows the IPF image of this sample. Figure 11 illustrates the (100), (111), and (110) pole figures, [100] IPF as well as ODF mapping. On the (100) pole figure, the sample direction shows a strong component close to RD, and on the (110) pole figure, the strongest component is aligned close to ND. IPF mapping depicts strong intensities at (111) and (001) planes on the [100] reference crystal coordinate frame, which represents plane alignment parallel to [100] direction. Thus, the conditions of preferred directional growth are met in this weld sample. β-fiber texture components were detected on the ODF, however, showing low intensities across the φ_2 angle (Figure 26). Additionally, η fiber shows an intensity peak at approximately 30 deg to 40 deg on Φ. ε and τ-fibers in this specimen show shifted peak intensities toward the lower Φ angle.

C. *S2 Sample*

The dominant microstructural constituent of this sample is very similar to S1. However, prior austenite grain morphology was found longer and narrower compared with the S1 sample. This phenomenon leads to diverse orientational directions that result in more pole locations on the pole figures and decreased texture component densities. Figure 12 shows the IPF image of the S2 sample and Figure 13 illustrates the pole figures, IPF, and ODF maps of S2. The high-intensity component

of the (100) pole figure is not along the RD like in the case of S1. Nevertheless, the high-intensity components of (111) and (110) are still comparable with the S1 pole figures (*e.g.*, rotated around the ND). In addition, the IPF mapping shows that the (001) planes are not aligned to the [001] crystal coordinate orientation as in the S1 sample. It shows that the preferred growth direction is suppressed partially under such conditions. The (111) planes are

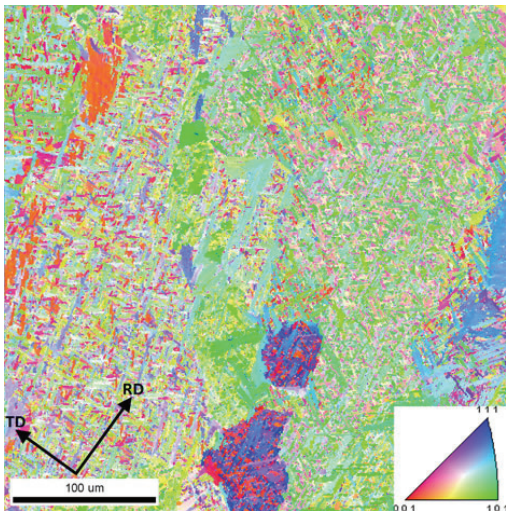

Fig. 10—IPF image of S1 sample.

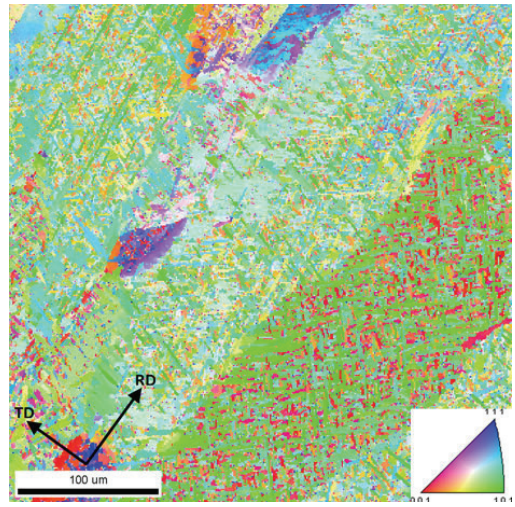

Fig. 12—IPF image of S2 sample.

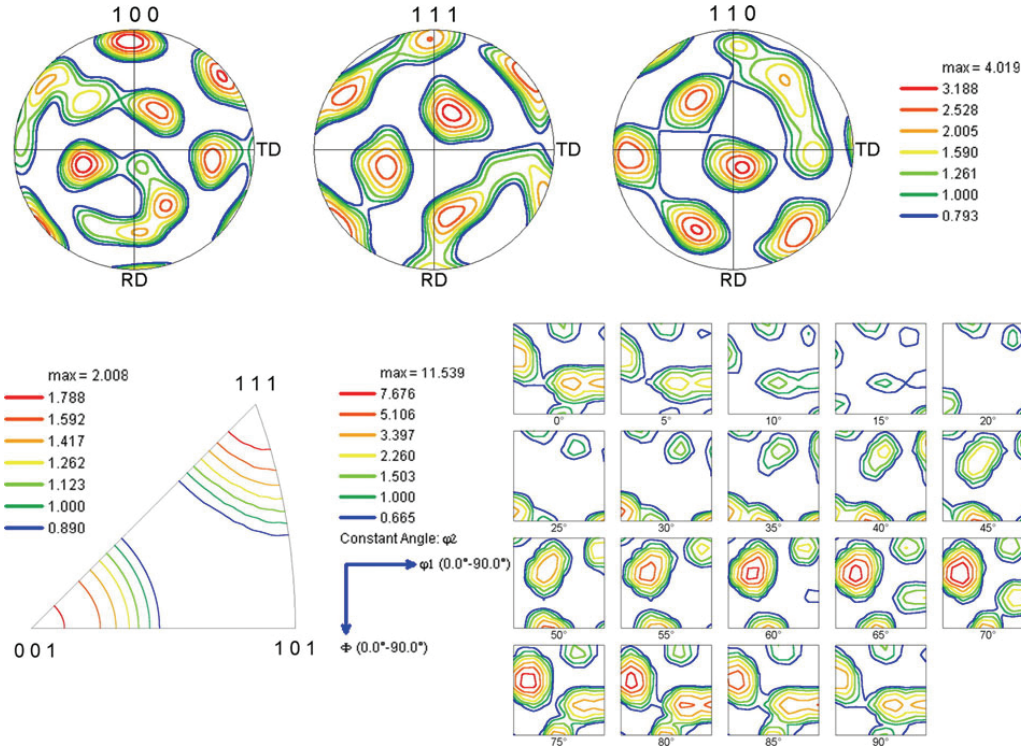

Fig. 11—Pole figures, [001] inverse pole figure, and ODF of S1 sample.

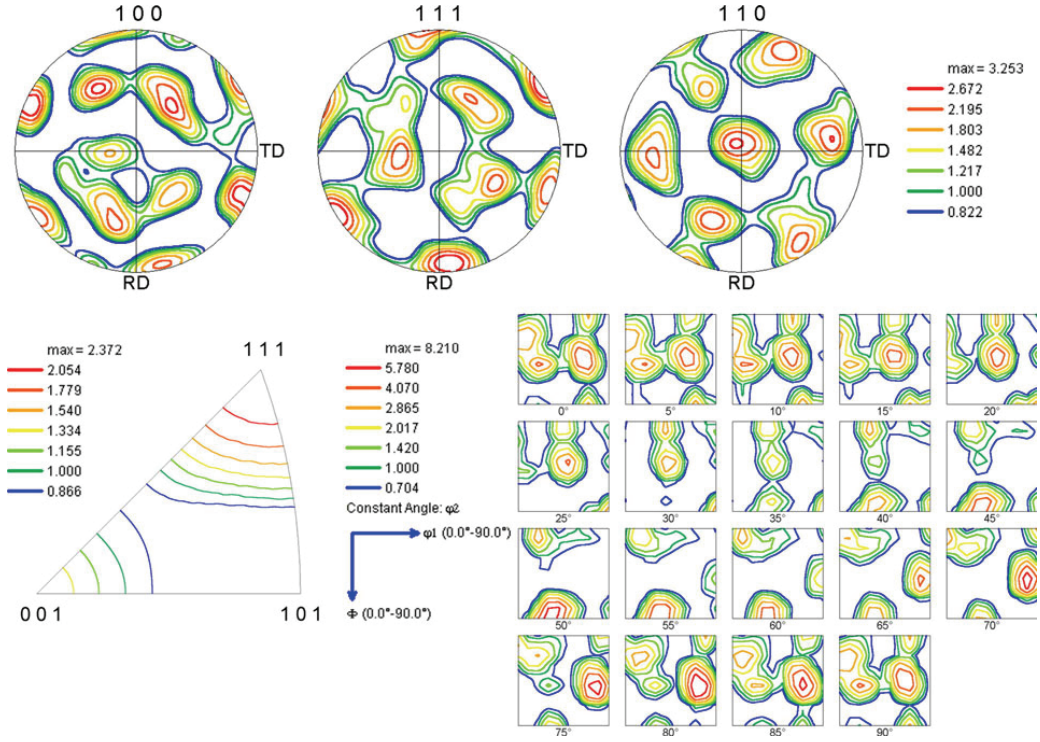

Fig. 13—Pole figures, [001] inverse pole figure, and ODF of S2 sample.

aligned toward the [001] crystal orientation, which is similar to S1.

ODF shows intensities along the β-fiber only at a high φ_2 angle range (approximately 80 deg to 90 deg). High intensities were also observed on an α-face-centered cubic (fcc) fiber along the φ_1 angle at approximately 60 deg to 70 deg.

D. *S3 Sample*

Excessive oxygen potential in this sample leads to more dispersed oxide inclusions that pinned the boundaries of prior austenite and limited the grain growth. Consequently, the small austenite grains are not transformed into acicular ferrite. The dominant microstructure of this sample is polygonal ferrite and some lower bainite phases. Figure 14 shows the IPF image of S3 sample. Coarse polygonal ferrite grains of approximately 50 to 80 μm are observed in this image. Figure 15 presents the PFs, IPF, and ODF of S3. The pole figures, in contrast, show a rotated version of texture components on the (111) and (110) planes when compared with the S1 and S2 samples. Components parallel to the TD are intensified in this sample in contrast to S1 in which components were aligned mostly parallel to the RD. The IPF of S3 sample shows a very similar distribution as depicted in the IPF of HAZ except that the density of the (111) planes (residues of rolling texture) is suppressed. Consequently, the CSL boundaries in HAZ and S3 may represent some

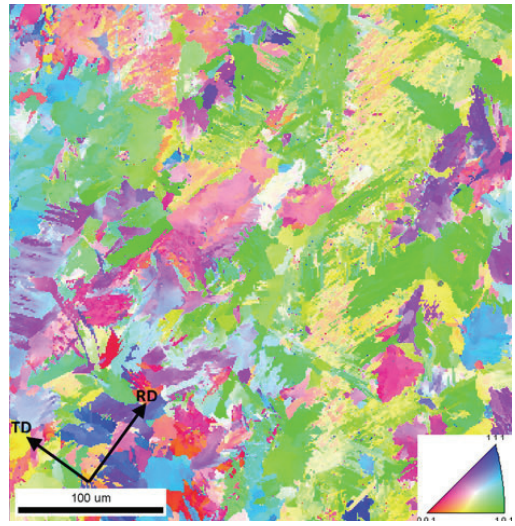

Fig. 14—IPF image of S3 sample.

resemblance (see Section VII). The intensity of β-fiber is not constant in this sample, although it lies over the β-fiber intensity of S1 and S2 samples. This sample shows high α-fcc and α-fiber intensity peaks as presented in Figure 26.

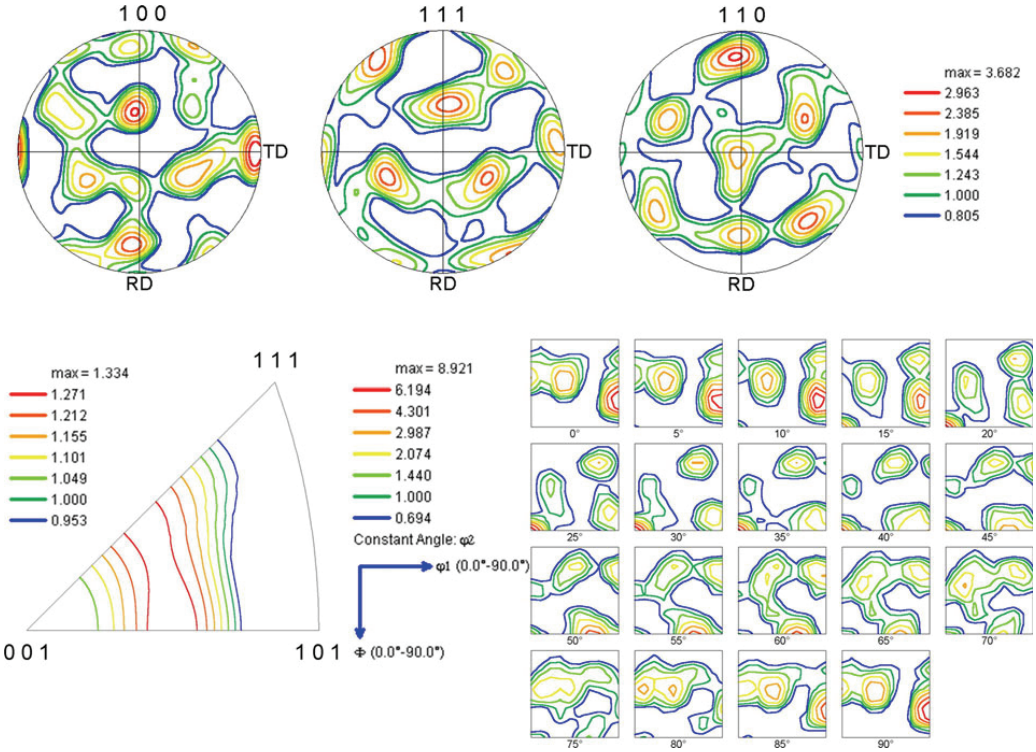

Fig. 15—Pole figures, [001] inverse pole figure, and ODF of S3 sample.

E. *S4 Sample*

The presence of thin ferrite grain boundary layers is the only difference between the microstructures of S4 and S1 (or S2) samples. Figure 16 shows the IPF image of S4. The length to width proportion of prior austenite grains is between that of S1 and S2 sample. Figure 17 illustrates PFs, IPF, and ODF of S4. The arrangement of high-intensity components on the (100), (111), and (110) pole figures seems incomparable with the previous samples. In terms of ODF times random, it shows higher component intensities compared with the S2 sample, although it is lower than the S1 sample. IPF shows improved distribution around (001) and (111) as well as some other planes with indices close to (323), (959), and (747). This sample shows a strong β-fiber texture especially in the lower φ_2 range. In addition, a short peak can be observed at approximately 55 deg of Φ along the η-fiber (see Figure 26).

F. *S5 Sample*

Figure 18 shows the IPF image of S5. Upper bainite was found as the main constituent of this sample. A smaller proportion of lower bainite, acicular ferrite, and even polygonal ferrite were also observed in this sample. Figure 19 presents the PFs, IPF, and ODF of S5. The

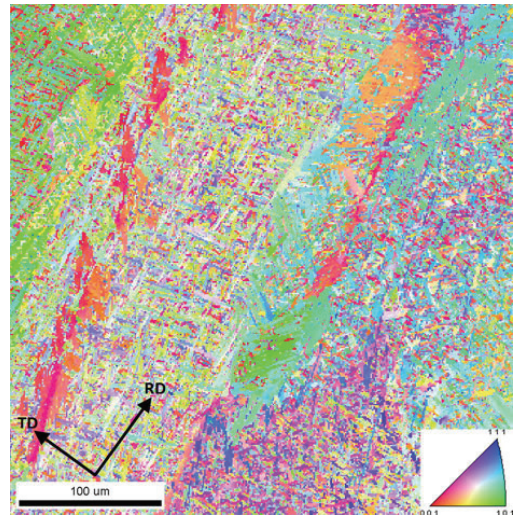

Fig. 16—IPF image of S4 sample.

(100) pole figure shows a high-intensity peak at approximately 30 deg away from the TD. ODF demonstrates intensive texture components higher than other samples

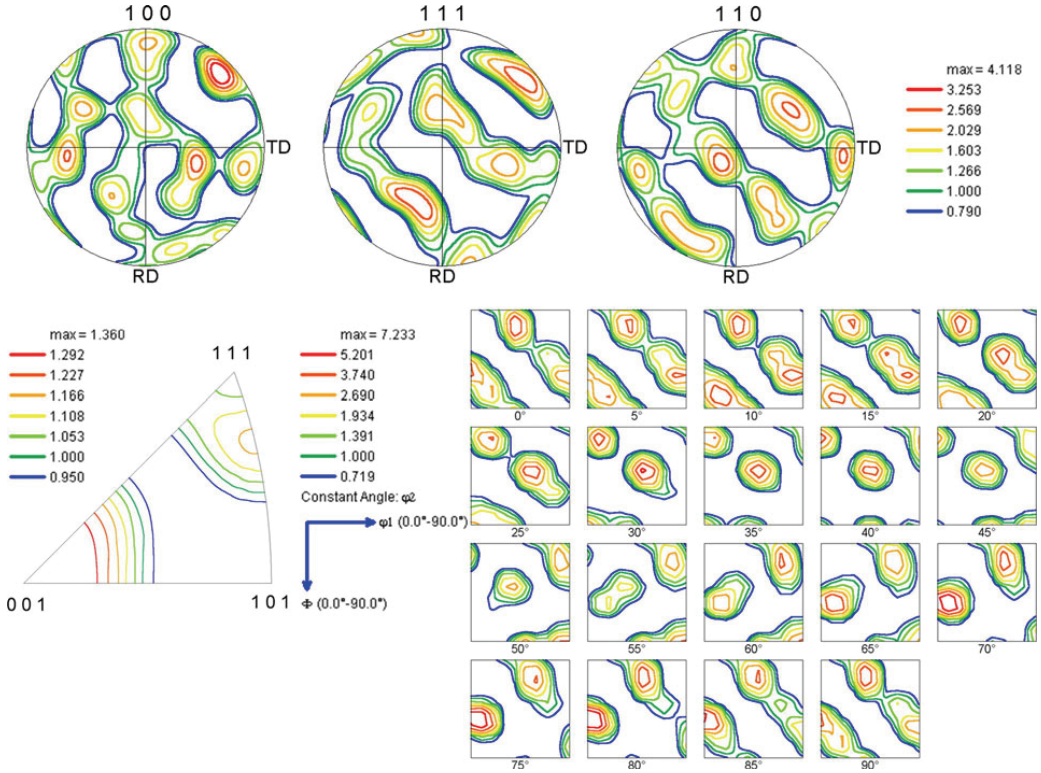

Fig. 17—Pole figures, [001] inverse pole figure, and ODF of S4 sample.

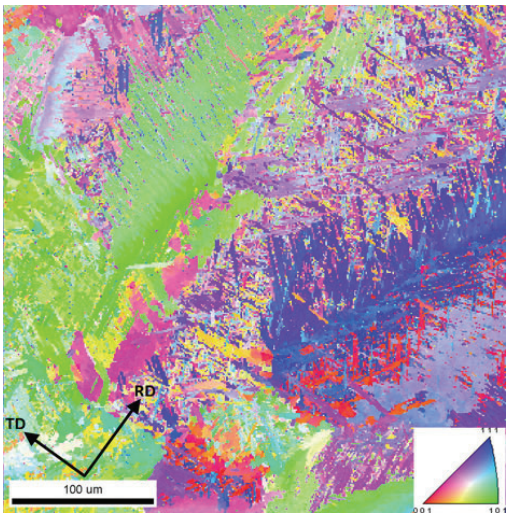

Fig. 18—IPF image of S5 sample.

except S1. It verifies that the growth and transformation of bainite phase is more textured than other observed microstructures. IPF shows the highest intensity around (001), which reveals the effect of the heat flow direction on the bainite transformation of this sample. A low intensity level was found on β-fiber except at low φ_2 values. High intensity was observed on the γ fiber at approximately 30 deg to 70 deg. The high γ-fiber distribution level between [111]⟨110⟩ and [111]⟨112⟩, which corresponds to 60 deg to 90 deg of φ_1, is representing high energy grain boundaries.[39] This fact is possibly the reason for providing a driving force in bainite phase nucleation.

Figure 20 presents the number fraction of the most prominent CSL grain boundaries in bainite and acicular ferrite microstructures of S5 sample. Since the upper bainite constituents are large, the embedded grain boundary length is consequently shorter than that of the acicular ferrite. As a result, the measured number fraction of different CSL boundaries in the bainite structure shows lower values. It can be observed that the number fractions of different CSL boundaries in bainite remain below the acicular ferrite values except in the Σ17b case where bainite shows higher. The Σ25b and Σ33c types of grain boundaries can be associated with the acicular ferrite transformation. According to Brandon[40] and Wolf and Yip[41] the dislocation density has an inverse relationship with the Σ value. It infers that the lower the Σ value, the higher the dislocations density will be. However, these boundaries possess low energy and high mobility characteristics.

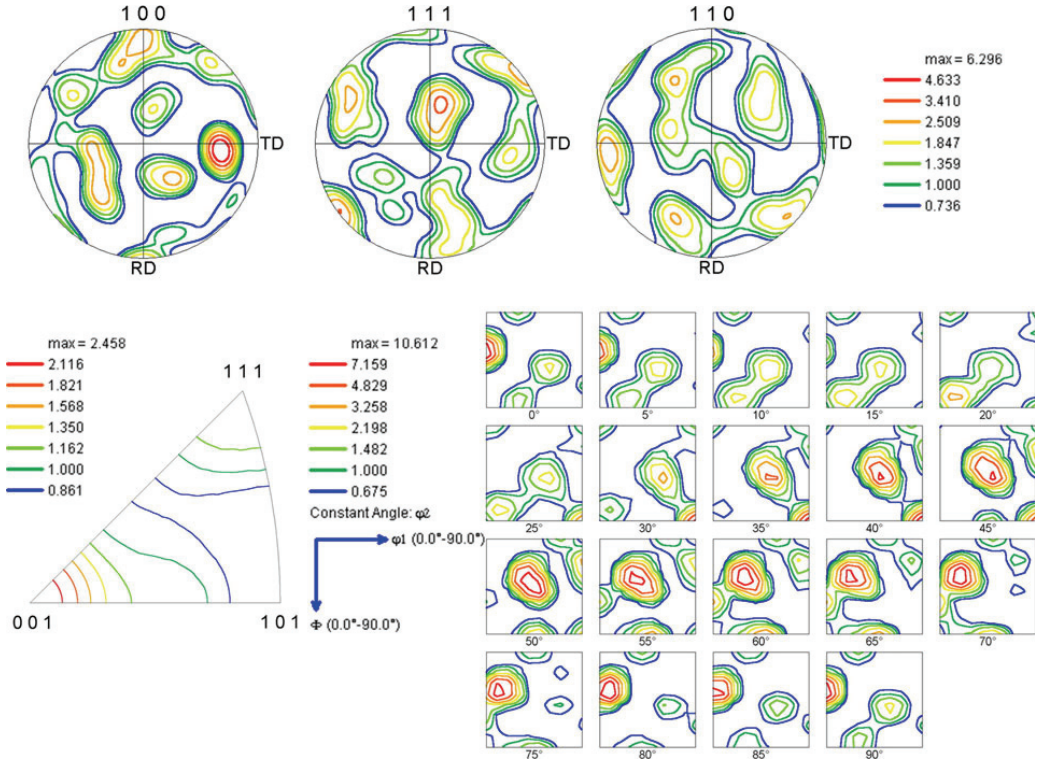

Fig. 19—Pole figures, [001] inverse pole figure, and ODF of S5 sample.

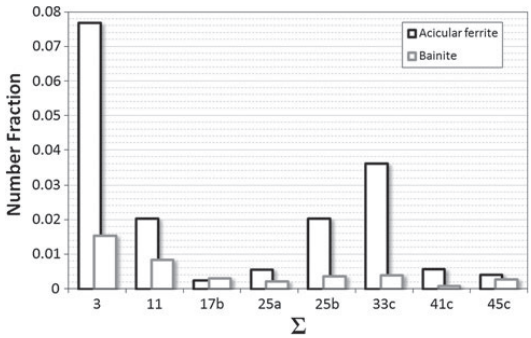

Fig. 20—Comparison of the most pronounced CSL grain boundaries between bainite and acicular ferrite microstructures of S5 sample.

VI. PHASE TRANSFORMATION

Patches of same microstructural constituents, mainly located in a single prior austenite grain, were investigated in terms of their transformation texture. It was found that the acicular ferrite transformation in the S1, S2, and S4 samples was following the K-S orientation relationship. The poles were arranged in all eight possible variant locations explained by the K-S relationship. Figure 21 shows several patches on the S1 sample, and their corresponding developed texture are presented in Figure 22. The center of each circular shape zones (Bain zones in red) represents one of three prior

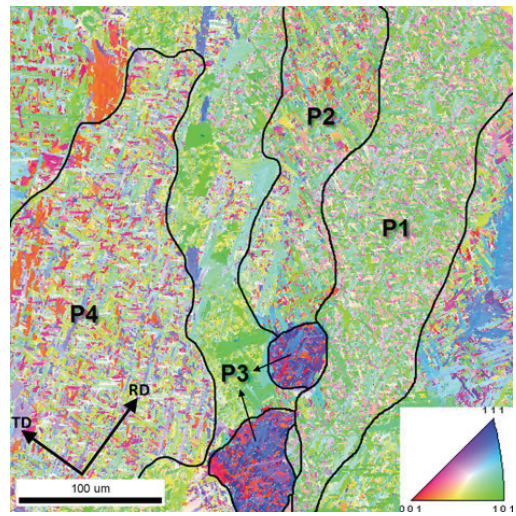

Fig. 21—Selected patches in S1 sample.

austenite orientation poles.[42] Adjacent patches show different prior austenite pole locations that represent the fact that the austenite grains were solidified in an equiaxed mode. Moreover, bainite patches were observed to follow the K-S relationship. It was found that the texture intensity values of ODF sections are as high as 30 times random for the orientations inside the patches.

VII. OVERALL COMPARISON

The intention of this section is to compare different microstructural features in different samples beside the BM and HAZ. Screening and sorting these features as well as considering the actual mechanical properties is beneficial in terms of understanding the effect of different shielding gases on the microstructure. In addition, this process works as a guideline in materials selection.

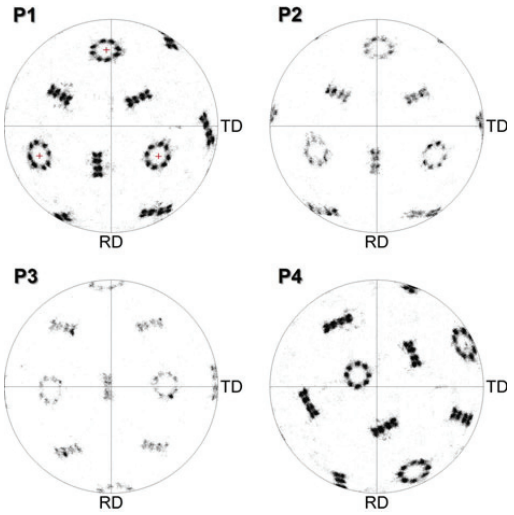

Fig. 22—(100) pole figures of different acicular ferrite patches.

Figure 23 illustrates the number fraction of the correlated (*i.e.*, grain boundaries in the microstructure) and uncorrelated (*i.e.*, random orientation pairs) misorientation distributions.[43] The correlated distribution shows two peaks at approximately 52.5 deg ± 0.3 deg and 59.5 deg ± 0.8 deg apart from the peaks at the low misorientation angle region. Sample S3, for instance, shows a very high fraction around the low-angle region compared with the high misorientation angles. The S1, S2, and S4 samples show very similar distributions with respect to the correlated distribution both at high and low misorientation angles. However, in the uncorrelated misorientation distribution figure, the S1 sample lies above the S2 and S4 samples. The S5 sample shows large number fraction values at both low and high uncorrelated misorientation angles.

Keehan *et al.*[44] found that the bainite transformation associates mainly with either very low or very high misorientation angles. The orientation difference within a bainite packet (coalesced bainite or lower bainite) is essentially of the low-angle type, whereas the orientation difference between the two adjacent packets is high. Because of the dominant bainitic microstructure, the medium-range misorientation angles are suppressed in the S5 sample.

Figure 24(a) shows the misorientation angle as a function of the grain boundary length normalized by the area being investigated. It shows how the different grain boundaries are distributed at different misorientation angles. Because the grain boundary length is correlated with the grain size, this figure vaguely represents the grain size of the different samples; the higher the GB length, the smaller the grains. The S1 sample shows the highest length at a high misorientation angle, even though it possesses the highest length at a low misorientation angle. The S4 sample shows the maximum difference in grain boundary length in low and high misorientation angles. Because the high-angle misorientation results in high-energy grain boundaries that are barriers in failure mechanisms, the longer grain boundary length at a high misorientation angle is desirable. Figure 24(b) illustrates the tensile properties of the weld samples. Very small-sized samples were prepared along the single-pass weld bead that consists only of the weld

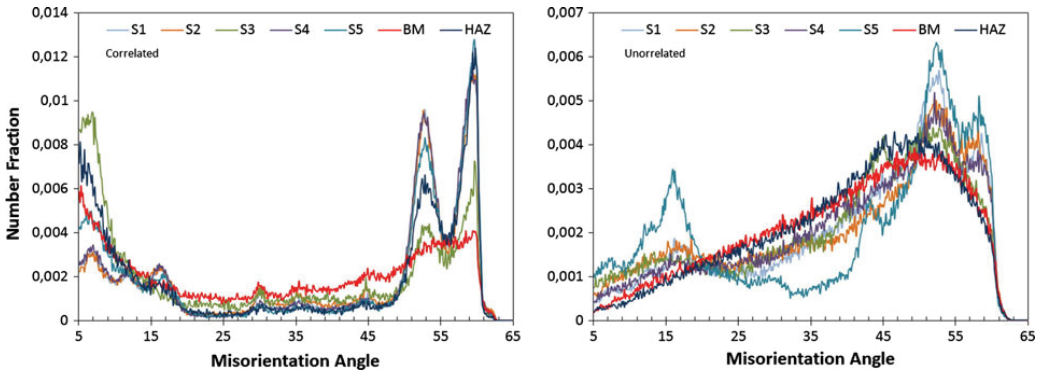

Fig. 23—Correlated and uncorrelated misorientation distributions.

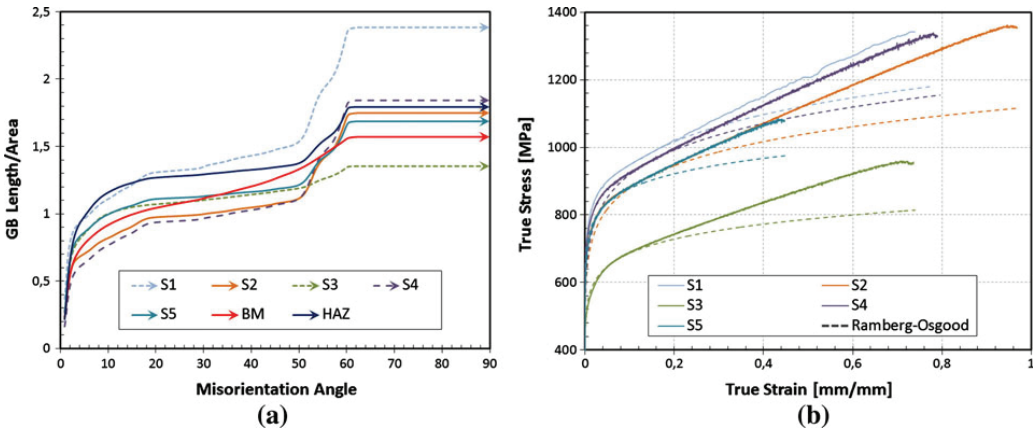

Fig. 24—(*a*) Grain boundary length *vs* misorientation angle. (*b*) Tensile properties of different samples.

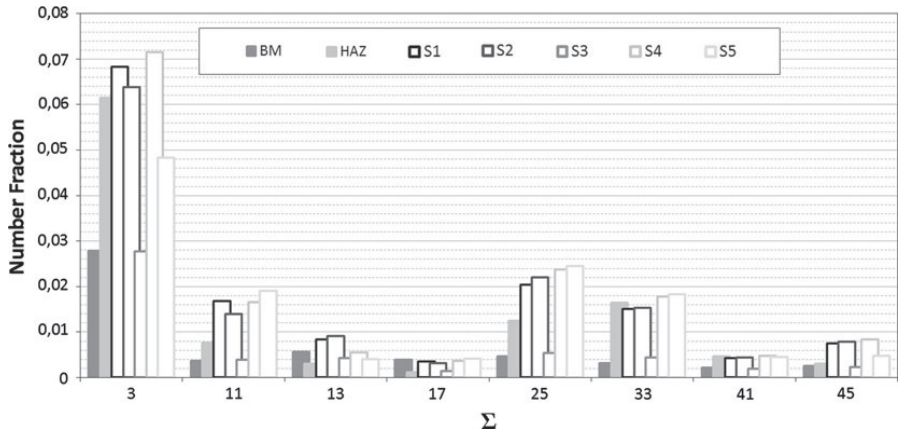

Fig. 25—CSL grain boundary formation in different samples.

metal microstructure. The thick lines show the actual true stress–strain curve and the broken lines with the same color are Ramberg-Osgood curves corrected for necking according to Bridgman.[45] It was observed that for a given true strain, the stress levels of the samples follow the same arrangement as the grain boundary length at a high misorientation angle.

Figure 25 depicts the distribution of CLS grain boundaries in the investigated samples. The S5 sample exhibits a high number fraction of high Σ grain boundaries (*e.g.*, Σ25 and Σ33) and a relatively low number fraction of low-angle grain boundaries (*e.g.*, Σ3). It implies that the fraction of dislocation-free grain boundaries in this sample is relatively high. Fewer dislocations may result in a lower strain at fracture as a result of their contribution in plastic deformation mechanisms (Figure 24). Sample S3 shows a very low Σ3 value; yet the high Σ grain boundaries show a low number fraction, respectively, which is representative of a short grain boundary length in general.

Figure 26 depicts the evolution of texture fibers in different samples. The detailed descriptions of texture fibers were presented in Section V for each sample. It should be noted that the same harmonic series parameters were employed for all the samples to keep the "ODF times random" values comparable.

VIII. DISCUSSION

The effect of grain boundaries on tensile data was presented as one of the influential aspects of choosing an appropriate shielding environment. Apart from the effect of the morphology of particles and the mechanisms of fracture involved in the mechanical characteristics, some materials behavior can be traced to the texture and grain boundary engineering criteria. For instance, according to the Hall-Petch definition of grain boundary strengthening,[46] high grain boundary length, especially the high-angle boundaries, impede the

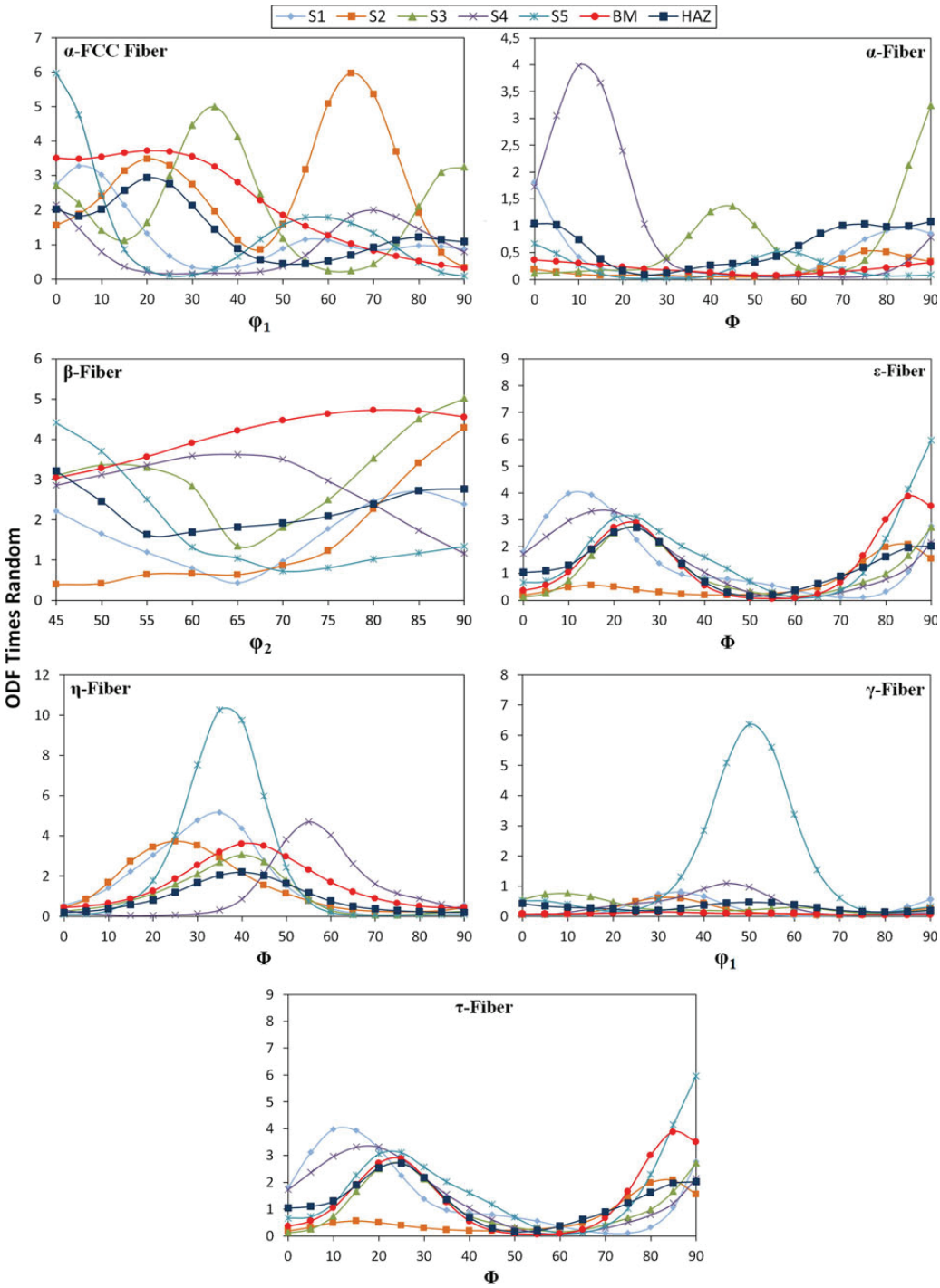

Fig. 26—Evolution of different texture fibers in the weld samples.

dislocation movement from grain to grain and results in a higher yield strength.

In this study, the S1 sample is the most textured one among the others. However, the S5 sample, for instance, shows several orders of magnitude of ODF times random compared with the others at some known textures components like η and γ fibers. Hutchinson[47] reported a strong correlation between the grain boundary microstructures and γ-fiber formation, as in the S5 case where the microstructure is mostly bainite. Because the bainite patches are large, the overall grain boundary length was reduced, yet, the proportion of special CSL grain boundaries changed significantly. One the one hand, the analysis of all samples for their average elastic stiffness in terms of the crystal orientations and applied stress direction (parallel to ND in tensile experiments) showed that the development of textured bainite constituents increases the elastic stiffness. Grain boundary characteristics, on the other hand, confines the plastic deformation in S5 sample and results in limited plasticity.

The η-fiber texture shows the variation in the orientation function for all planes and $\langle 001 \rangle$ parallel to the reference direction. Hence, it reveals that the growth of bainite constituents consistently follows the characteristic heat flow in welding.

As expected, the β-fiber texture component decomposes in all the samples compared with the BM sample. The trend of β-fiber distribution along φ_2 is very similar for BM and HAZ samples, which confirm the aforementioned behavior of HAZ under such heating condition (Section V–A).

The choice of the area being investigated requires more experiments; nevertheless, the presented area in this study unveiled a significant relationship between the tensile properties and the microstructural characteristics. The selected sections superimpose the region in tensile specimen where the ductile fracture mechanisms initiate. This region may be the weakest link involved in the fracture processes with respect to the surrounding microstructure.

IX. SUMMARY

This study shows that the hyperbaric chamber gas not only affects the microstructure but also alters the texture properties of the weld metal. The following conclusions can be drawn from this investigation:

- A positive relationship was found between the grain boundary engineering and the arrangement of the tensile stresses in different weld samples. The length of overall grain boundary as well as special CSL boundaries are determinant in tensile properties.
- The evolution of austenite grain orientations near the weld center line does not follow the heat gradient.
- The heat flow direction influences the morphology and lattice orientation of the bainite constituents nucleated from the grain boundary. The development of η-fiber confirms this phenomenon.
- A combination of low and high misorientation angles as well as low-to-high CSL boundaries number fraction determine the dislocation density and plastic behavior of the weld samples.

X. FUTURE WORK

An EBSD study should be carried out with the same systematic procedure on different areas to identify the significance of the introduced region. Complementary tests are needed to identify the effect of the observed textures and fibers on the overall mechanical properties of the weld metal. A high-magnification mapping is also required to distinguish the evolution of CSL grain boundaries between two adjacent phases, and the results should be correlated to the welding parameters. Understanding the effect of misorientation angle distribution between the grains entails more investigation.

ACKNOWLEDGMENTS

The financial support from the Norwegian Research Council (Contract No. 192967/S60), Statoil, Gassco, Technip, and EFD Induction is gratefully acknowledged. The authors would like to thank Mr. Wilhelm Dall and Mr. Yingda Yu for their valuable guidelines.

REFERENCES

1. A. Haldar, S. Suwas, and D. Bhattacharjee: *Microstructure and Texture in Steels and Other Materials*, Springer, Jamshedpur, India, 2009.
2. S. Kou: *Welding Metallurgy*, 2nd ed., Wiley, New York, NY, 1987.
3. L.E. Svensson: *Control of Microstructures and Properties in Steel ARC Welds*, CRC Press, Boca Raton, FL, 1994.
4. W.W. Mullins and R.F. Sekerka: *Appl. Phys.*, 1963, vol. 34, pp. 323–29.
5. K.A. Jackson: *Solidification*, ASM, Materials Park, OH, pp. 121–50.
6. D.M. Herlach: *Mater. Sci. Eng.: R: Reports*, 1994, vol. 12 (4,5), pp. 177–272.
7. M. Rappaz, S.A. David, J.M. Vitek, and L.A. Boatner: *Metall. Trans. A*, 1989, vol. 20A, pp. 1125–38.
8. T. Zacharia, J.M. Vitek, A.J. Goldak, T. DebRoy, M. Rappaz, and H.K.D.H. Bhadeshia: *Modell. Simul. Mater. Sci. Eng.*, 1995, vol. 3, pp. 265–88.
9. S.A. Davis, J.M. Vitek, and T.L. Hebble: *Weld. J.*, 1987, vol. 66 (10), pp. S289–300.
10. A. Kluken, Ø. Grong, and J. Hjelen: *Metall. Trans. A*, 1991, vol. 22A, pp. 657–63.
11. G. Kurdjumov and G. Sachs: *Zeitschrift für Physik*, 1930, vol. 64, pp. 325–43.
12. H.K.D.H. Bhadeshia: *Bainite in Steels*, 2nd ed., Carlton House Terrace, IOM Communications Limited, London, U.K., 2001.
13. S.S. Babu and H.K.D.H. Bhadeshia: *Mater. Sci. Eng: A*, 1992, vol. 156 (1), pp. 1–9.
14. J.M. Gregg and H.K.D.H. Bhadeshia: *Acta Metall. Mater.*, 1994, vol. 42 (10), pp. 3321–30.
15. N. Stenbacka and K.A. Persson: *Weld. J.*, 1989, vol. 68 (11), pp. 41–47.
16. U.F. Kocks, C.N. Tomé, and H.-R. Wenk: *Texture and Anisotropy: Preferred Orientations in Polycrystals and Their Effect on Materials Properties*, Cambridge University Press, Cambridge, U.K., 2000.
17. O. Engler and V. Randle: *Introduction to Texture Analysis: Macrotexture, Microtexture, and Orientation Mapping*, CRC Press, Boca Raton, FL, 2000.

18. A. Haldar, D. Bhattacharjee, and S. Suwas: *Microstructure and Texture in Steels: and Other Materials*, Springer, London, U.K., 2009.
19. H.J. Bunge: *Texture Analysis in Materials Science: Mathematical Methods*, Butterworths, London, U.K, 1993.
20. X.H. Ha, S.W. Jang, W.H. Bang, U.S. Yoon, and K.H. Oh: *Mater. Sci. Forum,*, 2002, vols. 408–412, pp. 1377–82.
21. H. Yu: *University of Science and Technology Beijing*, 2008, vol. 15 (6), pp. 184–88.
22. Y. Zhong, F. Xiao, J. Zhang, Y. Shan, W. Wang, and K. Yang: *Acta Mater.*, 2006, vol. 54 (2), pp. 435–43.
23. R.A. Farrar and P.L. Harrison: *J. Mater. Sci.*, 1987, vol. 22 (11), pp. 3812–20.
24. S. Shanmugam, N.K. Ramisetti, R.D.K. Misra, J. Hartmann, and S.G. Jansto: *Mater. Sci. Eng. A*, 2008, vol. 478 (1–2), pp. 26–37.
25. V. Venegas, F. Caleyo, T. Baudin, J.H. Espina-Hernández, and J.M. Hallen: *Corros. Sci.*, 2011, vol. 53 (12), pp. 3873–4326.
26. V. Venegas, F. Caleyo, J.M. Hallen, T. Baudin, and R. Penelle: *Metall. Mater. Trans. A*, 2007, vol. 38A, pp. 1022–31.
27. B. Hutchinson, N. Hansen, P.V. Houtte, and D.J. Jensen: *Philos. Transact. A Math. Phys. Eng. Sci.*, 1999, vol. 357 (1756), pp. 1471–85.
28. I.M. Richardson, N.J. Woodward, and J. Billingham: *The Twelfth Int. Offshore and Polar Engineering Conf.*, Kitakyushu, Japan, 2002.
29. G.R. Jones: *High Pressure Arcs in Industrial Devices*, Cambridge University Press, New York, NY, 1988.
30. A.S. Azar, N. Woodward, H. Fostervoll, and O.M. Akselsen: *J. Mater. Process Tech.*, 2012, vol. 1, pp. 211–19.
31. Ø. Grong: *Metallurgical Modelling of Welding*, 2nd ed., Maney Publishing, Cambridge, MA, 1997.
32. M. Suban and J. Tušek: *J. Mater. Process. Techn.*, 2001, vol. 119 (1–3), pp. 185–92.
33. Y. Wang and H. Tsai: *Metall. Mater. Trans. B*, 2001, vol. 32B, pp. 501–15.
34. M. Ferrante and R.A. Farrar: *J. Mater. Sci.*, 1982, vol. 17 (11), pp. 3293–98.
35. A. Kumar and T. DebRoy: *7th Int. Conf. on Trends in Welding Research*, S.A. Davis, T. DebRoy, J.C. Lippold, H.B. Smartt, and J.M. Vitek, eds., Pine Mountain, GA, 2005.
36. W. Zhang, C.-H. Kim, and T. DebRoy: *J. Appl. Phys.*, 2004, vol. 95, p. 5210.
37. K. Davut and S. Zaefferer: *Metall. Mater. Trans. A*, 2010, vol. 41A, pp. 2187–96.
38. S. Biggin and D.J. Dingley: *J. Appl. Crystall.*, 1977, vol. 10 (5), pp. 376–85.
39. O. Engler and V. Randle: *Introduction to Texture Analysis*, 2nd ed., CRC Press, Boca Raton, FL, 2000.
40. D.G. Brandon: *Acta Metall.*, 1966, vol. 14 (11), p. 1479.
41. D. Wolf and S. Yip: *Materials Interfaces: Atomic-Level Structure and Properties*, Chapman & Hall, London, U.K, 1992.
42. Y.L. He, S. Godet, J. Jacques, and J.J. Jones: *Mater. Sci. Forum*, 2005, vols. 495–497, pp. 1201–06.
43. J. Wheeler, D.J. Prior, Z. Jiang, R. Spiess, and P.W. Trimby: *Contrib. Mineral. Petrol.*, 2001, vol. 141 (1), pp. 109–24.
44. E. Keehan, L. Karlsson, H.K.D.H. Bhadeshia, and M. Thuvander: *Mater. Sci. Technol.*, 2008, vol. 24 (10), pp. 1183–88.
45. P.W. Bridgman: *Studies in Large Plastic Flow and Fracture: with Special Emphasis on the Effects of Hydrostatic Pressure*, Harvard University Press, Cambridge, MA, 1964.
46. W.D. Callister and D.G. Rethwisch: *Fundamentals of Materials Science and Engineering: An Integrated Approach*, Wiley, Hoboken, NJ, 2011.
47. W.B. Hutchinson: *Acta Metall.*, 1989, vol. 37 (4), pp. 1047–56.

Paper VI

Effect of Hyperbaric Gas Composition on Mechanical Properties of the Weld Metal

Amin S. Azar, Hans I. Lange, Erling Østby, and Odd M. Akselsen

Materials Science and Engineering A, 556 (2012) 465-472.

Is not included due to copyright